Toward a Deeper Understanding of Concentrated Electrolyte Effects in Redox Flow Batteries

Rohit Rungta

The Queen's College

University of Oxford

A thesis submitted for the degree of

Doctor of Philosophy

October 2025

Supervised by Prof. Charles W. Monroe

Last but not least, I wanna thank me
I wanna thank me for believing in me
I wanna thank me for doing all this hard work
I wanna thank me for having no days off
I wanna thank me for, for never quitting

I wanna thank me for always being a giver
And tryna give more than I receive
I wanna thank me for tryna do more right than wrong
I wanna thank me for just being me at all times

– Snoop Dog

Acknowledgements

My deepest gratitude goes to my supervisor, Prof. Charles Monroe, whose guidance and support have profoundly shaped my PhD journey. His mentorship, along with his generous sharing of resources and time, has been instrumental in developing my confidence and independence as a researcher. Charles' perfect balance of insightful direction and intellectual freedom, allowed me to confidently explore novel ideas and ultimately grow into a more thoughtful and capable researcher.

I also wish to thank my colleagues and friends in the Monroe Research Group – Kirk Smith, Andrew Wang, Zeyang Geng, Samson Foo, Taeho Jung, Krupal Patel, Alexander Van-Brunt, and Emmanuelle Hagopian. Our insightful discussions, camaraderie, and shared experiences have made my time in the lab both intellectually rewarding and thoroughly enjoyable. Special thanks are due to Dr. Kirk Smith, whose foundational work on flow batteries and crucial mentorship significantly accelerated my early research efforts. Kirk's willingness to share lessons from his previous experiences was invaluable.

I would not be where I am today without support from my community back home. I am immensely thankful for my high school teachers in Phoenix for inspiring me to pursue a career in the STEM field. Special thanks to Prof. Narayanan Neithalath who generously provided my first research opportunity. My professors at the University of California, Berkeley were pivotal in my decision to pursue graduate studies. I owe particular thanks to Prof. Jeffrey Reimer for providing my first opportunity towards independent research, and to Prof. Alexander Forse, whose patient and insightful mentorship profoundly shaped my early passion for research.

Heartfelt thanks to my cousins, Salony Roongta and Livio Spori, whose warm hospitality in Zurich provided a cherished refuge from the demands of my PhD studies and the dreary Oxford weather. Our shared escapades exploring the Swiss mountains and lakes will always hold a special place in my memories.

My sincerest gratitude goes to my partner, Melissa Young, whose unwavering support, kindness, and encouragement have been a constant source of strength throughout this journey. Her steady presence, though often unseen, has been indispensable.

Above all, I am eternally grateful to my parents. Their unconditional love and countless sacrifices have provided me with every opportunity imaginable. My mother, Archana Rungta, has my deepest respect for raising and shaping me into the person I am today. My father, Sanjay Rungta, impressed upon me the value of hard work, and his stoic love and unwavering pride through my highs and lows have never gone unnoticed. Both have instilled in me a profound respect for scholarly pursuits, and their faith in my abilities has always inspired me to reach higher. I stand on their shoulders and this achievement is as much theirs as it is mine.

List of Papers

This thesis is established on the following articles:

1. "*Mechanical properties of lithium electrolytes with dual carbonate cosolvents*" R. Rungta, P. Slowikowski, A. Gardner, D. Persa, C.W. Monroe, *Manuscript in preparation* (**2025**)

2. "*The emergence of Nernst–Planck laws from Onsager–Stefan–Maxwell theory*" R.Rungta, C.W. Monroe, *Manuscript in preparation* (**2025**)

3. "*Mitigating membrane fouling in non-aqueous redox flow batteries*" R. Rungta, C.W. Monroe, *Manuscript in preparation* (**2025**)

4. *"Drivers of membrane fouling in the vanadium acetylacetonate flow battery"* R. Rungta, K.P. Smith, C.W. Monroe, J. Membrane Science Letters, vol. 4, p. 100074, (**2024**)

5. *"Multi-Week Cycling of a Nonaqueous Flow Battery Using Tris-Bipyridine Iron (II) Triflate without Additional Supporting Electrolyte"* K.P. Smith, R. Rungta, A.A. Wang, C.W. Monroe, J. Electrochem. Soc., vol. 170, p. 060510, (**2023**)

Abstract

The rapid uptake of wind and solar power has created an urgent need for long-duration, grid-scale energy-storage technologies that are efficient, safe, and economically scalable. Redox flow batteries (RFBs) satisfy many of these requirements, yet their commercial adoption is hampered by poor durability, which in part owes to gaps in the fundamental understanding of ion transport in the concentrated electrolytes favored for high energy density. This dissertation delivers an integrated experimental–theoretical investigation that traces performance bottlenecks from the cell-scale symptoms of capacity fade to the micro-scale physics that govern ion motion in complex fluids.

Chapters 2 and 3 diagnose and mitigate the principal durability challenge in non-aqueous RFBs: membrane fouling. Using galvanostatic cycling, impedance spectroscopy, and a novel "canary-cell" protocol, I show that pore clogging – not electrolyte decomposition – dominates capacity decay in vanadium acetylacetonate systems. Flow-field redesign and active reservoir rebalancing suppress concentration gradients across the separator and extend cycle life by an order of magnitude.

Motivated by these findings, Chapter 4 revisits multicomponent transport theory. I recast the Onsager–Stefan–Maxwell (OSM) equations in a salt–charge coordinate system, clarifying how electroneutrality, thermodynamic non-ideality, and ion-ion friction govern ion transport and pinpointing the assumptions that collapse the OSM framework into the familiar Nernst–Planck form. The resulting hierarchy of sub-models, each invoking only the transport and thermodynamic parameters it needs, resolves coupled concentration and electrostatic-potential gradients in space and time, enabling practical prediction of ionic fluxes.

Chapter 5 closes the property loop by measuring the viscosity, density, sound speed, and compressibility of $LiPF_6$ in mixed-carbonate solvents over a broad concentration range. These constitutive relations, coupled with the new transport formalism, enable predictive simulation of concentrated-electrolyte behavior under extreme pressure and temperature variations. Although chemically distinct, both lithium-ion and non-aqueous RFB electrolytes combine rigid-ring solutes with flexible linear co-solvents, indicating that mixing volumes, partial-molar compressibilities, and related Gibbs free-energy derivatives follow generally transferable trends.

Collectively, the thesis integrates separator diagnostics, flow-field engineering, advanced transport modeling, and comprehensive property characterisation to build a unified picture of concentrated-electrolyte effects in RFBs. The resulting insights shorten the path from laboratory discovery to field deployment, guiding the design of more durable, efficient, and cost-competitive flow-battery systems essential for a decarbonised electricity grid.

Contents

List of Figures

List of Tables

Abbreviations

ACN . . . . . Acetonitrile

ASR . . . . . Area-specific resistance

BESS . . . . . Battery energy-storage system

CAISO . . . . . California Independent System Operator

CE . . . . . Coulombic efficiency

CNN . . . . . Convolutional neural network

CV . . . . . Cyclic voltammetry

EC . . . . . Ethylene carbonate

EE . . . . . Energy efficiency

EIS . . . . . Electrochemical impedance spectroscopy

EMC . . . . . Ethyl-methyl carbonate

ESS . . . . . Energy-storage system

NARFB . . . . . Non-aqueous redox-flow battery

OCV . . . . . Open-circuit voltage

OSM . . . . . Onsager–Stefan–Maxwell (framework)

PC . . . . . Propylene carbonate

PHS . . . . . Pumped-hydro storage

PID . . . . . Proportional–integral–derivative (control)

RFB . . . . . Redox-flow battery

RTE . . . . . Round-trip efficiency

SEM . . . . . Scanning-electron microscopy

SOC . . . . . State of charge

$TEABF_4$ . . . . . Tetraethylammonium tetrafluoroborate

UE . . . . . Utilisation efficiency

VE . . . . . Voltaic efficiency

VRFB . . . . . Vanadium redox-flow battery

Nomenclature

c_i	Molar concentration of species i ($\mathrm{mol} \cdot \mathrm{m}^{-3}$)
$c_{\mathbf{T}}$	Total molarity, $\sum_i c_i$ ($\mathrm{mol} \cdot \mathrm{m}^{-3}$)
D_i	Fickian diffusivity
$\mathscr{D}_{ij}$	Stefan–Maxwell diffusivity of i in j ($\mathrm{m}^2 \cdot \mathrm{s}^{-1}$)
ΔE	Cell potential (V)
F	Faraday's constant (96485 C mol^{-1})
$\mathbf{i}$	Current density ($\mathrm{A} \cdot \mathrm{m}^{-2}$)
J_i	Diffusive molar flux of species i
K_{ij}	Hessian of molar Gibbs free energy ($\mathrm{J} \cdot \mathrm{mol}^{-1}$)
L_{ij}	Onsager transport coefficient
M_{ij}	Onsager drag coefficient
N_i	Total molar flux of species i ($\mathrm{mol} \cdot \mathrm{m}^{-2} \cdot \mathrm{s}^{-1}$)
Q_t	Theoretical charge density ($\mathrm{Ah} \cdot \mathrm{L}^{-1}$)
Q_{ij}	Darken thermodynamic factor ($\mathrm{J} \cdot \mathrm{mol}^{-1}$)
R	Gas constant (8.314 J mol^{-1} K^{-1})
t	Time (s)
t_+	Cation transference number
T	Absolute temperature (K)
u_i	Ionic mobility $D_{ij}/(RT)$ ($\mathrm{m}^2 \cdot \mathrm{V}^{-1} \cdot \mathrm{s}^{-1}$)
$\mathbf{v}$	Mass-average velocity ($\mathrm{m} \cdot \mathrm{s}^{-1}$)

$\vec{v}^{\square}$	Volume-average velocity ($\mathrm{m} \cdot \mathrm{s}^{-1}$)
$\overline{V}_i$	Partial molar volume of species i ($\mathrm{m}^3 \cdot \mathrm{mol}^{-1}$)
x	Spatial coordinate (m)
y_i	Mole fraction of species i
z_i	Equivalent charge of species
η	Viscosity ($\mathrm{Pa} \cdot \mathrm{s}$)
κ	Ionic conductivity ($\mathrm{S} \cdot \mathrm{m}^{-1}$)
μ_i	Electro-chemical potential of i ($\mathrm{J} \cdot \mathrm{mol}^{-1}$)
ρ_e	Excess charge density ($\mathrm{C} \cdot \mathrm{m}^{-3}$)
Φ	Electric potential (V)
Φ_{NP}	Nernst–Planck over-potential (V)
Φ_z	Salt-charge potential (V)
χ	Thermodynamic factor

1 Introduction

Contents

1.1 Grid-scale energy storage

As global energy systems decarbonize, renewable electricity generation has grown rapidly due to increased investment and adoption [1]. Renewables accounted for 43.2% of global installed power capacity by the end of 2022, with solar, wind, and hydro comprising the largest shares [2]. These sources, however, are intermittent and non-dispatchable, leading to severe temporal mismatches between electricity supply and demand. The replacement of reliable fossil-fuel-based power plants with inconstant renewable energy sources is forcing the power system to undergo rapid changes [3]. The power grid was not built for extensive load balancing and

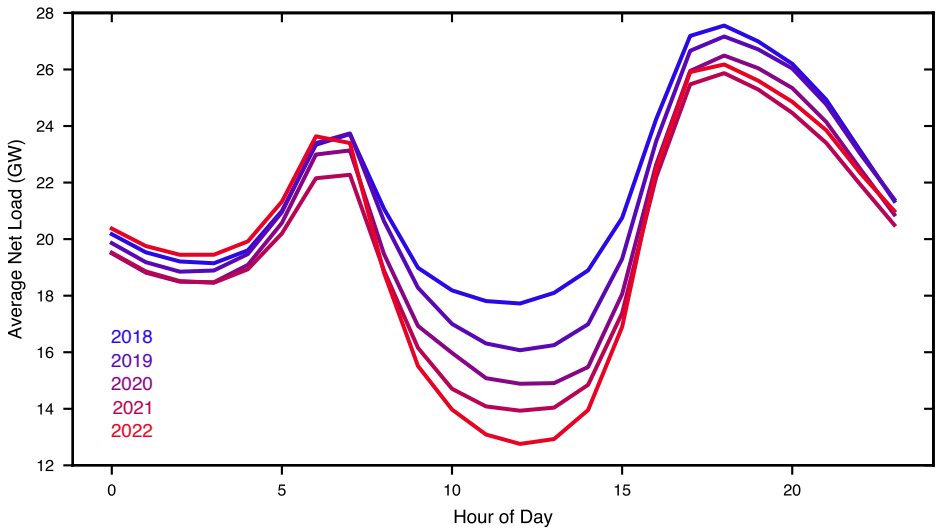

Figure 1.1: Average hourly net power loads in California for the month of January, using data from the California Independent System Operator [8]. Data from weekends and major U.S. holidays have been excluded to focus on typical weekday trends.

distribution, as it was designed around readily dispatchable fossil fuels.

The fluctuation in energy production from intermittent renewable energy sources, such as wind and sunlight, has motivated cities to redesign conventional grid operating paradigms [4, 5]. Studies have shown that the current power grid—with severe modifications—can only accommodate up to 20% of energy production from renewable energy sources without the need for energy storage systems [6, 7]. The California Independent System Operator (CAISO), for example, has faced increasing operational challenges due to solar overgeneration during midday hours, followed by steep ramping requirements in the evening when solar output drops and electricity demand surges. This pattern is illustrated by "duck curves," which depict the net load (total demand minus solar generation) throughout a typical day. Fig. 1.1 shows duck curves for the state of California in January, from 2018 to 2022. As solar installations have increased over the years, midday net demand has steadily declined. However, as the sun sets and people return home and begin consuming electricity, the grid experiences a sharp rise in load. These trends are expected to intensify as solar and other renewable energy sources continue to expand.

In the absence of sufficient storage, grid operators are often forced to curtail renewable generation during periods of overproduction. This not only wastes

	Pumped hydro	Vanadium RFB	Lithium-ion	Source
Projected Cost in 2025 $\left(\frac{€_{2018}}{\text{kWh}_{cap}}\right)$	205 ± 1	310 ± 78	302 ± 85	[10]
Typical Power Output (MW)	250 - 1000	0.1 - 10	0.1 - 5	[5, 11, 12]
Discharge Duration	several hours	2 - 8 hours	min - hours	[5]
Response time	sec - min	sec	sec	[5]
Roundtrip efficiency	75–85%	70–85%	85–95%	[5]

Table 1.1: Comparison of common grid-scale energy storage technologies

clean energy but also necessitates continued reliance on fossil-fuel-based peaker plants to maintain grid stability. Grid-scale energy storage systems (ESS) are necessary if the majority of energy in cities is to be sourced from renewable energy sources. By storing excess electricity during low-demand periods and discharging it during peaks, ESS enable load shifting, renewable firming, and reduced curtailment. Moreover, they can provide crucial ancillary services such as grid inertia and frequency regulation [9]. These advantages have sparked interest in developing efficient and cost-effective grid-scale energy storage technologies.

Table 1.1 provides a summary of the most widely deployed grid-scale energy storage systems. To date, pumped hydro storage (PHS) is the most mature form of grid-scale energy storage and has the largest market share of grid-connected storage; however, lithium-ion batteries have seen the fastest adoption over the past five years [10]. PHS systems offer long durations (up to 12 hours or more), high round-trip efficiencies (75–85%), and lifespans exceeding 50 years, making them exceptionally cost-effective over the long term. However, their deployment is limited by geographical requirements: access to water, significant elevation differences, and suitable land use. Where these conditions are met, pumped hydro is often considered the optimal energy storage solution due to its scalability, reliability, and economic performance.

1. Introduction

The cost of lithium-ion batteries has declined by over 85% in the past decade, catalyzing widespread deployment of battery energy storage systems. Nonetheless, lithium-ion technology remains cost-prohibitive for grid-scale, long-duration applications [13]. In response, the U.S. Department of Energy has set a target of a 90% cost reduction by 2030 for energy storage systems capable of delivering durations exceeding 10 hours [14]. Achieving this benchmark will likely necessitate the development of alternative electrochemical storage technologies, since lithium-ion systems are approaching their theoretical performance and cost limits due to decades of maturation and incremental optimization.

Beyond lithium-ion, several other battery technologies are being developed and deployed at grid scale. Redox flow batteries (RFBs) offer the advantage that they decouple power capacity from energy capacity, making them well-suited for long-duration storage. RFBs typically have lower energy densities than lithium-ion batteries but offer superior cycle life and safety. In many cases, flow batteries can now compete economically with natural-gas peaker plants, especially when accounting for emissions and policy incentives [15]. Vanadium redox flow batteries (VRFBs), in particular, stand out as a mature technology, exhibiting proven commercial viability globally. Long-term operational data from decades-old deployments demonstrate remarkable capacity and efficiency retention [16]. Leading companies like Invinity Energy Systems, Sumitomo Electric, and Rongke Power have spearheaded large-scale VRFB installations. Notably, the Chinese Dalian Rongke Power project boasts the largest VRFB installation with 200 MW / 800 MWh capacity. Similarly, Invinity Energy Systems' 2 MW / 5 MWh grid-connected system in Oxford, UK [17], underscores the versatility of the VRFBs for diverse grid applications. In parallel, the development of new organic electrolytes aims to significantly reduce electrolyte costs, enhancing the economic feasibility of large-scale deployment. Examples of these emerging chemistries will be discussed in later sections. Together, the commercial maturity of VRFB technology and the potential for substantial cost reductions through electrolyte innovation position flow batteries as a leading candidate to meet future energy storage needs.

Despite their promise, energy storage technologies face challenges, including high capital costs, environmental concerns related to battery production and disposal, and limited duration in many cases. Research into long-duration storage technologies such as iron-air batteries, flow batteries, and hydrogen-based systems is ongoing and essential to fully integrate renewable energy at scale. The accelerating deployment of renewables is straining legacy grid infrastructure and introducing operational instabilities that traditional grid planning was never designed to handle. Grid-scale energy storage offers a versatile and increasingly economical solution to these problems, and its rapid deployment is essential to ensure a stable, reliable, and decarbonized electricity system.

1.2 Flow battery fundamentals

In light of the urgent need for scalable and cost-effective grid storage solutions, redox flow batteries (RFBs) have garnered significant research attention. The following section examines the fundamental principles governing RFB operation, traces their historical development, defines key electrochemical performance metrics, and identifies current limitations and pathways for technological improvement.

1.2.1 Development of the traditional redox flow battery

The first recorded development of the modern redox flow battery was in a patent filed by Kangro in 1949 [18]. Kangro designed a system in which an active species was dissolved in a fluid and stored in two separate tanks as electrolytes. These electrolytes are then pumped through respective half cells to be oxidized or reduced. This system is fully reversible, as the electrolyte is once again pumped through the cell upon complete discharge. Notably, Kangro's design consisted of a singular active species that was stable in multiple oxidation states [Cr^{+3}/Cr^{+2}, Cr^{+6}/Cr^{+3}]. Electrolyte systems that use one metal species on both sides of the RFB reactor are referred to as single-metal chemistries. These have an inherent advantage over dual-metal electrolyte systems because crossover of the active species between the tanks does not result in permanent degradation of the system.

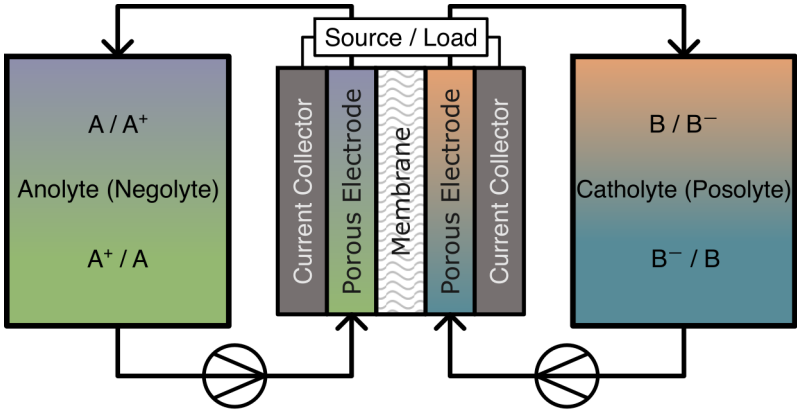

Figure 1.2: A traditional redox flow cell configuration

Due to the high cost of chromium during development, the extremely carcinogenic nature of the chromate and dichromate ions, and the low energy density of the system, the chromium-based RFB was not further pursued. Rather, researchers at NASA developed a working dual-metal redox flow battery with chromium and iron based active species in 1974 [19]. This replaced the oxochromium species with relatively cheap and abundant iron (Cr^{+2}/Cr^{+3} and Fe^{+2}/Fe^{+3}). The first working prototype of a dual-metal flow cell was based on NASA's iron–chromium chemistry, and that cell design is widely considered the traditional RFB configuration.

Fig. 1.2 shows a schematic of a traditional dual-metal RFB. One tank of electrolyte (anolyte) is pumped through the anode while the other is pumped through the cathode (catholyte). The catholyte and anolyte each pass through a porous electrode where the respective heterogeneous electrochemical reactions take place. Ideally, the separator between the two porous electrodes only allows for crossover of the supporting electrolyte to complete the electrical circuit while maintaining charge neutrality. Crossover of the active species would result in either self-discharge or permanent electrolyte degradation. Lastly, the graphite plates act as current collectors to connect the current leads to the power source/load.

The modular design of RFBs is perhaps one of their greatest advantages over other battery systems. Since the active materials are stored in liquids outside the flow reactor, the energy content is determined only by the total volume of electrolyte. Similarly, the power capability is only a function of the reacting surface

area, which can be altered by connecting several flow cells in series. Most traditional batteries, based on intercalation (e.g., lithium nickel manganese cobalt oxides), plating (e.g., lithium metal), or conversion reactions (e.g., silicon anodes) within porous electrodes, do not permit this decoupling of power and energy. Fig. 1.3 shows a visual representation of two different RFB reactor configurations with different power and energy capabilities.

The modularity of RFB design greatly simplifies the manufacturing process. Scaling a RFB system's energy or power capability only requires the trivial construction of electrolyte tanks and relatively straightforward connection of electrical systems. Scaling up the capacity or power of a traditional battery, by contrast, requires modification of the entire cell-fabrication process. The percentage of inactive materials such as binders and packaging largely remain the same for both large and small RFB installations. Thus, RFBs are prime candidates for large-scale energy storage applications where energy density is not the primary consideration.

Following NASA's development of the Cr/Fe flow battery, a variety of electrolyte chemistries and hybrid flow configurations have been explored and implemented. While these various chemistries and hybrid configurations will be explored in future sections, the most notable and well-researched of them is the all-vanadium redox flow battery. This single-metal system was first developed by Skyllas-Kazacos et al. in 1986 [20]. The cell half-reactions at a very low pH in sulfuric acid are

$$\mathrm{VO_2}^+ + 2\mathrm{H}^+ + \mathrm{e}^- \leftrightharpoons \mathrm{VO}^{2+} + \mathrm{H_2O}, \quad E^\ominus = 1.00 \text{ V vs. SHE} \quad \text{(positive electrode)} \tag{1.1}$$

and

$$\mathrm{V}^{3+} + \mathrm{e}^- \leftrightharpoons \mathrm{V}^{2+}, \quad E^\ominus = -0.291 \text{ V vs. SHE} \quad \text{(negative electrode)} \tag{1.2}$$

leading to an overall cell reaction (with the discharge reaction producing products, and recharge returning to reactants) of:

$$\mathrm{VO_2}^+ + \mathrm{V}^{2+} + 2\mathrm{H}^+ \leftrightharpoons \mathrm{VO}^{2+} + \mathrm{V}^{3+} + \mathrm{H_2O} \tag{1.3}$$

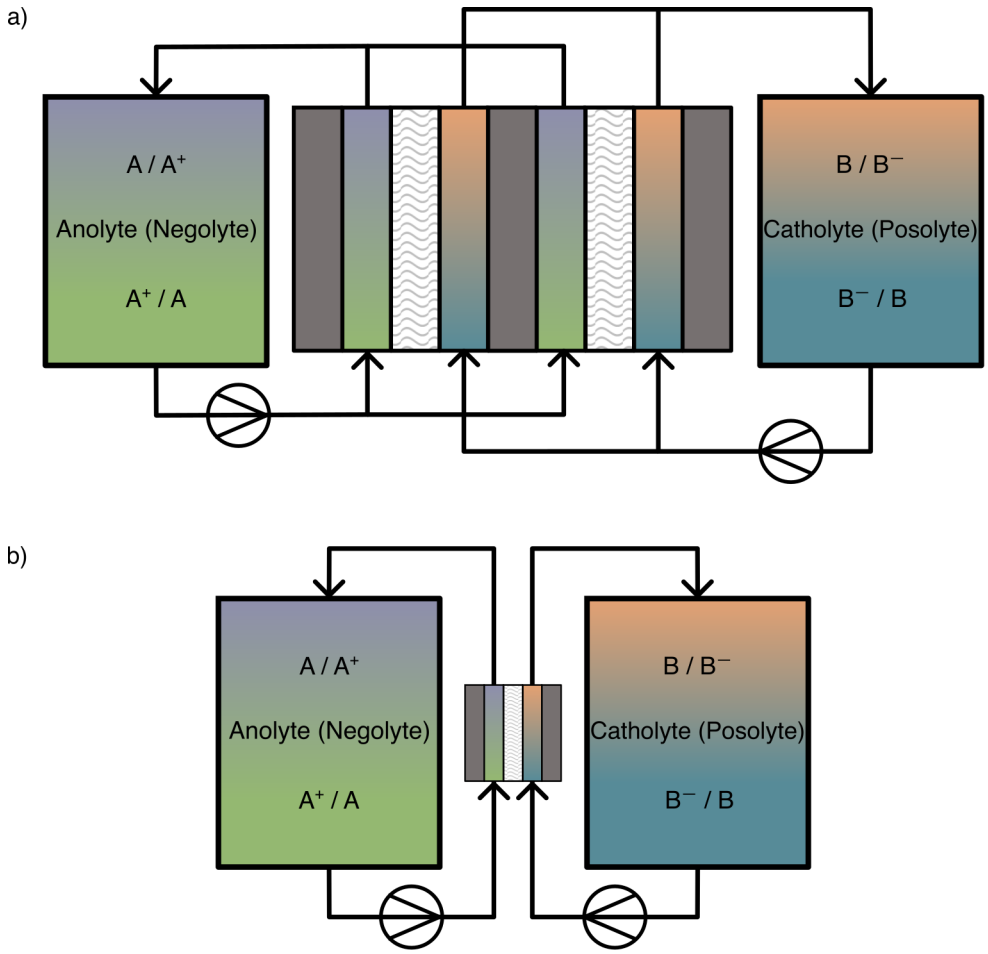

Figure 1.3: A traditional redox flow cell configuration with an a) increased active surface area for higher power capability and b) increased volume of electrolyte for higher energy capacity.

The half-reactions have been proven to be highly reversible and stable with fast kinetics. This, in combination with decades of research and enhancements in materials and cell design all contribute to a relatively high overall energy efficiency of 88% while accounting for pumping losses [21–23]. Very few practical electrolyte systems have been able to match the energy efficiency and long-term stability of the aqueous VRFB.

While companies have been installing VRFBs for more than a decade [24], many studies still show that this battery does not meet the cost requirements for broad market penetration [25, 26]. The largest cost associated with the battery is the electrolyte itself, which contributes to 60% of the total cost [27]. Vanadium remains quite expensive, and its cost is not projected to decrease significantly

with economies of scale due to its scarcity. Additionally, the Nafion membrane used throughout all VRFB contributes to 30% of the total cell cost. The cost of these two components is the primary factor preventing widespread adoption of this technology. In addition to economic considerations, several practical considerations make the implementation of this battery unfeasible. The corrosiveness and toxicity of the vanadium electrolyte (stored at very low pH) possess safety concerns while the narrow optimal operational range between 10 and 40°C would necessitate an active heat management system [28]. Researchers have been attempting to develop electrolyte systems that are less harmful to the environment while being significantly cheaper than the state-of-the-art VRFB – a task that has been proven quite difficult.

1.2.2 Development of hybrid electrolyte systems

Several RFB literature reviews have classified and summarized the various electrolyte chemistries [29–33]. In general, all flow batteries can be classified as either a one-phase all-liquid electrolyte system or a hybrid system that utilizes two different phases (suspension, solids, or gasses). Fig. 1.4 shows a visual breakdown of common electrolytes and their place in the RFB community. Simple inorganic ions in all-liquid RFBs were the starting point for electrolyte development since they have relatively simple chemistries with high solubilities in aqueous solvents. As research progressed, the all-vanadium flow battery had the best performance among other inorganic liquid phase electrolyte systems but was deemed economically unfeasible for widespread adoption [34]. The three primary methods of decreasing the cost of similar RFBs are to: 1) increase the standard cell potential per mole of active species, 2) increase the solubility of active species to allow for higher current densities, and 3) avoid expensive metals such as vanadium altogether by using all-organic electrolyte systems.

To allow for larger cell potentials, several studies explored the use of nonaqueous solvents such as acetonitrile (ACN) and propylene carbonate (PC) [35–37]. These solvents are stable over a larger potential difference than water, as they are not limited by H_2 and O_2 evolution. While aqueous batteries can operate stably at or

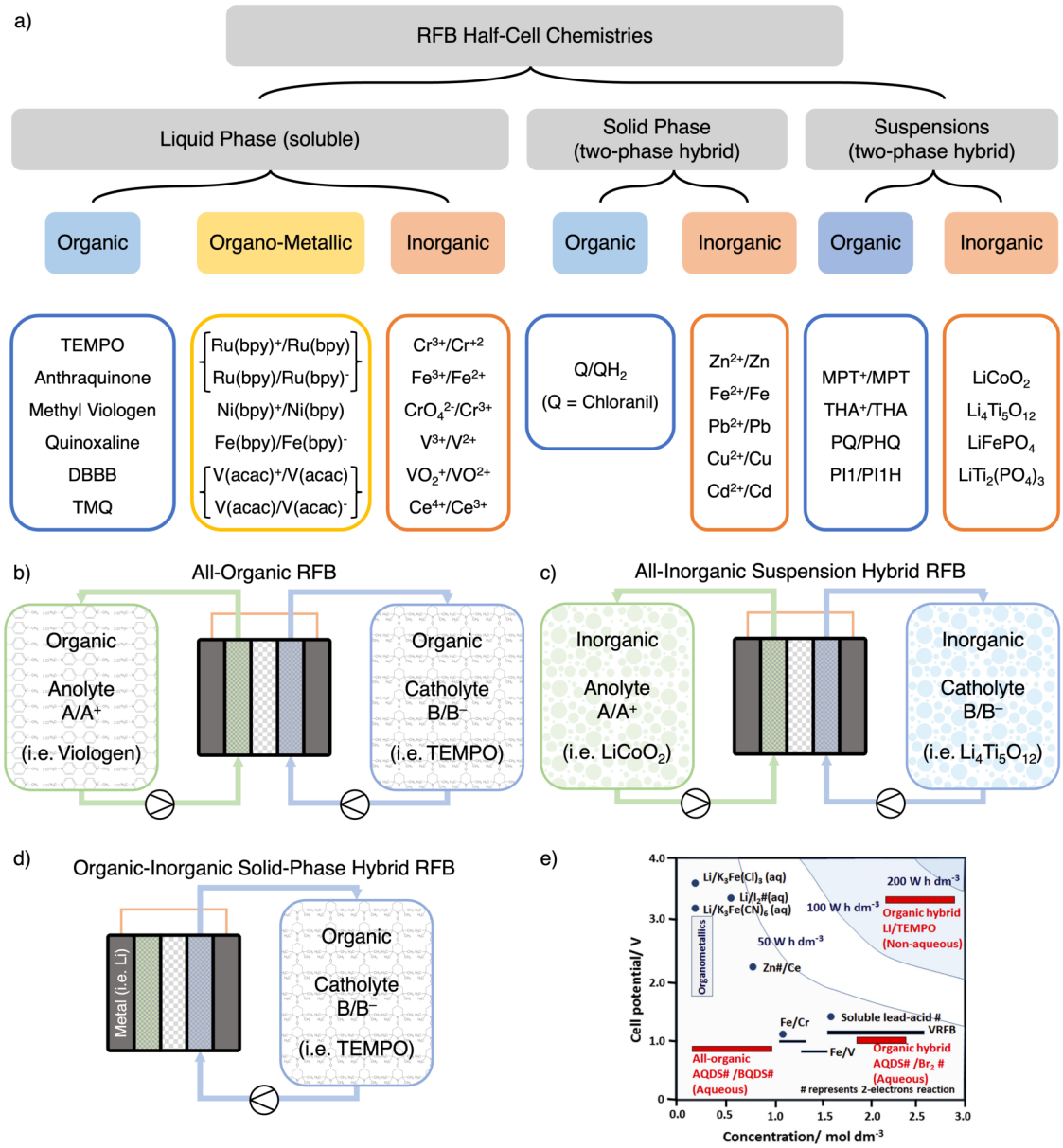

Figure 1.4: Overview of electrolyte systems and RFB configurations: a) classification of various half-cell electrode reactions used in RFBs; b-d) visual representations of RFB configurations when different half-cell reactions are combined in a RFB; and e) comparison of common performance metrics of existing organic flow battery systems. Adapted from Leung et al. [33]

even slightly beyond this thermodynamic window through favorable thermodynamics and kinetic suppression of gas evolution (e.g., lead–acid systems), the accessible potential range remains more constrained than in nonaqueous media. Simple ions such as V^{+2} or V^{+3}, however, have very low solubilities in nonaqueous solvents [38]. This gave rise to organometallic complexes which consist of a transition metal

center and peripheral ligands. Many aromatic ligands such as acetylacetone (acac) and 2,2'-bipyridine (bpy) are used since they stabilize radicals and can be tuned to increase the redox potential [39, 40]. Furthermore, the addition of large ligands greatly increases the solubility of the active species in nonaqueous solvents. Thus, organometallics can maintain roughly the same active species solubilities while exhibiting larger standard cell potentials.

While organometallic complexes would theoretically decrease the costs of RFBs, they are still limited by the scarcity of expensive metal elements. Fully organic electrolytes pose an environmentally safe and cheap alternative. Many of the proposed compounds, such as anthraquinone and viologen, are naturally abundant and obtained from a variety of sources [41]. Perhaps the largest drawback to organic liquid electrolytes is that they often require low cell potentials to ensure long cell lifetimes. Organic active materials are usually less stable than their organometallic counterparts, so operation at high voltages results in side reactions and permanent electrolyte degradation [42, 43]. Solubilities of organic active materials depend greatly on the solvent but can be tuned – similar to organometallic compounds. Currently, no stable organic anolytes have been found with a redox potential smaller than that of anthraquinone-2-sulfonic acid (-0.60 V vs. mercurous sulfate electrode) [44]. The lack of a suitable anodic material has been preventing the adoption of all-organic redox flow batteries.

Solid-phase hybrid RFBs have also been tried to lower system cost. Use of a solid anode or cathode greatly increases energy density. An example of the Li metal and organic TEMPO electrolyte RFB configuration is shown in Fig. 1.4d). RFB systems that use lithium metal as an anode (3.04 V vs. SHE) along with organic electrolytes have the largest energy densities of all RFBs to date as they often have high cell voltages of 3.40 V [45]. The main drawbacks of these hybrid RFB configurations are that almost all metal electrodes (especially zinc) suffer from deleterious dendrite growth, resulting in poor cycling performance [46]. Moreover, this hybrid configuration still uses corrosive electrolytes and loses the modular flexibility present in all-liquid RFBs.

Suspension hybrid RFBs provide similar energy densities to solid-phase hybrid RFBs while maintaining the modularity of all-liquid RFBs. Duduta et al. proposed a class of hybrid RFBs that circulate active materials through the cell in slurries with conductive additives [47]. This liquid form avoids dendrite growth while still having a significantly high molar concentration of active species. A major concern regarding suspension RFBs is the high viscosity of the electrolyte, which in turn increases pumping losses and provides additional operational complexities. The primary active materials that are used in these RFB configurations are $LiCoO_2$ and $Li_4Ti_5O_{12}$ – both of which are expensive to manufacture and require extensive mining practices [48]. While this nascent technology shows promise in achieving high densities and long cycle lives, its application for grid-scale storage is minimal to none. The energy density comes at a price of expensive and toxic active materials; however, grid-scale energy storage technologies prioritize affordability, cycle life, and environmental impact over energy density.

Adapted from Leung et al., Fig. 1.4e) shows a plot comparing the energy density and cell potential for various RFB chemistries/configurations [33]. As expected, all stable configurations with a cell potential >2.0 V have a nonaqueous solvent system. All-organic batteries currently have low energy densities, cell potentials, and solubilities, mainly due to the lack of a suitable anodic active material. Aqueous organic–inorganic half-cells can achieve higher active-species concentrations, but their low cell potentials—limited by water stability—result in poor energy densities. Organometallics achieve higher cell potentials in nonaqueous systems while current research is working to increase their solubility limits. Lastly, nonaqueous organic hybrid RFBs exhibit the best performance, but at the cost of practicality in grid-scale RFB applications.

1.2.3 Performance metrics

Although various RFB chemistries have been investigated for durability and cost-efficiency, inconsistent testing protocols and evaluation criteria hinder meaningful comparisons across studies. Table 1.2 summarizes the most important parameters

for characterizing cell/electrolyte attributes, cycling conditions, and performance metrics. These metrics are essential for comparing the performance and rough costs across all RFB chemistries and configurations. For example, many experimental studies of suspension RFBs fail to measure and report the viscosity of the electrolyte. The solid suspensions would result in relatively high realized energy densities, but these values are misleading – a significant amount of energy would be needed to pump the electrolytes and pumping losses cannot accurately be estimated without viscosity measurements.

The key attributes that define an electrolyte system are the overall cell potential and energy density. The energy density is a function of the cell potential (which is also dependent on the electrode material), the number of transferred electrons per mole of active species, and the solubility of active species. It is important to note that electrolyte systems with the largest energy densities are not necessarily the best candidates for RFBs. For example, a modular liquid all-organic electrolyte (with cheap starting materials) would yield a low energy density but is preferred over the energy-dense hybrid configurations (with expensive operating and starting materials).

Once an electrolyte system is fully defined, one must clearly state the cell cycling conditions and parameters. Current density and flow rate have been shown to have a significant impact on cell performance due to mass transport limitations [49, 50]. In most experiments, less than 70% of the theoretical solubility of active species is used to prevent precipitation and pump failure. Thus, a charge density for the cycling conditions should be reported in addition to the theoretical charge density as these are more representative of operating conditions. Additionally, reporting the state of charge (SOC) window depicts the depth of charge and discharge to allow for better analysis of cell performance. Lastly, the flow rate and electrolyte viscosities gives the reader a measure of the pumping losses that would be realized in practical operations.

The most reported performance metrics are coulombic efficiency (CE) and energy efficiency (EE). The coulombic efficiency is the ratio of discharge capacity to charge capacity and is a useful metric for assessing the charge reversibility of each cycle. A

	Formula	Units	Comments
Cell Attributes			
Cell Potential	$\Delta E = E_a - E_c$	V	E_a = anodic formal potential E_c = cathodic formal potential
Theoretical Charge Density	$Q_t = \frac{S \cdot n \cdot F}{3600}$	$\frac{\text{Ah}}{\text{L}}$	S = solubility limit of active species n = number of electrons per mole active species F = Faraday constant
Theoretical Energy Density	$E_t = Q_t \cdot \Delta E$	$\frac{\text{Wh}}{\text{L}}$	Q_t = theoretical charge density ΔE = cell potential
Flow Field			Flow-through, interdigitated, serpentine, etc.
Cycling Conditions			
Charge Density	$Q = \frac{C_a \cdot n \cdot F}{3600}$	$\frac{\text{Ah}}{\text{L}}$	C_a = concentration of active species
Current Density		$\frac{\text{mA}}{\text{cm}^2}$	
SOC Window		%	
Flow Rate		$\frac{\text{mL}}{\text{min}}$	
Kinematic Viscosity		$\frac{\text{m}^2}{\text{s}}$	
Performance Metrics			
Coulombic Efficiency	$\frac{\text{CE}}{100} = \frac{Q_{\text{discharge}}}{Q_{\text{charge}}}$	%	$Q_{\text{discharge}}$ = charge output Q_{charge} = charge input
Energy Efficiency	$\frac{\text{EE}}{100} = \frac{\int I_{out} V_{Cell}\, dt}{\int I_{in} V_{Cell}\, dt}$	%	I_{out} = current output I_{in} = current input V_{Cell} = cell potential
Utilization Efficiency	$\frac{\text{UE}}{100} = \frac{Q_d}{C_a \cdot n \cdot F \cdot V_{Cell}}$	%	
Voltaic Efficiency	$\frac{\text{VE}}{100} = \frac{\text{EE}}{\text{CE}}$	%	
Capacity Decay		$\frac{\%}{\text{cycle}}$	

Table 1.2: Common performance metrics for flow batteries

decrease in coulombic efficiency is most often attributed to self-discharge (crossover) or electrolyte degradation (side reactions). Energy efficiency is the ratio of discharge energy to charge energy at a certain current density. This accounts for both the CE and the voltaic efficiency (VE). The voltaic efficiency is the ratio of average

discharge voltage to average charge voltage. The VE is often used to monitor the overpotentials during cell operation. Other useful metrics are utilization efficiency and capacity decay rate. Utilization efficiency is the ratio of discharge capacity to theoretical discharge capacity (for the given charge density of the system). This metric enables easy comparison of the realized depth of charge/discharge to the expected SOC determined when identifying cycling conditions. The capacity decay rate is often reported in units of '% per cycle' or '% per day'. These units are slightly problematic since they are highly dependent on the charging SOC and volume of total electrolyte respectively. Reporting capacity decay rates in units of '% per full discharge' would enable easy comparison between different charging SOCs and current densities. This does, however, assume a constant rate of decay across all SOCs, which is not always accurate.

1.3 Approaches to modeling ionic transport

This section summarizes the two overarching models used to describe ionic transport in electrolytic solutions for battery applications in general: 1) dilute solution theory, and 2) concentrated solution theory. The earliest transport models describing dilute solutions are introduced and their evolution into concentrated solution theory to describe species-species interactions are outlined.

1.3.1 Dilute solution theory

Core to the modeling of transport in aqueous media is the idea of diffusion. Diffusion refers to the spontaneous migration of discrete entities – atoms, ions, or molecules – from regions of elevated concentration toward zones of depletion, thereby driving the system toward spatially uniform composition. Fick conducted the earliest quantitative treatment [51] of this phenomenon and asserted that the molar flux of species i, J_i, is proportional to the gradient of its molar concentration, ∇c_i through

$$J_i = -D_i \nabla c_i, \tag{1.4}$$

where D_i is the Fickian diffusivity of species i in its solvent. The proportionality constant D_i characterises the intrinsic mobility of the diffusing species within its medium. The Fickian fluxes have been shown to accurately describe diffusion in dilute and stagnant solutions, especially those without charged species [52–55].

The Nernst–Planck framework extends Fick's concept of diffusion to incorporate the transport of ions under an electric field $\left(-\vec{\nabla}\Phi\right)$ and convection through a bulk flow velocity $\vec{v}$. The total species fluxes $\vec{N}_i$ as a vector quantity was expressed mathematically as

$$\vec{N}_i \;=\; -D_i\Big(\frac{F z_i c_i}{RT}\,\vec{\nabla}\Phi \;+\; \vec{\nabla}c_i\Big) \;+\; c_i\,\vec{v}, \tag{1.5}$$

where F is Faraday's constant, R the gas constant, T the absolute temperature, and z_i the equivalent charge of species i [56, 57]. This expression encapsulates three distinct transport processes governing the flux of a charged species i: electromigration arising from gradients in electric potential, diffusion, modeled in accordance with Fick's law, and convective transport, driven by bulk fluid motion. The primary strength of this framework lies in its elegance and tractability – species flux can be characterized with a single diffusivity parameter. Note that some Nernst–Planck models incorporate a separate mobility parameter u_i associated with migration, but diffusivities are more often linked to ionic mobility via the Nernst-Einstein relation ($u_i = D_i/RT$), which has been incorporated into equation 1.5 [58].

Despite its wide adoption, the Nernst–Planck model is limited by its assumptions. Specifically, the model assumes that individual species dissolved within an electrolytic solution do not not interact with each other, but only with the solvent. As a result, the Fickian diffusivity parameter for species i only depends on the species and the solvent. For example, in the case of a binary salt, diffusivities of the cation (D_+) and anion (D_-) fully specify transport within this framework. For an electrolyte with unit cation and anion charge ($z_+ = -z_- = 1$), the Nernst–Planck diffusivities have been shown to map to three easily measured macroscopic properties—ionic conductivity κ, Fickian salt diffusivity D, and the

cation transference number t_+—through

$$\kappa = \frac{F^2 c}{RT}\Big(D_+ + D_-\Big), \qquad D = \frac{2\,D_+\,D_-}{D_+ + D_-}, \qquad t_+ = \frac{D_+}{D_+ + D_-}. \tag{1.6}$$

Note that the macroscopic parameters are overspecified – only two independent transport parameters determine three macroscopic electrolyte properties. Studies have shown that this situation is problematic even at relatively high dilution [59] but becomes especially concerning at high concentrations (0.1 M in Li-ion electrolytes) [60, 61].

1.3.2 Concentrated solution theory

The Onsager–Stefan–Maxwell (OSM) framework addresses the pitfalls in dilute solution theory by considering species–species interactions. This was done by adding distinct Stefan–Maxwell diffusivities $\mathscr{D}_{ij}$ between each pair of species [62]. In the case of a binary salt dissolved in a solvent, for example, this would yield three transport parameters: $\mathscr{D}_{+-}$, $\mathscr{D}_{+0}$, and $\mathscr{D}_{-0}$, where '+' represents the cation, '−' the anion, and '0' the solvent. Generally, the OSM equations can be used to express the gradients in electrochemical potentials $\vec{\nabla}\mu_i$ in terms of the force per unit volume exerted by species j on species i as a result of their relative motion as

$$-\,c_i\,\vec{\nabla}\mu_i \;=\; \sum_{j\neq i} \frac{R\,T\,c_i\,c_j}{c_\mathrm{T}\,\mathscr{D}_{ij}}\Big(\vec{v}_i - \vec{v}_j\Big), \tag{1.7}$$

where c_T is the total molarity of the solution and $\vec{v}_i = \vec{N}_i/c_i$ is the number-average velocity of species i. Note that upon specification of a consistent reference velocity for convection, Eq. 1.7 can be inverted into its flux-explicit form:

$$\vec{j}_i = \sum_{j\neq i} L_{ij}\vec{\nabla}\mu_i \tag{1.8}$$

where L_{ij} are called Onsager diffusivities, and $\vec{j}_i$ is the excess molar flux of species i relative to the mass-average velocity. Previous works have outlined transformation processes that convert Stefan-Maxwell diffusivities to Onsager diffusivities with respect to various reference velocities [63, 64]. Despite their differing formulations,

both the force-based and flux-based frameworks yield electrolyte transport models that are thermodynamically consistent.

Similar to dilute solution theory, the independent transport parameters of a binary electrolyte can be related to macroscopically observable transport properties through

$$\begin{aligned} \frac{1}{\kappa} &= \frac{RT}{c_{\mathrm{T}} F^2}\left(\frac{1}{\mathscr{D}_{+-}} + \frac{c_0}{c_+}\frac{1}{\mathscr{D}_{0+}+\mathscr{D}_{0-}}\right), \\ D = \chi\frac{2\,\mathscr{D}_{0+}\mathscr{D}_{0-}}{\mathscr{D}_{0+}+\mathscr{D}_{0-}}, &\quad \text{and} \quad t_+^0 = \frac{\mathscr{D}_{0+}}{\mathscr{D}_{0+}+\mathscr{D}_{0-}}, \end{aligned} \tag{1.9}$$

where χ is a dimensionless parameter called the thermodynamic factor. Thermodynamic factors are necessary in the OSM framework to convert concentration gradients into electrochemical-potential gradients [65] and are defined as

$$RT\,\chi_{ij} = y_i\left(\frac{\partial \mu_i}{\partial y_j}\right)_{T,p,\,y_{k\neq j,n}}, \tag{1.10}$$

where $y_i = c_i/c_{\mathrm{T}}$ is the mole fraction of species i. Application of the Gibbs–Duhem relation ($\sum_{i=1}^{n} y_i d\mu_i = 0$) highlights the fact that one of the mole fractions and thermodynamic factors always depends on the rest. The set of independent thermodynamic factors can be used to relate electrochemical potential gradients to mole fraction gradients through

$$d\mu_i = \frac{RT}{y_i}\sum_{j=1}^{n-1}\chi_{ij}\,dy_j. \tag{1.11}$$

Note that this work will primarily utilize the Darken matrix, which is closely related to the traditional thermodynamic factor χ. The Darken matrix, defined as

$$Q_{ij} = y_i\left(\frac{\partial \mu_i}{\partial y_j}\right)_{T,p,\,y_{k\neq j,n}}, \tag{1.12}$$

differs from χ only in that it has units of molar energy.

1.4 Thesis structure

The argument of this dissertation unfolds in six chapters that trace a continuous arc from the systems-level motivation for grid-scale energy storage to the mechanistic,

theoretical, and design insights that advance redox-flow battery (RFB) technology. Chapter 1 establishes the practical and intellectual setting: it situates long-duration storage within the decarbonization of electricity networks, surveys the historical evolution of RFBs, and introduces concentrated-solution theory.

With the foundation laid, Chapter 2 turns to the chief durability challenge facing non-aqueous RFBs – membrane fouling. Galvanostatic cycling, impedance spectroscopy, and a "canary-cell" protocol converge on a single conclusion: pore clogging in commercial separators, rather than chemical decay of the electrolyte, governs capacity fade. The insights from Chapter 2 furnish the performance metrics and diagnostic tools that Chapter 3 then leverages to explore mitigation strategies. Two key factors of flow-field geometry and active electrolyte rebalancing are explored in detail, and the data reveal how minimizing concentration gradients across the porous separator can extend cell life by an order of magnitude.

The empirical results of Chapters 2 and 3 prompt a theoretical detour in Chapter 4, which revisits the Onsager–Stefan–Maxwell (OSM) framework. By reformulating multicomponent transport in a salt–charge coordinate system, the chapter dissects the respective contributions of electroneutrality, thermodynamic non-ideality, and ion–ion friction, showing that the widely-used Nernst–Planck equation is merely a dilute-solution limit of a more general transport description. The analytical criteria derived here explain the experimental trends observed earlier and demarcate the conditions under which engineers may safely adopt simplified models.

Chapter 5 extends the transport analysis into the thermo-mechanical domain. Systematic measurements of viscosity, density, and compressibility for $LiPF_6$ in mixed-carbonate solvents populate the constitutive relations introduced in Chapter 4. Trends from the Li-ion electrolytes and their relevance to RFB applications are discussed. By closing this materials-property loop, this chapter accelerates the development and implementation of predictive transport models.

Finally, Chapter 6 argues that a unified perspective on separator fouling, flow-field design, and concentrated-solution transport accelerates the path from

laboratory discovery to commercial deployment. The chapter concludes by outlining avenues for future research.

Taken together, the chapters progress from identifying concentration-related degradation phenomena to understanding and modeling their transport behavior. Each stage builds deliberately on its predecessors, so that by the end of the dissertation the reader will have an appreciation for how micro-scale physics governing ion transport in concentrated solutions can be reconciled in the design of durable RFB systems.

2

Drivers of Membrane Fouling in Redox Flow Batteries

Contents

2.1 Introduction

As discussed in section 1.2.2, the three primary approaches to decreasing the cost of redox flow batteries (RFBs) are: 1) increasing the standard cell potential per mole of active species, 2) enhancing the solubility of active species, and 3) avoiding the use of expensive metal ions. Addressing the first two objectives, Liu et al. first proposed the non-aqueous vanadium acetylacetonate electrolyte [66], leveraging a nonaqueous solvent to achieve higher stable cell voltages and employing the acetylacetonate ligand to improve solubility to levels comparable with aqueous systems. The $V(acac)_3$ RFB chemistry involves two elementary half-reactions:

$$V(acac)_3{}^+ + e^- \leftrightharpoons V(acac)_3, \quad E^\ominus = 1.72 \text{ V vs. } Ag^{0/+} \tag{2.1}$$

at the positive electrode, and

$$V(acac)_3 + e^- \leftrightharpoons V(acac)_3{}^-, \quad E^\ominus = -0.46 \text{ V vs. } Ag^{0/+} \tag{2.2}$$

at the negative electrode [67]. Since the $V(acac)_3$ coordination complex undergoes outer-sphere electron transfer reactions upon oxidation or reduction, the reaction kinetics at both electrodes is rapid [68], enabling discharge voltages near 2 V under practical current densities [69].

Charging the $V(acac)_3$ RFB involves a one-electron electrochemical disproportionation reaction:

$$2\,V(acac)_3 \leftrightharpoons V(acac)_3{}^+ + V(acac)_3{}^-, \quad \Delta E^\ominus = -2.18 \text{ V}, \tag{2.3}$$

resulting in identical electrolytes in both the positive and negative reservoirs at the fully discharged state. Such 'common-electrolyte' configurations offer a distinct advantage by making electrolyte mixing a reversible process. Consequently, active-species crossover through the separator membrane causes self-discharge rather than irreversible electrolyte compositional changes that require periodic regeneration. This inherent crossover tolerance permits the use of inexpensive porous separators for common-electrolyte RFBs, avoiding the costly ion-exchange membranes typically necessary for traditional RFB systems.

Historically, the long-term stability of the $V(acac)_3$ electrolyte has been hindered by various hypothesized degradation mechanisms, such as side reactions triggered by trace environmental contaminants interacting with electrodes and wetted components [70, 71]. By eliminating such contaminants, this chapter identifies membrane fouling as the primary mechanism responsible for capacity fade during cycling within RFB reactors. The methods and conclusions drawn here are widely applicable across various RFB chemistries, and similar degradation phenomena have been observed in aqueous and organic electrolyte systems [72], although they are more challenging to isolate.

This chapter quantifies performance metrics from cycling experiments performed on $V(acac)_3$ RFB reactors equipped with porous separators. These measurements elucidate the trade-off between reduced capital costs associated with cheaper membranes and increased operational losses due to crossover-related inefficiencies. Moreover, this analysis helps differentiate performance degradation sources, pinpointing how alterations in separator properties affect battery performance across cycling.

Further experiments were conducted using secondary flow reactors ('canary cells') arranged in series with the primary reactor. These cells provided insight into how operating conditions and varying electrolyte states contribute to separator degradation during prolonged cycling. Key performance indicators and trends are thoroughly examined, aiming to clearly distinguish the characteristic signs of membrane fouling from self-discharge and electrolyte degradation effects. Achieving an independent understanding of these phenomena is essential when assessing disproportionation-based RFB chemistries using flow reactors.

2.2 Experimental

Unless otherwise stated, all chemicals and materials were used as received. Cycling experiments and electrolyte handling were always conducted in an argon-filled (99.998%, BOC, UK) Inert Pure LabHE glovebox with atmospheric water and oxygen contents below 0.5 ppm.

2.2.1 Electrolyte preparation

Molecular sieves (4 Å, Fisher Scientific, UK) were dried at 250 °C for 24 h under vacuum and transferred to the glovebox while warm before use. HPLC-grade acetonitrile (Thermo Fisher, 99.9%, UK) was degassed with argon and purified with a PureSolv-Micro solvent purification system (Inert, UK). Purified acetonitrile (ACN) was transferred to the glovebox and further dried over the molecular sieves. After drying for 48 h, a C30 Karl Fischer Coulometric Titrator (Mettler-Toledo, UK) was used to confirm water content below 0.5 ppm. $V(acac)_3$ (98%, Strem, UK) was recrystallized with the anhydrous ACN and washed with anhydrous diethyl ether (Honeywell, 99.5%, UK) in the glovebox. The purified $V(acac)_3$ crystals were dried and stored in the glovebox. Tetraethylammonium tetrafluoroborate ($TEABF_4$, 99%, Sigma, UK) was stored in the glovebox and used as received.

2.2.2 Reactor design

The flow-through reactor designed by Smith [73], with a separator area of 2.20 cm^2 parallel to the flow direction and a compressed depth of 1.6 mm normal to the flow, was used for all cycling experiments; Appendix 2.A.1 outlines further details regarding reactor dimensions and design choices. Flow reactors were assembled and cycled in the glovebox. The electrodes were 3.18 mm thick carbon felt (Alfa-Aesar, UK), dried under vacuum at 250 °C for 48 h before reactor assembly. Separators—either Daramic 175 or Celgard 4560—were rinsed in anhydrous ACN before use. Expanded polytetrafluoroethylene (ePTFE, Gore, USA) gaskets were used between the resin-impregnated graphite plate (Graphite-Store, USA) and separator. The four screws clamping the reactor assembly together were tightened to a torque of 4.5 $N \cdot m$. After this compression the reactor had a thickness of 1.6 mm and a half-cell volume of 0.35 cm^3. Chemically compatible diaphragm pumps (model FF-12, 1/428 fittings, DCB-4 wire control, FS 60X PEEK prefilter, KNF Neuberger, UK) were used for all experiments. Flow rates of 10 $mL\,min^{-1}$, 26 $mL\,min^{-1}$, and 51 $mL\,min^{-1}$ were employed, corresponding respectively to linear flowrates past the separator of 1.0 $cm\,s^{-1}$, 2.5 $cm\,s^{-1}$, and 5.0 $cm\,s^{-1}$, as explained in Appendix 2.A.1.

2.2.3 Cycling procedure

An Autolab PGSTAT 302N potentiostat (Metrohm, UK) was used to cycle the $V(acac)_3$ RFB. For charge/discharge tests, cells were charged up to 20% of the theoretical maximum state of charge (SOC), as computed via coulomb counting, at 10 mA cm^{-2} (22 mA). Cells were charged only to a theoretical SOC of 20% to minimize self-discharge and extend battery lifetime, and a lower current density was used to ensure reproducible results. Voltage cutoffs of 3.0 V for charging steps and 1.3 V for discharging steps were applied. Cells were held at open circuit (a 0 A applied current) for 15 seconds between charging and discharging steps to monitor the open-circuit potential as it relaxed.

Impedance measurements were conducted using an FRA32 module on the potentiostat. Impedance spectra were gathered every 10 cycles at 0% SOC (as established by an open-circuit hold after the cell discharged to 1.3 V), unless otherwise mentioned. The signal amplitude was set to 10 mV and frequencies ranged from 0.1 Hz to 100 kHz with 5 points per decade. Measuring an impedance spectrum typically took two minutes.

Every self-discharge experiment was run with a similar protocol, built up from three different cycling procedures: a regular cycle, an impedance cycle, and a self-discharge cycle. In a regular cycle, the cell was charged up to 30% of its theoretical maximum SOC by coulomb counting at 20 mA cm^{-2} (44 mA), held at 0 A for 15 seconds, and subsequently discharged at 20 mA cm^{-2} down to 1.3 V. The impedance cycle was identical to the regular cycle, aside from a two-minute impedance measurement being taken immediately before discharging according to the protocol described above. In self-discharge cycles, the cell was charged up to 100% of its theoretical maximum SOC by coulomb counting, after which it was held at 0 A until the voltage dropped below 2 V. In all self-discharge experiments, a regular cycle was run first as a 'burn-in' step, followed by an impedance cycle. Then, a 10-cycle loop consisting of one self-discharge cycle, an impedance cycle, and eight regular cycles was initiated. The 10-cycle loop was continued until the

cell was unable to self-discharge fully, as indicated by a lack of an appreciable voltage change over an hour.

2.2.4 Experimental data

For clarity, not all of the charge/discharge cycling profiles and impedance spectra gathered are presented below. Results from every charge/discharge experiment and impedance measurement are publicly available in the Oxford University Research Archive [74]. The repository also includes modified Matlab code for the adaptive observer along with outputs from the adaptive controller for all six self-discharge experiments.

2.3 Results and discussion

2.3.1 Cell performance

Saraidaridis reported stable cycling of $V(acac)_3$ for 160 cycles [69] and postulated that reservoir imbalance caused the cell's eventual failure. After adding a control system developed by Smith [73] to mitigate the imbalance, fairly rapid capacity fade and cell failure was repeatedly observed. The first 27 cycles of data in Fig. 2.1 show efficiency variations typical of these experiments. Similar trends have also been observed elsewhere [71].

Smith posited that pore clogging in the separator was the primary driver of performance fade [75]. As the pores within the membrane start to clog, the apparent coulombic efficiency of the cell rises, because smaller pores slow crossover of the active species. Once the membrane's pores drop below a critical size, exchange of the supporting electrolyte begins to be slowed, causing an apparent rise in membrane resistance and concomitant growth of charging and discharging overpotentials as shown in Fig. 2.1(a-c). These effects rationalize the monotonic rise in coulombic efficiency and decrease in voltaic efficiency that begins after cycle 6 and continues until cycle 27.

The data shown in Fig. 2.1 were produced by a cell in which the polarity was switched after cycle 28, i.e., the identities of the electrolyte reservoirs were

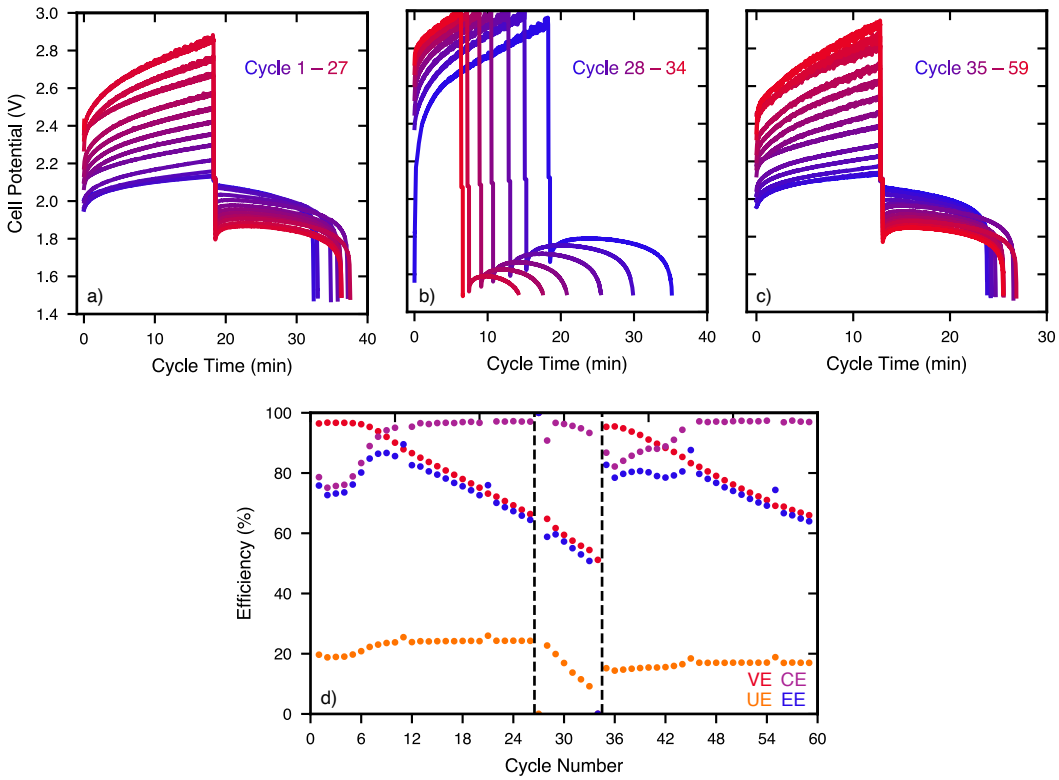

Figure 2.1: (a-c) Galvanostatic charge/discharge data and (d) voltaic (VE), coulombic (CE), utilization (UE), and energy (EE) efficiencies for the first 35 cycles for the 0.1 M $V(acac)_3$, 0.3 M $TEABF_4$ RFB in a countercurrent and zero-gap flow configuration with a microporous Celgard 4560 separator. The cell was cycled to a theoretical SOC of 20% via coulomb counting at 10 mA cm^{-2}. The positive and negative reservoirs were switched by discharging twice between cycles 28 and 34. After cycle 34, the separator was replaced.

swapped by running two discharge steps in a row. This polarity reversal did not significantly impact the rate of voltage-efficiency change, indicating that the source of performance loss in the first 34 cycles was not a unidirectional (diode-like) phenomenon. The coulombic efficiency slightly decreases by 5%, which is hypothesized to stem from the charged electrolyte within the membrane pores neutralizing its now oppositely charged counterpart. Note that decreasing utilization efficiencies during cycles 27-34 owe to the cell reaching its 3 V voltage cut-off before the targeted charge input.

The trend in voltaic efficiencies in this experiment indicate that membrane fouling occurs within the membrane matrix and is not reversible. This is further supported by the similarity of SEM images of the pristine and spent membrane (Appendix 2.A.2). At first glance the slight decrease in coulombic efficiency in Fig.

2.1(d) might suggest reversible membrane fouling. However, Fig. 2.1(a-c) show that the charging and discharging overpotentials only continue to increase from cycles 1 to 35. Notably, once the current direction is reversed at cycle 28, the discharging overpotential jumps from 0.15 V to 0.3 V. This suggests that fouling within the membrane matrix is not symmetric and biased towards the positive side.

Upon cell failure (cycle 34, at which utilization efficiency had dropped to nearly 0%), the porous separator and its flanking ePTFE gaskets were replaced, while all other cell components were retained. As can be seen in Fig. 2.1(d), cell performance was fully restored. Moreover, during cycles 35-60, the dynamical changes of coulombic and voltage efficiency seen in cycles 1-34 are essentially repeated, stemming from similar galvanostatic charge/discharge data shown in Fig. 2.1(c). Note that the ∼5% decrease in utilization efficiency after separator replacement owes to electrolyte loss during reassembly of the cell.

Cyclic voltammetry was performed on fresh and post-cycled $V(acac)_3$ electrolytes (Appendix 2.A.3), which both yielded similar voltammograms. These results support Smith's membrane fouling hypothesis, while contrasting other studies that point to degradation processes occurring at the negative electrode as the predominant cause of cell failure [71].

2.3.2 Canary cell experiments

After the microporous separator was identified as a main source of performance fade, a 3-cell experiment, in which two 'canary cells' were placed in series with the reactor being cycled, was conducted to probe whether performance of the Celgard 4560 separator changed during contact with charged electrolytes at open circuit. As shown in Fig. 2.2(a), both the positive and negative electrolytes were first passed in loops through canary cells at open circuit before flowing into the 'working cell', through which current was passed. No current was passed through the two canary cells, excepting the periods during which impedance spectra were gathered from them.

The cycling data and efficiencies from the working cell (Appendix 2.A.4) followed the same trends discussed above. Fig. 2.2(b-d) show stark differences between the

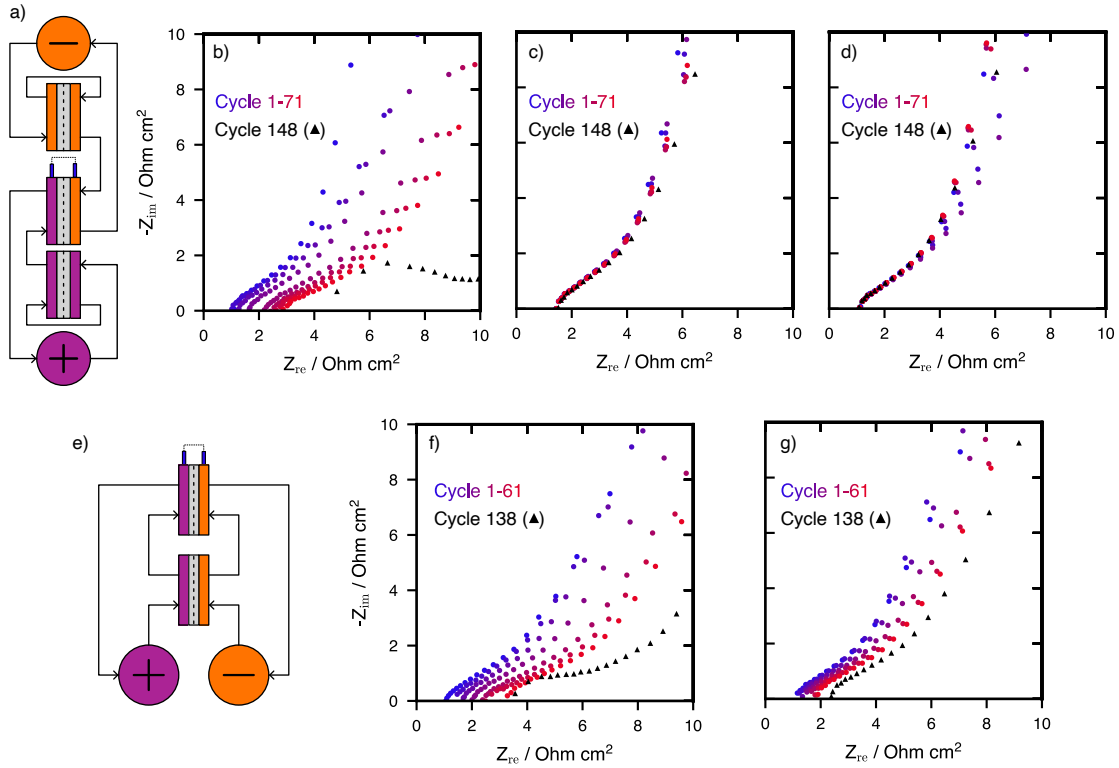

Figure 2.2: Electrolyte flow configuration and Nyquist plots for the (a-d) 3-cell and (e-g) 2-cell canary experiments. Solid arrows in (a,e) represent fluid flow while dotted lines between the blue current collectors represent current flow. An impedance measurement was taken for the (b,f) working and (c,d,g) canary cells every 10 cycles at 0% SOC (corresponding to a hold at 0 A applied current after discharge to 1.3 V). The signal amplitude was set to 10 mV and frequencies ranged from 0.1 Hz to 100 kHz with 5 points per decade.

impedance spectra of the canary cells and the working cell. The working cell's bulk area-specific resistance (ASR) – as determined by the high frequency real intercept – increases from 1.1 $\Omega\,\mathrm{cm}^2$ to 4.0 $\Omega\,\mathrm{cm}^2$ over 148 cycles. This is naturally explained by gradual pore clogging in the separator: a smaller average pore size decreases the effective conductivity, increasing the cell's bulk resistance. In contrast, the bulk ASRs in both canary cells remained constant. Note that the positive cell's ASR is 0.3 $\Omega\,\mathrm{cm}^2$ larger than the negative's, owing to different resistances of the electrical leads, carbon-wool packing, etc.

The low-frequency responses of the canary cells vary due to slight differences in the SOC. Recall that impedance measurements were taken at 0% SOC as determined by holding at open circuit after the low-voltage cutoff was exceeded. Below 1.3 V,

the slope of the open-circuit potential curve varies strongly with SOC. Because this effect manifests as an apparent zero-frequency admittance (inverse capacitance), small variations in the SOC near the cutoff voltage strongly impact the cell's low-frequency impedance response. Variations in the low-frequency imaginary impedance components of both canary cells were essentially random across cycles, but the variance was higher in the negative canary.

Excluding the differences in the low-frequency regime, the relatively constant impedance responses of both canary cells at moderate-to-high frequencies confirm that the Celgard 4560 separator remains stable in contact with charged electrolytes of either sign. Indeed, both canary cells were cycled after being disconnected from the 3-cell experiment and proceeded to indicate the pore clogging signature seen in the working cell: voltaic efficiency decreased monotonically and coulombic efficiency rose sigmoidally. This observation is consistent with a hypothesis that pore clogging results from polarization of the cell – either a potential gradient associated with applied current or a concentration gradient associated with differences in charge state between solutions on either side of the membrane.

A 2-cell canary experiment was designed to probe the distinct effects of concentration and potential differences on membrane performance. In this configuration, shown in Fig. 2.2(e), the negative and positive electrolytes were passed through a canary cell before entering the working cell to experience applied current.

Similar to the 3-cell canary experiment, no current was passed through the concentration-polarized canary cell except during the periodic impedance measurements. This 2-cell experiment investigates a situation in which the working cell experiences forces that drive both diffusion and migration of electrolyte constituents across the membrane, whereas the canary cell only experiences a diffusion driving force. Nyquist plots for the working and canary cell are presented in Fig. 2.2(f,g). The bulk ASR increases in both cells as they cycle, but does so more slowly in the concentration-polarized canary cell. Over 138 cycles, the working cell's ASR increased by 220%, while the canary cell's rose by 120%. The combination of canary cell experiments proves that none of the species (charged or neutral) are solely

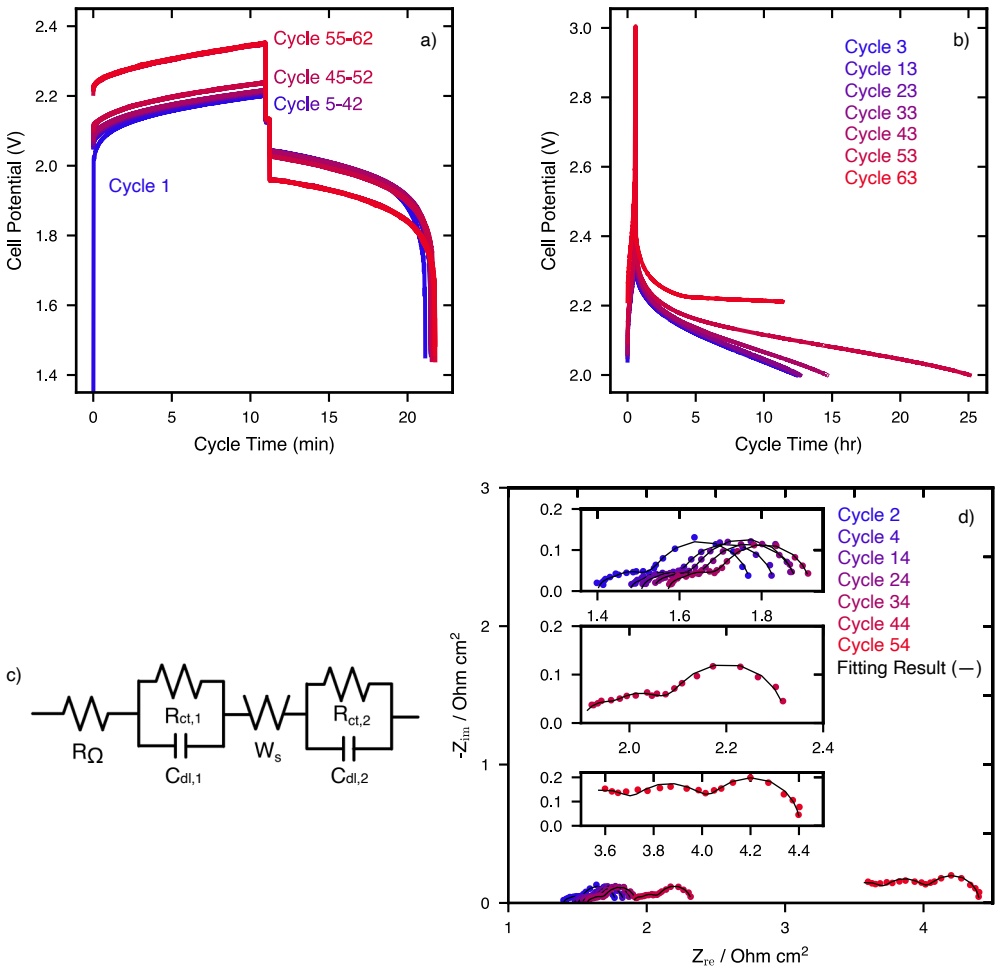

Figure 2.3: (a) Charge-discharge curves for the 0.1 M $V(acac)_3$/0.3 M $TEABF_4$/ACN RFB chemistry with a Daramic-175 porous separator, a current density of 20 mA cm^{-2}, and a mean linear flow velocity of 5.0 cm s^{-1} (b) Self-discharge curves (hold at 0 A applied current), until a voltage cutoff of 2.0 V was reached, were conducted every 10 cycles. (c) Equivalent circuit model that was used to fit the (d) impedance data that was collected between each self-discharge cycle.

responsible for membrane fouling, but rather the driving forces of migration and diffusion appear to propel the rise in separator resistance.

2.3.3 Evolution of crossover rates

Self-discharge tests were perfomed using the protocols described in section 2.2.3 with Daramic 175 and Celgard 4560 microporous separators and at three different electrolyte flow rates. Fig. 2.3 presents representative data from the cell with a Daramic 175 separator and a 51 mL min^{-1} (5.0 cm s^{-1}) electrolyte flow rate. After every 10th cycle of charge-discharge, an impedance measurement was taken,

after which the cell was charged via coulomb counting to 100% of the theoretical maximum SOC (assuming no crossover) and self-discharge was tracked. The charge–discharge data shown in Fig. 2.3(a) are similar to those seen in Section 2.3.1, but the charging and discharging overpotentials increase sharply after the self-discharge cycles, presumably because of the larger swings in SOC before them. Fig. 2.3(b) shows that the time to discharge to 2 V increases for each self-discharge cycle, consistent with the increasing coulombic efficiency trend seen in Fig. 2.1. SEM images of the fresh and spent Daramic separator (analogous to the Celgard separator shown in Appendix 2.A.2) were not acquired; however, the similarity in cycling behavior suggests that, as with Celgard, any membrane evolution occurs within the bulk matrix rather than at the surface.

Impedance data were fitted to the equivalent circuit model depicted in Fig. 2.3(c). The cell resistance (R_Ω) is in series with both the negative ($R_{\mathrm{ct},1}$) and positive ($R_{\mathrm{ct},2}$) charge-transfer resistances and double-layer capacitances ($C_{\mathrm{dl},1}$ and $C_{\mathrm{dl},2}$). A finite-length Warburg element (W_s) was added between the two interfacial reaction impedances to account for diffusion across the membrane. The fitted parameter that changed most was cell resistance: cycle 2 yielded a bulk ASR of 1.40 $\Omega\,\mathrm{cm}^2$, which rose to 3.44 $\Omega\,\mathrm{cm}^2$ by cycle 54. The full list of fitted parameters is presented in Table S6. Similar trends were seen across all three flow rates and with both separators.

An adaptive observer governed by an isothermal, zero-dimensional ('stirred-tank') lumped-parameter model was reported earlier by Ascencio et al. [76]. The adaptive observer dynamically estimates crossover rates during each self-discharge cycle given the state of charge of the cell. Notably, Ascencio's model does not assume that species fluxes through the separator are proportional to the concentration difference across it (Fickian diffusion). Rather, the SOC and crossover flux are estimated simultaneously, allowing for signatures of more complex transport behavior to be extracted from the experimental voltage data.

Generally, the molar crossover flux Q_x of a charged species across a planar membrane normal to the x direction is expected to scale with the exposed membrane area A_x and the concentration of the charged species. To first order, the relationship

among these quantities can be parametrized by a mass-transfer coefficient k_{mt} with units of velocity, as

$$Q_x = k_{\mathrm{mt}} A_x c_0 \mathrm{SOC}_{\mathrm{cell}}, \tag{2.4}$$

where c_0 is the active-species concentration in the fully discharged electrolyte and $\mathrm{SOC}_{\mathrm{cell}}$ is the SOC in the cell, which generally exceeds the reservoir SOC because the electrolytes accumulate excess charge during their residence time in the reactor chamber. For simple Fickian diffusion across the membrane, k_{mt} is expected to be a constant, proportional to the effective diffusivity of active species and inversely proportional to the membrane thickness. When diffusion is Fickian, the active observer is expected to show that Q_x varies in direct proportion to $\mathrm{SOC}_{\mathrm{cell}}$.

Fig. 2.4 shows crossover-rate estimates from the adaptive observer for both separators at three different mean linear velocities of 1.0 $\mathrm{cm\,s^{-1}}$, 2.5 $\mathrm{cm\,s^{-1}}$ and 5.0 $\mathrm{cm\,s^{-1}}$. At the onset of cycling, the crossover is Fickian across both separators in all cases. These initial data sets were used to estimate k_{mt} values by linear regression; the dashed lines present the best-fit curves, and corresponding k_{mt} values derived from their slopes are written on the graphs in Fig. 2.4.

With the possible exception of Celgard at a 1.0 $\mathrm{cm\,s^{-1}}$ flowrate, k_{mt} for a particular membrane does not vary significantly with linear flowrate, suggesting that the flow in the reactor chamber was well-developed and turbulent. Linear regression shows that Daramic and Celgard have mass transfer coefficients of 3.7 $\mu\mathrm{m\,s^{-1}}$ and 6.4 $\mu\mathrm{m\,s^{-1}}$, respectively, with a 1.0 $\mathrm{cm\,s^{-1}}$ linear flowrate through the reactor. The higher mass transfer coefficients seen for Celgard are consistent with the lower coulombic efficiencies they exhibit compared to the Daramic separator [77].

The k_{mt} value remains essentially unchanged for Daramic as flowrate rises, signifying that convection has little impact on the initial crossover rate of active species. For Celgard, the mass-transfer rate does increase by about 15% as the flowrate increases from 1.0 $\mathrm{cm\,s^{-1}}$ to 4.9 $\mathrm{cm\,s^{-1}}$. It appears that most of this increase occurs between the flowrates of 1.0 $\mathrm{cm\,s^{-1}}$ and 2.5 $\mathrm{cm\,s^{-1}}$. Possibly there is a critical flow rate at which the flow becomes well-developed and turbulent within the reactor

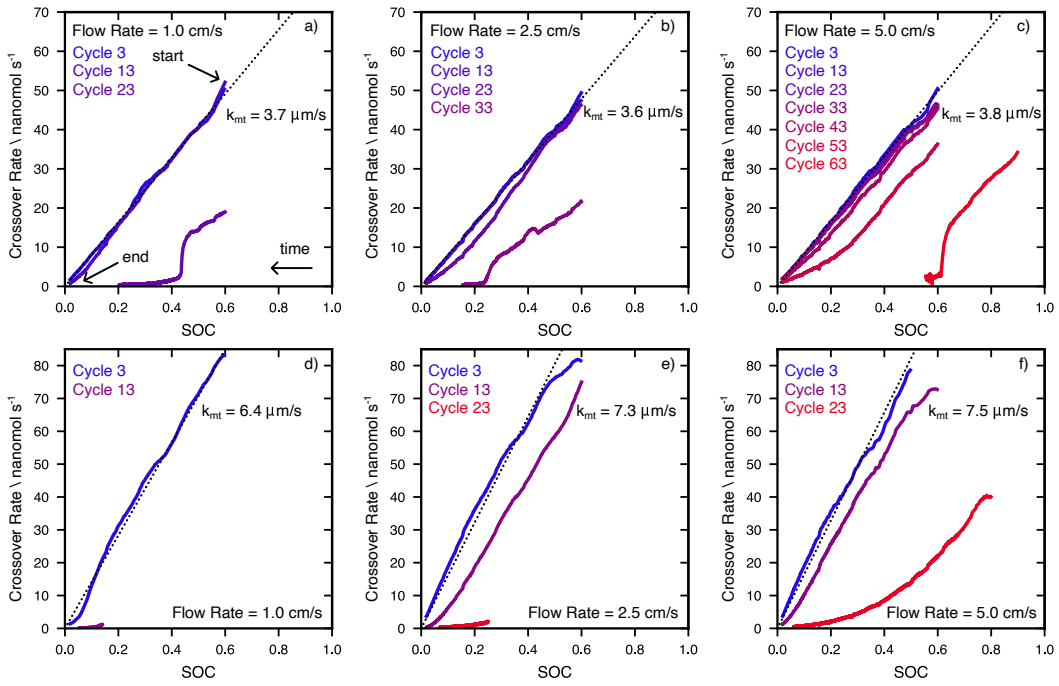

Figure 2.4: Crossover estimation for each self-discharge cycle for the Daramic-175 (a-c) and Celgard 4560 (d-e) separators. Three mean linear flow rates of 1.0 cm s^{-1} (a,d), 2.5 cm s^{-1} (b,e), and 5.0 cm s^{-1} (c,f) were tested. An adaptive observer was used for estimating all crossover rates [76]. The mass transfer coefficient (k_{mt}) was obtained with a linear fit of the crossover estimation from the first self-discharge cycle (cycle 3) in conjunction with the exposed membrane area A_x of 2.20 cm^2. The coefficient of determination (R^2) was greater than 0.99 in all instances.

chamber, such that k_{mt} ceases to change. Given, the electrolyte's viscosity of 0.535 cP [69] and reactor dimensions, turbulent mixing (Re $>$ 4000) would occur at a linear flow rate of 16 cm s^{-1}—within an order of magnitude of the tested flow rates. The experimentally reported linearized velocities do not account for the tortuosity and compression of the porous electrode, suggesting that their true values are larger than reported. Note that a similar trend was seen for the Daramic separator at flow rates below 1.0 cm s^{-1} but the long residence times at these low rates led to very high per-pass conversion, and consequently large overpotentials, that caused the voltage cutoffs to be reached before significant amounts of charge could be exchanged at the current density used for these experiments.

As cycling progresses for each cell, the adaptive observer shows that the law governing crossover deviates from the expected Fickian response. For example, the Daramic cell operating at a linear flow rate of 5.0 cm s^{-1}, shown in Fig. 2.4(c),

maintains a constant, Fickian mass transfer coefficient for the first 33 cycles. During cycles 43 and 53, the crossover rate begins to be suppressed at low SOC; after reaching SOC greater than 40%, however, the slope of the crossover vs. SOC curve reaches a value commensurate with the k_{mt} observed in earlier cycles. By cycle 63, the crossover rate suddenly drops to roughly zero below 60% SOC. Similar trends are seen for the 1.0 $\mathrm{cm\,s^{-1}}$ and 2.5 $\mathrm{cm\,s^{-1}}$ flow rates, although the cells survive for fewer cycles.

Remembering that SOC is a proxy for the concentration polarization across the membrane, and consequently with the thermodynamic force that drives diffusion, the trends exhibited in Fig. 2.4 are commensurate with pore clogging. As outlined in Appendix 2.A.6, both fresh Daramic and Celgard separators have an average pore size that is much larger than the atomic radii of the active species, resulting in a linear relationship between crossover and SOC. We hypothesize that as cycling proceeds the average pore sizes decrease and pore size distributions possibly altered. The qualitatively distinct fouling signatures between Daramic (sudden drop in crossover rate) and Celgard (gradual decrease in crossover rate) have been hypothesized to stem from differences in their mechanical properties and microstructure detailed in Appendix 2.A.6. [78].

2.4 Conclusions

Although side reactions have been proposed as the predominant degradation pathway for the $V(acac)_3$/ $TEABF_4$/ACN RFB chemistry, we observe that membrane fouling is the predominant driver of cell failure. The widely reported increase in coulombic efficiency and steady drop in voltage efficiency over the first few dozen cycles relates to changes in the membrane separator, rather than deterioration of the active electrolytes. After replacement of the Celgard membrane, the initial capacity and efficiency metrics of a flow reactor were recovered entirely.

This chapter shows that similar porous membranes can result in distinct fouling signatures. Additionally, the Celgard and Daramic porous separators foul at significantly different rates. Although the exact mechanism of fouling is not shown, additional cross-sectional SEM imaging could reveal insight into the distribution of

pore clogging. Membranes could also be imaged at various stages of cell cycling to observe the evolution of pore sizes during cycling to further confirm the hypothesis set out in this chapter. The next chapter attempts to better understand how cycling protocols, operating conditions, and flow reactor design can impact pore clogging.

If the membrane-fouling problem can be solved, porous separators with appropriate modifications may allow coulombic efficiencies comparable to those achieved with more costly bespoke ion-exchange membranes. Canary cells showed that Celgard 4560 is stable and maintains a constant resistance when exposed to both positively and negatively charged electrolyte solutions. The resistivity increased when exposed to current and, less significantly, when exposed to an electrolyte composition difference. Our observations suggest that the resistance rises can be explained by pore clogging, although the signature of this effect differ between Daramic and Celgard.

In the initial cycles, the variation of crossover rates with SOC across both porous separators was consistent with a Fickian diffusion process. Mass-transfer coefficients did not vary significantly with electrolyte flowrate and were 3.8 and 7.5 μm s^{-1} at mean linear flow rates of 5.0 cm s^{-1} for Daramic-175 and Celgard 4560, respectively. Crossover rates deviated from Fickian responses as membrane fouling progressed. The crossover rate dropped suddenly at a rising threshhold SOC for Daramic-175, whereas it gradually dropped with respect to SOC for Celgard 4560.

2.A Appendices

2.A.1 Flow cell reactor schematics

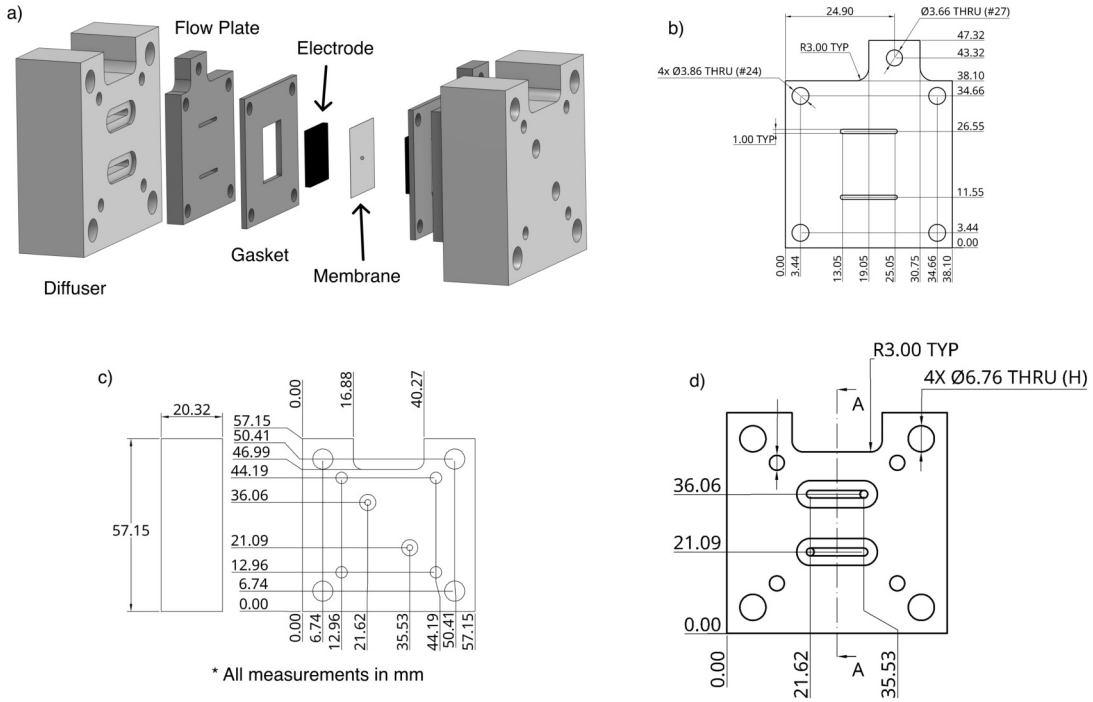

Figure 2.5: (a) Schematic for flow cell reactor, (b) flow plate, and (c-d) diffuser plate. All measurements are reported in millimetres. The exposed membrane and electrode area has height of 1.64 cm (parallel to flow) and a width of 1.34 cm, resulting in a cross-sectional area of 2.20 cm^2. The compressed width and porosity of the electrode is 1.6 mm and 80% respectively. Thus, the open cell area normal to flow is 0.17 cm^2. Flow rates are reported as mean linear flow rates across the separator. With this reactor geometry, a 1.0 cm/s, 2.5 cm/s, and 5.0 cm/s linear flow rate corresponds to 10 mL/min, 26 mL/min, and 51 mL/min respectively.

2.A.2 SEM images of Celgard 4560 separator

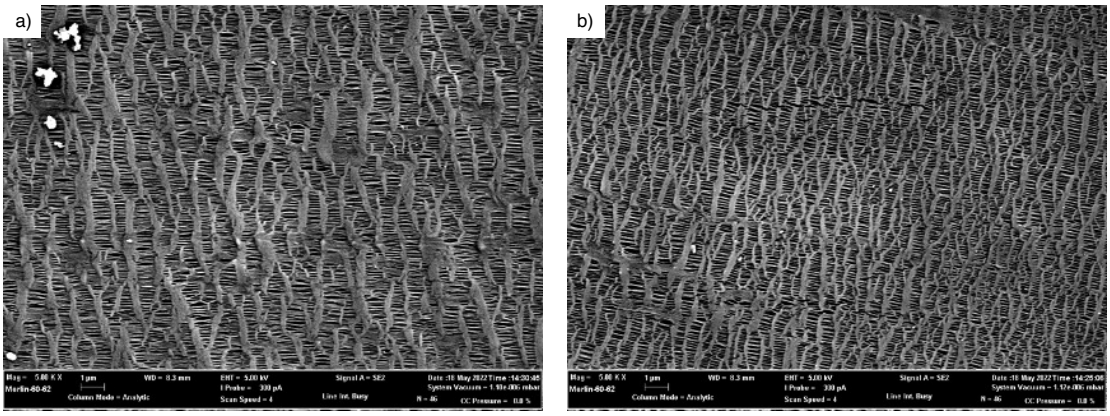

Figure 2.6: SEM images of a porous Celgard 4560 membrane (a) in pristine condition and (b) upon cell failure. Images were acquired using a Zeiss Merlin microscope in secondary electron (SE2) mode at an accelerating voltage of 5.0 kV, probe current of 300 pA, and working distance of 8.3 mm. The magnification was 50,000×, corresponding to a scale bar of 1 µm. Images were collected in analytic column mode with a scan speed of four.

2.A.3 Cyclic voltammograms of electrolyte

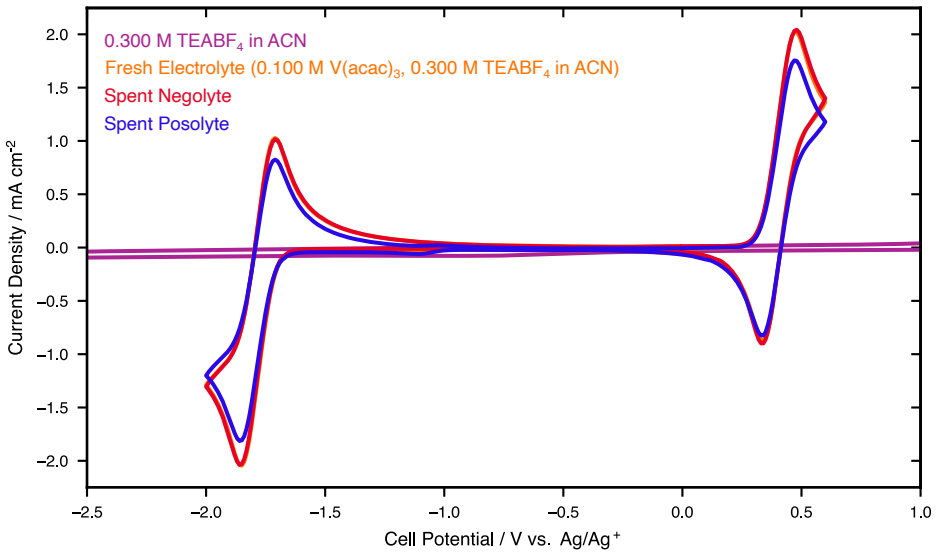

Figure 2.7: Cyclic Voltammograms of fresh (0.1 M $V(acac)_3$/0.3 M $TEABF_4$ in ACN) and spent electrolytes at a scan rate of 50 mV/s on a glassy carbon working electrode at 23°C.

2.A.4 Galvanostatic cycling data for 3-cell canary experiment

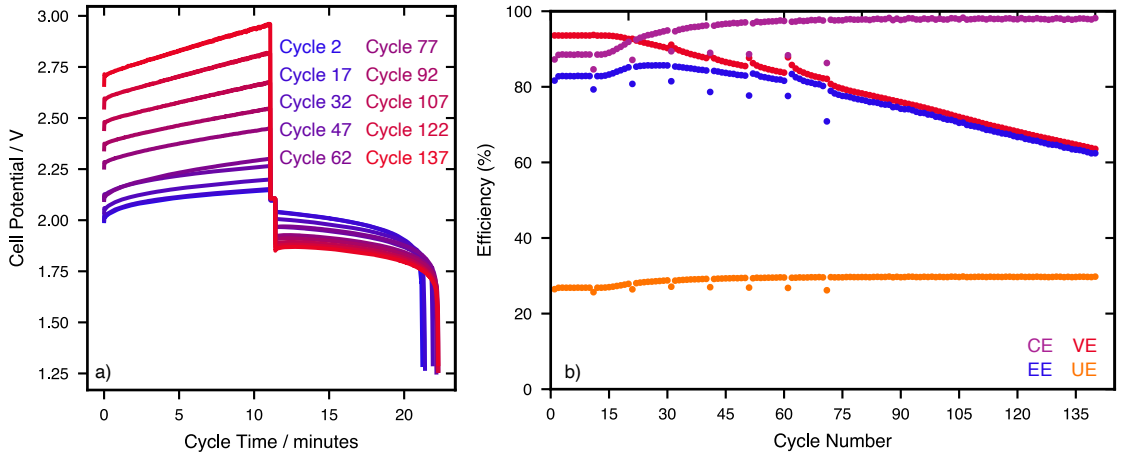

Figure 2.8: (a) Voltage data from the working cell of the 3-cell canary experiment. Every 15^{th} charge/discharge curve is plotted started from cycle 2. (b) The computed coulombic, voltaic, utilization, and voltaic efficiencies for the same cell. Impedance measurements were taken every 10^{th} cycle until cycle 71 at 0% SOC after cell equilibration. This results in lower energy efficiencies during each "burn-in" cycle. The electrolyte consisted of 0.1 M $V(acac)_3$/0.3 M $TEABF_4$ in ACN with a Celgard 4560 porous separator. The cell was cycled at 20 mA/cm^2 to 30% SOC via coulomb counting at a flow rate of 5.0 cm/s.

2.A.5 EIS parameter fits

Cycle #	R_Ω (Ω cm^2)	$R_{ct,1}$ (mΩ cm^2)	$C_{dl,1}$ (mF cm^2)	$R_{ct,2}$ (mΩ cm^2)
2	1.40 ± 0.002	33.5 ± 5.85	18.5 ± 3.69	52.8 ± 5.90
4	1.48 ± 0.003	25.2 ± 4.44	18.8 ± 4.96	54.9 ± 4.47
14	1.51 ± 0.003	30.3 ± 8.22	27.4 ± 6.40	47.2 ± 8.23
24	1.53 ± 0.002	34.8 ± 5.49	29.3 ± 4.88	42.9 ± 5.82
34	1.57 ± 0.002	31.3 ± 6.04	28.0 ± 5.56	48.0 ± 6.01
44	1.90 ± 0.004	58.7 ± 5.14	10.9 ± 1.88	74.4 ± 5.04
54	3.44 ± 0.021	25.4 ± 18.4	1.02 ± 0.186	254 ± 9.16
Cycle #	$C_{dl,2}$ (mF cm^2)	$W_s - Z_0$ (Ω cm^2)	$W_s - \tau$ (s)	
2	89.8 ± 22.7	0.288 ± 0.003	0.739 ± 0.019	
4	81.6 ± 15.6	0.274 ± 0.003	0.755 ± 0.019	
14	112 ± 42.0	0.301 ± 0.004	0.879 ± 0.025	
24	137 ± 38.4	0.274 ± 0.002	0.781 ± 0.014	
34	135 ± 38.1	0.269 ± 0.003	0.778 ± 0.022	
44	92.6 ± 14.8	0.287 ± 0.004	0.808 ± 0.024	
54	20.4 ± 1.69	0.456 ± 0.008	0.433 ± 0.018	

Table 2.1: EIS parameters of 0.1 M $V(acac)_3$/0.3 M $TEABF_4$ in ACN in a RFB with a Daramic separator. The estimated errors for each parameter are the 95% confidence interval for the corresponding equivalent circuit.

2.A.6 Porous separator properties

Property	Celgard 4650	Daramic 175
Thickness (µm)	115	175
Tensile Strength (MPa)	12.7	15.08 [79]
Porosity (%)	55	58
Average Pore Size (nm)	64	100
Material	Polypropylene	Polyethylene

Table 2.2: Properties of the microporous Celgard 4650 and Daramic 175 separators.

3

Mitigating Membrane Fouling in Redox Flow Batteries

Contents

3.1 Introduction

Membranes play a critical role in the performance and longevity of redox flow batteries (RFBs) [80], yet membrane research for non-aqueous RFBs (NARFBs) is still in its early stages [81]. Many studies rely on commercial membranes designed for aqueous systems, such as Nafion, which exhibit poor structural stability in organic solvents [77]. As a result, most advancements in NARFB technology have been driven by improvements in active species and reactor engineering [72]. The viability of NARFB systems for long-term cycling remains largely unproven. Addressing this gap requires a deeper understanding of membrane structure–property relationships and the dynamics of ion transport in non-aqueous systems. Porous separators such as Celgard and Daramic offer an alternative to expensive and unstable ion-exchange membranes, but their use in asymmetric systems leads to rapid electrolyte degradation due to high active species crossover. Currently, few membranes provide both high ionic conductivity and low permeability of redox-active species in non-aqueous systems.

This chapter aims to address membrane instability in NARFBs by investigating the impact of flow configurations on the long-term performance of porous separators. Chapter 2 identified membrane fouling as the primary cause of capacity fade in porous separators, despite their mechanical robustness [82]. A sigmoidal increase in coulombic efficiency and rising bulk resistance were identified as key indicators of membrane degradation. These signatures in cycling-perfomance data have been observed in many flow battery studies [83, 84].

This chapter, like the previous one, uses the stable non-aqueous vanadium acetylacetonate ($V(acac)_3$) electrolyte to isolate membrane and flow-related effects. It introduces two key strategies to mitigate membrane fouling in the $V(acac)_3$ RFB: (1) optimizing flow field configurations and (2) implementing an electrolyte rebalancing system. Switching from counter-current to co-current flow dramatically reduces fouling in the Daramic porous separator, while addressing reservoir imbalance effectively eliminates capacity fade and enables stable long-term cycling.

The significant benefits of reservoir balancing motivated the design of a user-friendly PID control system tailored for the RFB research community. To support researchers who typically avoid reservoir balancing due to its complexity, this work provides a detailed guide to simplify the setup process. Furthermore, to account for the relatively high permeability of porous separators, the study investigates how flow configuration affects voltaic efficiency. By testing two extreme aspect ratios, it establishes the relationship between pumping losses, flow configuration, and overall cell performance.

3.2 Experimental

Unless specified otherwise, all chemicals and materials were used without further modification. Cycling experiments and electrolyte handling were performed within an Inert Pure LabHE glovebox filled with argon (99.998%, BOC, UK), maintaining atmospheric water and oxygen levels below 0.5 ppm.

3.2.1 Electrolyte preparation

Molecular sieves (4 Å, Fisher Scientific, UK) were vacuum-dried at 250 °C for 24 hours and transferred to the glovebox while still warm. HPLC-grade acetonitrile (Thermo Fisher, 99.9%, UK) was degassed using argon and purified through a PureSolv-Micro solvent purification system (Inert, UK). The purified acetonitrile (ACN) was then brought into the glovebox and further dried over molecular sieves. After 48 hours of drying, water content was verified to be below 0.5 ppm using a C30 Karl Fischer Coulometric Titrator (Mettler-Toledo, UK). $V(acac)_3$ (98%, Strem, UK) was recrystallized using anhydrous ACN and subsequently washed with anhydrous diethyl ether (Honeywell, 99.5%, UK) inside the glovebox. The purified $V(acac)_3$ crystals were dried and stored in the glovebox. Tetraethylammonium tetrafluoroborate ($TEABF_4$, 99%, Sigma, UK) was stored in the glovebox and used without further modification. Each cycling experiment used a total of 20 mL of electrolyte (10 mL for each tank).

3.2.2 Reactor design

This chapter utilizes two distinct reactor designs, both employing flow-through flow fields. The flow-field shape was held constant in the first reactor, referred to as Cell 1, which produced the results in Sections 3.3.1 and 3.3.2. A second reactor, Cell 2, was designed to investigate the impact of different flow-field configurations, as described in Section 3.3.3. Detailed reactor dimensions and schematics can be found in Appendix 3.A.1 and 3.A.2. All experiments were conducted using a porous Daramic 175 separator, which was rinsed with anhydrous ACN prior to use.

The reactor design for cell 1 matches that used and developed by Smith et al. in a previous study [73, 85]. This reactor featured a separator area of 2.20 cm^2 aligned with the flow direction and a compressed depth of 1.6 mm perpendicular to the flow. Flow reactors were assembled and operated within the glovebox. The electrodes, composed of 3.18 mm thick carbon felt (Alfa Aesar, UK), were vacuum-dried at 250 °C for 48 hours before reactor assembly. Expanded polytetrafluoroethylene (ePTFE, Gore, USA) gaskets were placed between the resin-impregnated graphite plate (Graphite-Store, USA) and the separator. The reactor assembly was secured using four screws tightened to a torque of 4.5 $N \cdot m$. Once fully compressed, the reactor maintained a thickness of 1.6 mm with a half-cell volume of 0.35 cm^3. All experiments employed chemically compatible diaphragm pumps (model FF-12, 1/4-28 fittings, DCB-4 wire control, FS 60X PEEK prefilter, KNF Neuberger, UK). For Cell 1, all experiments used a flow rate of 26 mL/min, corresponding to a mean linear flow velocity of 2.5 cm/s parallel to the separator.

The reactor design for Cell 2 has a separator area of 3.0 cm^2 for all tested flow fields. The electrodes, graphite plates, separator, and pumps consisted of the same material and thickness as Cell 1, however the gaskets were 1/16 inches (1.59 mm) rather than 1/8 inches (3.18 mm). This cell was compressed to a higher torque of 5.0 $N \cdot m$. Once fully compressed, the reactor maintained a thickness of 3.0 mm with a half-cell volume of 0.9 cm^3. Two different flow rates were tested: 26.8 mL/min and 79.5 mL/min.

3.2.3 Cycling procedure

A Metrohm Autolab PGSTAT 302N potentiostat (UK) was used to cycle the $V(acac)_3$ RFB. Unless otherwise mentioned, all experiments utilized the following procedure. Cells were charged to 20% of the theoretical maximum state of charge (SOC), determined via coulomb counting, at a current density of 20 mA cm^2. Voltage cutoffs were set at 3.0 V for charging and 1.3 V for discharging. To monitor the relaxation behavior of the open-circuit potential, cells were held at open circuit (0 A applied current) for 15 seconds between charging and discharging steps.

Electrochemical impedance spectroscopy (EIS) was performed using the potentiostat's FRA32 module. Unless stated otherwise, impedance spectra were recorded every 10 cycles at 0% SOC, determined by an open-circuit hold after discharging to 1.3 V. The measurements were conducted with a 10 mV signal amplitude over a frequency range of 0.1 Hz to 100 kHz, with five points per decade. Each impedance spectrum acquisition took approximately two minutes.

3.2.4 Reservoir balancing setup

Reservoir imbalance arises from direct flow of electrolyte through the separator from one reactor chamber to the other. This flow can be driven either by mechanical pressure or osmotic pressure, and ultimately leads to a liquid-volume difference between the electrolyte tanks (note the liquid-height difference in Fig. 3.1(b)). Mechanically, head losses in the two pipelines leading into the reactor inevitably differ. This causes slight pressure differences between the inlet flow streams, which ultimately drive interchamber flow. Osmotic pressure arises from concentration polarization or chemical change in the reactant flow streams; differences in mixing free energy between the solutions in the reactor chambers cause a thermodynamic pressure difference, which also drives interchamber flow.

A purely mechanical reservoir balancing strategy was designed, in which pressure differences between reactor chambers were counterbalanced by regulating the flowrates into them. Pressure losses in the feed lines are proportional to the flowrates through them, and flow between reactor chambers leads to a height difference

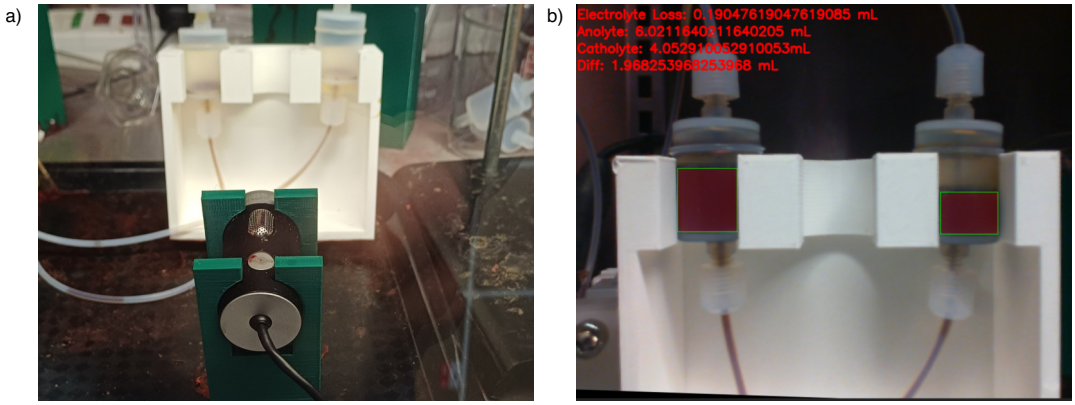

Figure 3.1: (a) The reservoir and camera holders used in the volume balancing scheme. A small PLA connector links the two at their bases to fix their relative positions and achieve consistent imaging. (b) Visualization of the image segmentation results. Segmentation masks for the electrolyte detection are superimposed on the reservoirs, accompanied by volume estimates.

between electrolyte reservoirs. Hence, the difference between inlet flowrates was varied to control the liquid heights.

Image processing from digital video was used to determine liquid volumes. Cylindrical reservoirs were securely positioned opposite a camera within a 3D-printed polylactic acid (PLA) scaffold, as shown in Fig. 3.1(a). During RFB operation, images of the reservoirs are captured every second and processed through a segmentation pipeline. Assuming a constant reservoir cross-section, the segmentation mask is mapped to a fluid volume using a user-defined conversion factor in mL/pixel (Fig. 3.1(b)). The volume difference between the two reservoirs serves as the control input to a PID scheme, which adjusts the differential pump duty cycle – and consequently, the flow rate – of the diaphragm pumps. This is implemented by maintaining one pump at a base duty cycle while adjusting the other pump's duty cycle according to the PID output: if the output is positive, the anolyte flow rate increases; if it is negative, the anolyte flow rate decreases. Since the diaphragm pumps require a nonzero minimum duty cycle to start operating, this approach ensures the controller never drives them below their functional range.

To prevent erratic control behavior, a 60 s moving-average filter was applied to all volume readings before being fed into the controller, reducing the impact of random segmentation errors. Additionally, the derivative term of the PID controller

was set to zero to avoid amplifying any residual noise. While these measures slightly increased the controller's response time, the dynamics of volume imbalance were slow in comparison. Thus, despite potential suboptimal control performance, the system was more than sufficient to maintain near-zero imbalance.

3.3 Results and discussion

3.3.1 Counter-current vs. co-current flow

Chapter 2 demonstrated that the primary mechanism of capacity fade in the $V(acac)_3$ electrolyte system is membrane fouling [82]. Additionally, an increase in a cell's bulk area-specific resistance (ASR) was identified as a key indicator of pore clogging in Daramic and Celgard porous separators. Monitoring active species crossover rates during self-discharge experiments further revealed that fouling is driven by the time spent at high states of charge (SOC) and the magnitude of $V(acac)_3$ concentration gradients across the membrane.

To mitigate these concentration gradients, flow operation was switched from counter-current to co-current. Counter-current flow is widely employed in chemical engineering applications where maximizing temperature and concentration gradients enhances transfer efficiency [86]. In RFBs, exactly the opposite effect is desired: counter-current flows raise the driving force for active-species crossover, so co-current flows may be intrinsically preferable.

In the $V(acac)_3$ NARFB, counter-current operation generally maximizes concentration gradients of the neutral $V(acac)_3$ species. As the schematic in Fig. 3.2(a) shows, the highest concentration polarization of neutral $V(acac)_3$ occurs under counter-current flow. In contrast, Fig. 3.2(b) illustrates that co-current operation eliminates these gradients, significantly reducing concentration imbalances. Since any diffusion of charged active species across the membrane is rapidly neutralized, their concentration gradients cannot be meaningfully suppressed. Accordingly, only concentration gradients of the neutral $V(acac)_3$ species are considered. In the heuristic analysis shown in Fig. 3.2(c,d), diffusion across the membrane has been modeled with Fickian behavior and both dispersion and turbulent mixing

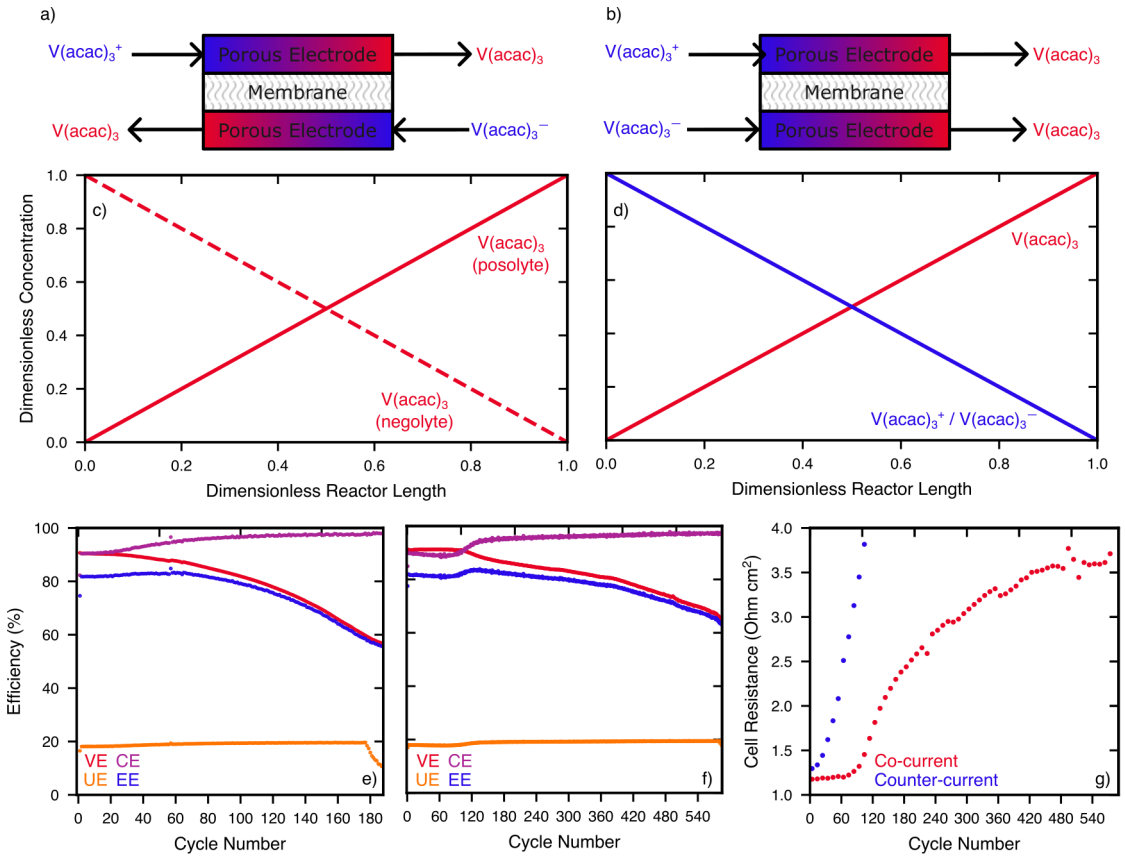

Figure 3.2: (a) Counter-current vs. (b) co-current operation of RFBs. Concentration profile of neutral $V(acac)_3$, and charged $V(acac)_3^+/V(acac)_3^-$ active species under (c) counter-current and (d) co-current operation. Voltaic (VE), coulombic (CE), utilization (UE), and energy (EE) efficiencies of the 0.1 M $V(acac)_3$, 0.3 M $TEABF_4$ nonaqueous RFB in (e) counter-current and (f) co-current flow. Both cells utilize a Daramic porous separator and are cycled to a theoretical SOC of 20% via coulomb counting at 20 mA cm^{-2}, resulting in a theoretical per-pass conversion of approximately 1% . (g) Bulk area-specific resistances from impedance measurements which were taken every 10 cycles. The galvanostatic cycling data and impedance spectra can be found in Appendix 3.A.3.

as flow progresses through the porous electrode have been neglected. The plotted dimensionless concentration is directly related to the local state of charge (SOC), which itself can be interpreted as a normalized concentration of active species. In the present experiments, the SOC window is intentionally limited to 0–0.2, so variations in dimensionless concentration reflect relatively small but spatially non-uniform deviations within this narrow operating range. Nevertheless, co-current operation would be expected to diminish neutral-species concentration polarization within the reactor much more than counter-current operation

Fig. 3.2(e-f) compares the cycling efficiencies of $V(acac)_3$ under co-current and

counter-current flow, with all other cycling conditions held constant. Both cells were charged to 20% SOC via coulomb counting (neglecting self-discharge) or until reaching an upper voltage cutoff of 3.0 V. The counter-current cell reached its voltage cutoff after only 177 cycles, whereas the co-current cell lasted 583 cycles without reaching the cutoff. Both cells exhibited the characteristic signatures of membrane fouling: a sigmoidal increase in coulombic efficiency and a monotonic decrease in voltaic efficiency, but the fouling was far slower in the co-current flow configuration. Note that the results in Fig. 3.2(e) differs from the results in chapter 2 due to different cycling conditions – notably a higher charging current density.

Fig. 3.2(e) presents the bulk ASR evolution for each cell over its cycling lifetime. Consistent with previous findings, membrane pore clogging led to increasing cell resistance in both cases. In both cells, there is an optimal amount of pore clogging such that CE rises faster than the VE decreases (i.e. EE is maximized). This is found to occur around a full cell resistance of 2.0 Ω cm^{-2}. The counter-current and co-current cells reached this bulk resistance after cycles 56 and 134, respectively. Using ASR as a quantitative metric of membrane fouling, we posit that the counter-current cell fouled more than two times faster than the co-current cell. This notable improvement underscores the critical role of flow field optimization, particularly in crossover-tolerant RFB systems that utilize porous separator membranes.

3.3.2 Effects of a PID level-balancing system

To further minimize V(acac)$_3$ concentration gradients, we addressed another significant factor: reservoir imbalance. Pump duties were initially calibrated using neutral V(acac)$_3$ solutions; however, over week-long experiments, small inaccuracies accumulate, leading to substantial electrolyte imbalance between the anolyte and catholyte. This issue is exacerbated by the fact that, during each cycle, the reservoir composition shifts from neutral to charged active species, altering key electrolyte properties such as viscosity. Also, the displacement pumps used to drive flow have inherent fluctuations in the flowrates they deliver, and these fluctuations may differ

in both amplitude and phase between pumps. As a result, an active management system is required to mitigate both short- and long-term electrolyte imbalances.

Smith et al. developed an image-based proportional–integral–derivative (PID) controller to regulate differential flow rates between electrolyte streams [73]. Their approach used an Otsu filter for liquid level detection in the reservoir. However, this thresholding method struggled with edge cases – such as bubble formation and inconsistent background lighting – resulting in frequent errors during long-term testing. To address these limitations, the updated level sensor utilized a convolutional neural network (CNN) segmentation pipeline. The LinkNet architecture, implemented using the *segmentation_models_pytorch* (SMP) Python library, was chosen for its ability to robustly handle common perturbations encountered during extended operation. The improved performance of this approach in challenging scenarios is demonstrated in Appendix 3.A.4.

The modified PID balancing system was implemented in a co-current flow cell to evaluate the impact of liquid imbalance on long-term cycling stability. The experiment spanned over two weeks and followed five distinct cycling protocols:

- Protocol I (Cycles 1 – 590 and 1191 – 1250): Charged to 20% SOC at 20 mA cm^{-2}
- Protocol II (Cycles 591 – 1170): Charged to 40% SOC at 40 mA cm^{-2}
- Protocol III (Cycles 1171 – 1190): Charged to 60% SOC at 40 mA cm^{-2}
- Protocol IV (Cycles 1251 – 1270): Charged to 100% SOC at 30 mA cm^{-2}
- Protocol V (Cycles 1271 – 1490): Charged to 100% SOC at 20 mA cm^{-2}

To demonstrate the stable reversibility of the $V(acac)_3$ electrolyte, the cell polarity was reversed at the transition between each protocol. This was achieved by performing two consecutive discharge steps, effectively swapping the identities of the anolyte and catholyte. For simplicity, Fig. 3.3(a) presents galvanostatic cycling data for Protocols I and II (1,170 cycles over 12 days). The complete cycling data set, covering all protocols, is provided in Appendix 3.A.5.

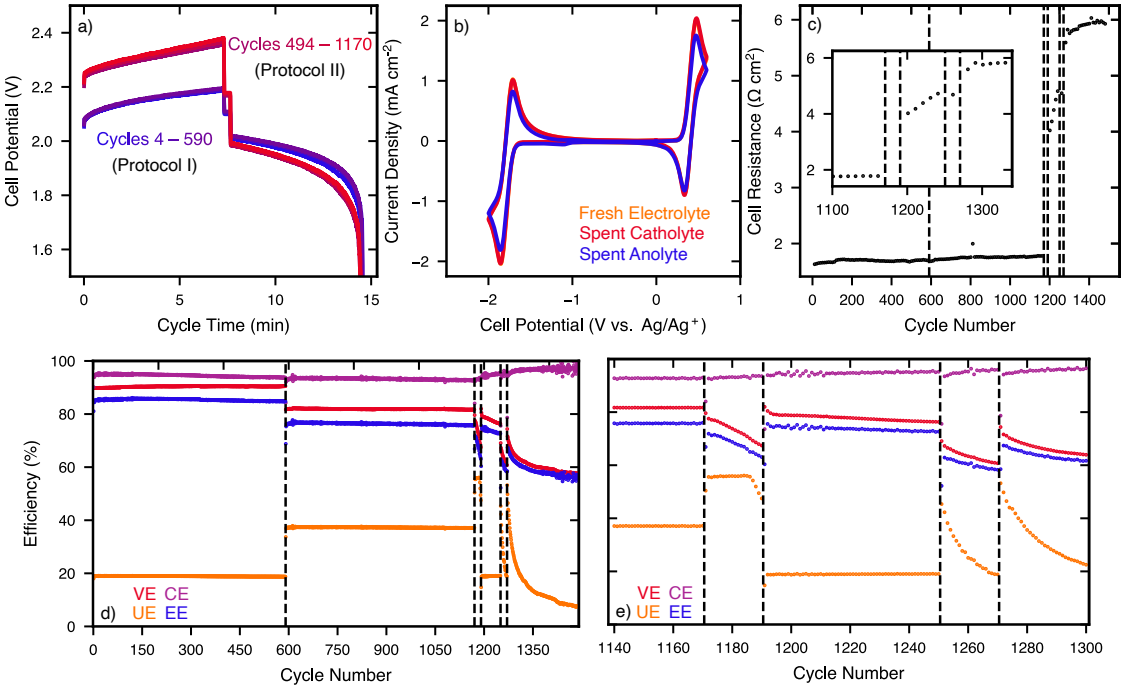

Figure 3.3: (a) Stable galvanostatic cycling data of the 0.1 M $V(acac)_3$, 0.3 M $TEABF_4$ nonaqueous RFB in co-current flow with an active PID controller to maintain equal liquid levels in each reservoir. Data for cycles 1,171 – 1,490 can be found in Appendix 3.A.5. (b) Cyclic voltammetry of the fresh and spent electrolytes after all 1,490 cycles. All measurements were taken with a scan rate of 50 mV/s (c) Bulk area-specific resistance of the cell during its lifetime. The full impedance spectra and their fits can be found in Appendix 3.A.6. (d,e) Voltaic (VE), coulombic (CE), utilization (UE), and energy (EE) efficiencies during each protocol. Black dotted lines indicate a transition between cycling conditions.

Fig. 3.3(b) shows cyclic voltammetry (CV) sweeps of both fresh and spent electrolytes, revealing minimal electrolyte degradation after 1,490 cycles. The slight difference in peak magnitudes in the spent anolyte is attributed to residual reservoir imbalance at the end of the experiment. Notably, upon completion of Protocol V, severe pore clogging prevented the PID controller from delivering sufficient interchamber pressure, leading to a steady ∼2 mL of liquid imbalance between the tanks.

Impedance measurements were recorded every 10 cycles to track the full-cell resistance throughout the experiment. Surprisingly, Fig. 3.3(c) shows that the co-current cell with PID control maintained stable cycling throughout Protocols I and II. In contrast, the co-current cell without PID level balancing reached an ASR

of 2.0 Ω cm^{-2} within just 134 cycles, whereas the PID-controlled system exhibited a significantly lower ASR of 1.78 Ω cm^{-2} even after 12 days of continuous cycling under more aggressive conditions. This stark difference underscores the critical role of active reservoir balancing in maintaining long-term cell performance. Note that after each protocol, the polarity was reversed, effectively swapping the identities of the anolyte and catholyte and flushing the pores of the membrane. This had no impact on the overall efficiency trends, and once membrane fouling began during Protocol III, flushing the membrane did not restore cell performance.

The efficiencies for the first two protocols are plotted in Fig. 3.3(d). Consistent with the stable cell resistance, all efficiency metrics remained relatively stable throughout the first 1,170 cycles. The total energy capacity fade (on a Wh/L basis) during Protocols I and II was 0.13% and 0.286%, respectively. For Protocol I, this corresponds to a fade rate of 0.0011% per equivalent cycle or 0.021% per day. Each equivalent cycle is defined as a full charge-discharge cycle to 100% SOC (i.e., five cycles of Protocol I correspond to one equivalent cycle). For Protocol II, the fade rates were 0.0012% per equivalent cycle or 0.048% per day.

The close agreement between the two protocols' fade rates on an equivalent cycle basis suggests that the observed capacity fade is primarily a function of cycling history rather than time or electrolyte degradation. This conclusion is further supported by the pristine condition of the spent electrolytes, as shown in Fig. 3.3(b). The stark contrast in performance between cells with and without a level-balancing system highlights the importance of eliminating reservoir imbalance effects when evaluating the stability of novel flow battery chemistries.

During Protocol III, the rapid increase in full-cell resistance led to a higher capacity fade rate. Once the cell reached its upper voltage limit of 3.0 V, the cycling protocol was reverted to Protocol I for 60 cycles. However, during these cycles, cell resistance continued to rise, resulting in lower energy and voltage efficiencies compared to the initial implementation of Protocol I (Cycles 1–590). This suggests that Protocol III induced a form of irreversible membrane fouling, preventing the cell from recovering its original performance.

In Protocols IV and V, the cycling conditions were pushed even further, exacerbating the degradation mechanisms. The characteristic signatures of membrane fouling were again observed, including a sigmoidal increase in coulombic efficiency and a progressive decline in voltage efficiency. The similarity in degradation patterns between the co-current cells with and without PID level balancing suggests that while $V(acac)_3$ concentration gradients are effectively minimized at lower current densities and SOCs, they do not completely prevent membrane fouling under more aggressive cycling conditions.

Recognizing the critical role of reservoir balancing in long-term RFB performance, a user-friendly program was developed to facilitate broader adoption within the RFB research community. The PID level-balancing code and accompanying program have been documented and published in a data repository [87]. To ensure accessibility, the program is designed for ease of use, allowing researchers with minimal coding or IT experience to install and implement a similar system effortlessly. The PID controller code is hardware-agnostic and compatible with various microcontrollers. Screenshots of the user interface and setup menu are shown in Fig. 3.4(a,b). Additionally, for users with programming experience who wish to modify the program's outputs, the source code is available in the following GitHub repository [87].

The software manages all aspects of pump control and volume rebalancing through an intuitive graphical user interface (GUI), requiring manual hardware wiring only during initial setup. This setup involves connecting each pump's control wire to any microcontroller pin that supports $analogWrite()$, while tachometer wires, if present, should be connected to digital interrupt-capable pins. Pinout diagrams for most Arduino-supported microcontrollers provide this information. Additionally, a common ground must be established by connecting the GND pin to the negative terminal of the DC bus supplying the pumps. Using these pin assignments, the program automatically generates microcontroller code to handle serial communication with the PC, control voltage output, and tachometer signal processing, as illustrated in Fig. 3.4(c).

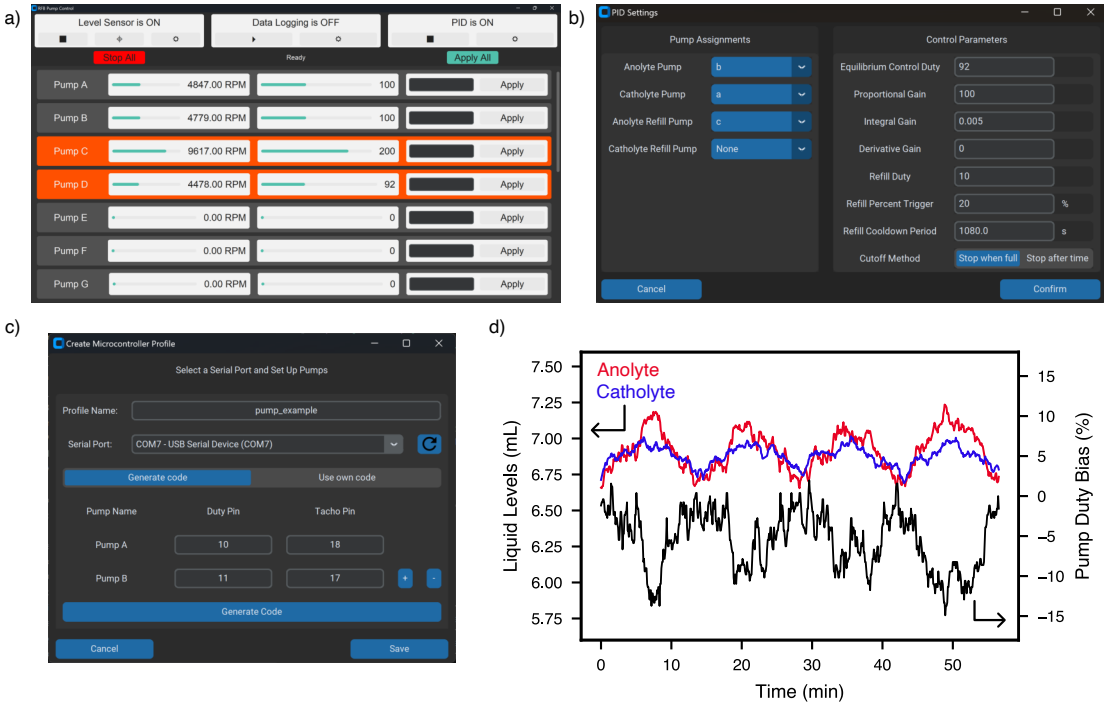

Figure 3.4: (a) Microcontroller setup page, showing the pin assignment process and code generation option.(b) User-configurable settings for the PID/refill control scheme. Similar options exist for other areas of the program. (c) Pump control page. The orange-highlighted pumps are actuated by the controller, while pumps A and B have had manual duties applied. The status of the volume sensor, controller, and data logger are also displayed.

Fig. 3.4(a) displays the program's main interface, where the level sensor and PID controller can be activated alongside a suite of user-configurable settings, some of which are shown in Fig. 3.4(b). Notably, the software includes a solvent refill control scheme that monitors total electrolyte volume and replenishes the reservoirs when levels fall below a set threshold. Additionally, a built-in data logger records electrolyte volumes, pump duty cycles, and periodic reservoir images. With an appropriate fluid delivery setup, the program effectively mitigates both electrolyte imbalance and loss, significantly extending cell lifespan.

While the LinkNet segmentation pipeline achieved 99.54% accuracy and a Dice coefficient of 97.49% on unseen test data, these results may not be immediately replicable in other lab setups, as the model was trained exclusively on images from our specific experimental layout. To address this, a non-parametric adaptive thresholding pipeline is included as a fallback volume detector. Additionally, the

data logger plays a crucial role in bridging this gap – by continuously recording images during experiments, it passively builds a large training dataset. Retraining the LinkNet model on these images allows it to adapt to the user's reservoir setup, ultimately recovering the performance observed in our experiments.

With appropriate parameter tuning and level detection, electrolyte imbalance was limited to 0.25 mL. Figure 3.4(d) plots typical liquid levels and pump duty biases during cycling experiments, revealing a periodic fluctuation in liquid levels that aligns with the charge-discharge cycle duration (∼15 min). As the battery charges and discharges, the electrolyte composition changes, requiring the pumps to dynamically adjust their duty cycles to maintain balance. This periodic trend highlights both the necessity and effectiveness of an active level-balancing system for long-duration testing.

3.3.3 Flow field exploration

Flow field design in RFBs is a more extensively studied topic compared to membrane fouling in nonaqueous electrolytes. Houser et al. investigated the impact of different flow field architectures through both mathematical modeling and experimental validation [88]. Their study included two channel-less flow field designs similar to those used in this work: one with an equal aspect ratio (EPL) and another with a short but wide path between the inlet and outlet (large aspect ratio). They found that cells with larger aspect ratios exhibited lower pressure drops across the cell, leading to higher net energy efficiencies. Building upon this work, this section examines how different flow configurations (co-current vs. counter-current) and flow rates influence cells with varying aspect ratios.

For this study, a modified cell design was employed to accommodate a broader range of flow field geometries. The expanded cell dimensions are provided in Appendix 3.A.2. To systematically assess performance differences, two extreme aspect ratios were selected. The small aspect ratio (1:3) directed the bulk of the electrolyte parallel to the cell length, while the large aspect ratio (3:1) oriented the bulk of the electrolyte perpendicular to the cell length. These configurations

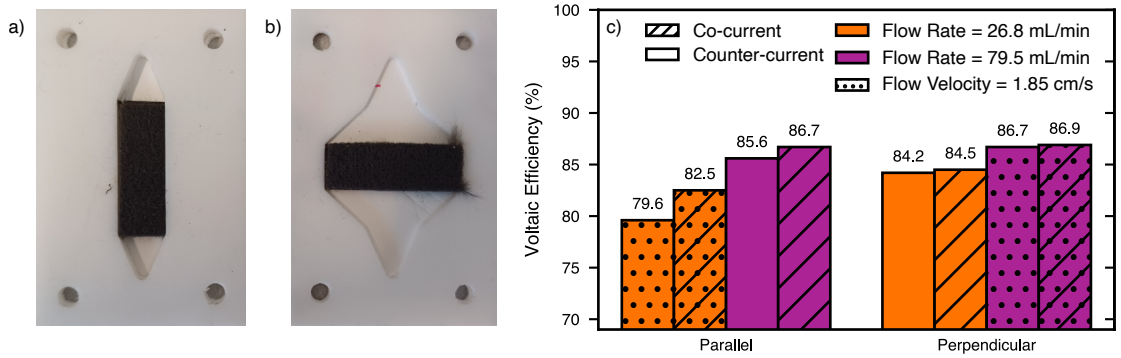

Figure 3.5: Pictures of the (a) parallel and (b) perpendicular flow field configurations. (c) Voltaic efficiencies for both flow fields under various flow configurations, volumetric flow rates, and mean linear flow velocities. Each data point is collected during cycling of the 0.1 M $V(acac)_3$, 0.3 M $TEABF_4$ nonaqueous electrolyte to 20% SOC at 20 mA cm^{-2}.

are henceforth referred to as the parallel and perpendicular flow fields, respectively. Fig. 3.5(a,b) displays images of the porous electrode integrated into the flow plate for each configuration.

The objective was to determine the effects of counter-current versus co-current operation on voltaic efficiency under two different conditions: (1) at the same mean linear flow velocity and (2) at the same volumetric flow rate. Both conditions were tested for the parallel and perpendicular flow fields to evaluate their impact on cell performance.

Under identical mean linear flow velocities, the pore Reynolds number—and consequently, the boundary layer characteristics—should be comparable between the parallel and perpendicular flow fields. The resulting voltaic efficiencies for these conditions are plotted with black dots in Fig. 3.5(c). In the parallel flow field, the co-current configuration led to an approximate 3% increase in voltaic efficiency. However, in the perpendicular flow field, the increase in voltaic efficiency was negligible. This result is likely due to the significantly shorter residence time in the perpendicular configuration, which limits the extent to which flow-related effects can manifest. Since differences between flow configurations arise along the direction of electrolyte flow, the reduced flow path in the perpendicular cell minimizes these effects.

Additionally, the perpendicular cell exhibited a ∼6% and ∼4% increase in efficiency under counter-current and co-current operation, respectively, compared to the parallel flow field. This trend aligns with expectations: due to the shorter residence time in the perpendicular configuration, a smaller fraction of the electrolyte undergoes reaction per pass, given that current densities remain constant. As a result, in the parallel flow field, lower concentrations of unreacted active species accumulate toward the reactor's outlet, leading to increased overpotentials required to sustain the reaction. This translates to a lower mean cell voltage, as measured by the potentiostat.

Initially, volumetric flow rates were adjusted between cells to match flow velocities, ensuring that boundary layers and residence times remained consistent. While useful, focusing solely on flow velocities can be misleading, as different velocities result in significantly different pressure losses across the cell. Assuming the pressure drop across the electrode follows Darcy's law, it can be reasonably inferred that pressure drops are equivalent in the case of similar volumetric flow rates. To investigate these effects, two volumetric flow rates – 26.8 mL/min and 79.5 mL/min (depicted in orange and purple in Fig. 3.5(c)) – were tested. At both flow rates, the perpendicular flow field outperformed the parallel configuration. Given that residence times were identical, this suggests that the perpendicular cell enhances mass transfer by facilitating the transport of unreacted active species. Thus, the perpendicular flow field presents a dual advantage: it reduces pumping energy requirements while simultaneously improving voltaic efficiency.

For the perpendicular flow field, co-current and counter-current operation resulted in negligible differences in efficiency, likely due to the short residence time of the active species, as discussed earlier. In contrast, within the parallel flow field, co-current operation provided a notable improvement in voltaic efficiency compared to counter-current flow. This efficiency difference was more pronounced at the lower flow rate. Despite identical residence times in the parallel cells at 26.8 mL/min, the co-current configuration outperformed the counter-current setup by ∼3%. These findings indicate that larger aspect ratios (i.e., perpendicular flow

fields) and co-current operation are generally preferable. However, with respect to volumetric flow rate, there exists a tradeoff between voltaic efficiency and pumping losses, which can be optimized based on specific application requirements.

3.4 Conclusions

This chapter systematically investigates the role of membrane stability, concentration gradients, and flow field design in the long-term performance of nonaqueous redox flow batteries. The use of stable vanadium acetylacetonate ($V(acac)_3$) chemistry enables isolation of membrane fouling degradation mechanisms, while revealing key approaches to minimize performance losses. The results demonstrate that concentration gradients across porous membranes significantly impact fouling and capacity retention. Switching from counter-current to co-current flow reduced membrane fouling rates by a factor of two. Additionally, implementing an active reservoir balancing system effectively eliminated membrane fouling at lower current densities and maintained stable cycling performance over multi-week experiments. Capacity fade remained time-independent, with minimal losses of 0.0011% and 0.0012% per full charge-discharge cycle at 20 mA cm^{-2} and 40 mA cm^{-2}, respectively. Furthermore, cyclic voltammetry confirmed negligible electrolyte degradation, reinforcing the stability of the $V(acac)_3$ system.

Beyond membrane performance, this chapter explored the impact of flow field design on voltaic efficiency. The results show that larger aspect ratio flow fields enhance mass transport, leading to a $\sim$5% increase in voltaic efficiency while simultaneously reducing pumping energy demands. Co-current operation consistently improved cell performance, particularly at lower flow rates, where mass transfer limitations are more pronounced. Finally, the inherent tradeoff between voltaic efficiency and volumetric flow rate are highlighted, emphasizing the need for application-specific optimization in RFB system design.

It is important to note that the experiments in this chapter primarily employ flow-through flow fields, whereas most commercial redox-flow batteries utilize flow-by or interdigitated configurations. This choice reflects practical constraints

at the academic scale, where implementing leak-tight and mechanically robust flow-by architectures in small-format cells is challenging. As a consequence, the hydrodynamic environment explored here differs from that of commercial systems, particularly with respect to per-pass utilization and electrolyte residence time. In the present work, per-pass conversions are intentionally kept low (around 1%) to minimize concentration gradients and isolate membrane fouling phenomena. In contrast, commercial VRFBs are generally designed to operate at higher per-pass utilizations and lower flow rates normalized by electrode area, although detailed industrial values are not publicly disclosed. These differences complicate direct quantitative extrapolation of the results reported here. Nevertheless, the qualitative trends observed – namely the sensitivity of membrane fouling and cell performance to concentration gradients imposed by flow configuration – are expected to remain relevant across scales. In particular, the results underscore that flow-field design and electrolyte management play a central role in controlling separator exposure to non-uniform reactant concentrations, irrespective of whether flow-through or flow-by architectures are employed.

These findings offer valuable insights for both assessing new nonaqueous RFB chemistries and optimizing existing systems. By providing practical strategies for isolating and mitigating membrane degradation while improving overall system efficiency, this work establishes a framework for more reliable long-term cycling. Additionally, the development of a user-friendly reservoir balancing application facilitates broader adoption of these improvements within the RFB research community. Future work should extend these findings on porous separators to ion exchange membranes, further exploring their limitations and potential mitigation strategies in similar nonaqueous electrolytes.

3.A Appendices

3.A.1 Cell 1 reactor schematics

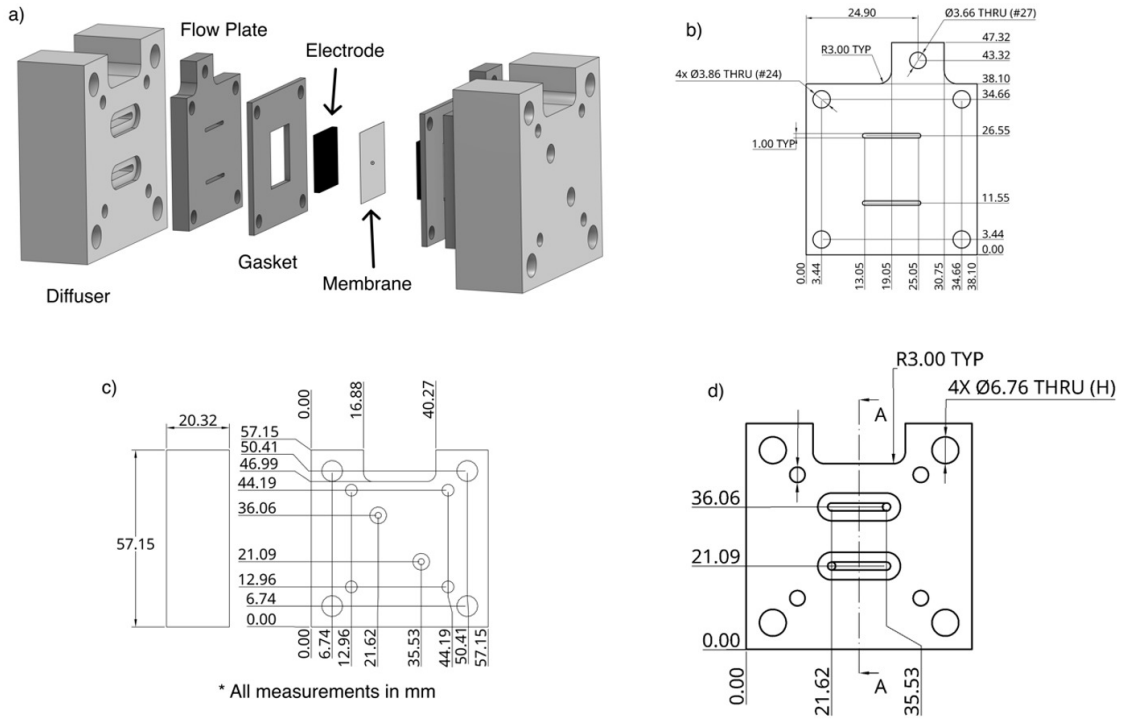

Figure 3.6: (a) Schematic for the Cell 1 flow cell reactor, (b) flow plate, and (c-d) diffuser plate. All measurements are reported in millimetres. The exposed membrane and electrode area has height of 1.64 cm (parallel to flow) and a width of 1.34 cm, resulting in a cross-sectional area of 2.20 cm^2. The compressed width and porosity of the electrode is 1.6 mm and 80% respectively. Thus, the open cell area normal to flow is 0.17 cm^2. Flow rates are reported as mean linear flow rates across the separator. With this reactor geometry, a 1.0 cm/s, 2.5 cm/s, and 5.0 cm/s linear flow rate corresponds to 10 mL/min, 26 mL/min, and 51 mL/min respectively.

3.A.2 Cell 2 reactor schematics

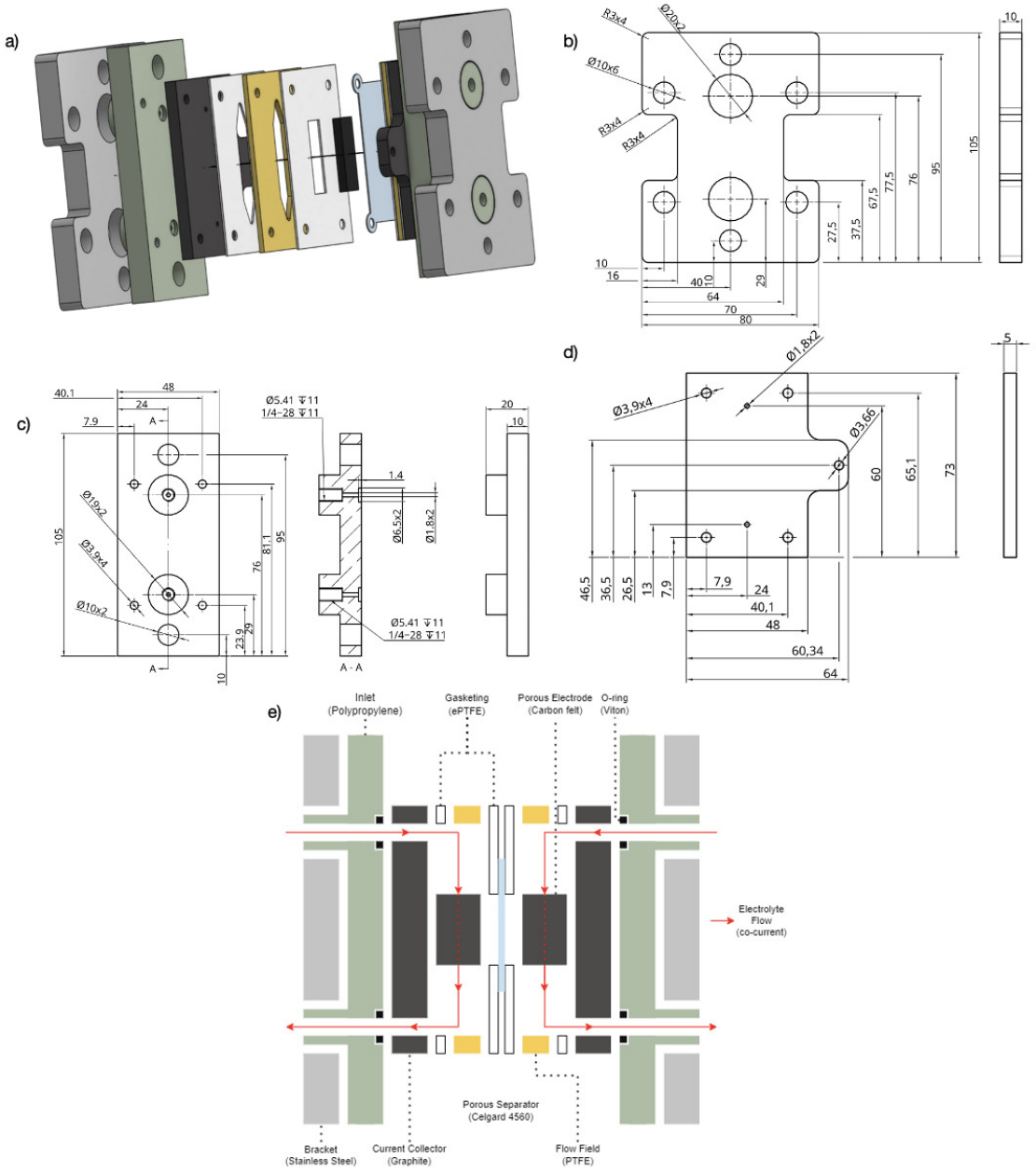

Figure 3.7: (a) Exploded view of the Cell 2 flow cell reactor, alongside schematics for (b) stainless steel outer bracket, (c) polypropylene fluid inlet and (d) graphite current collector. (e) 2D cutout of the design, showing the path of electrolyte through the reactor under co-current operation. Colours and positions of each part correspond to those in (a). The PTFE flow field and surrounding gasketing are laser cut and swapped in to achieve the different flow shapes. Six M8 bolts under 45 in-lb of torque are used to keep the cell under compression, which holds the reactor at 3.0 mm thickness, and a volume of 0.9 cm^3.

3.A.3 Cycling data for co- vs. counter-current flow configuration

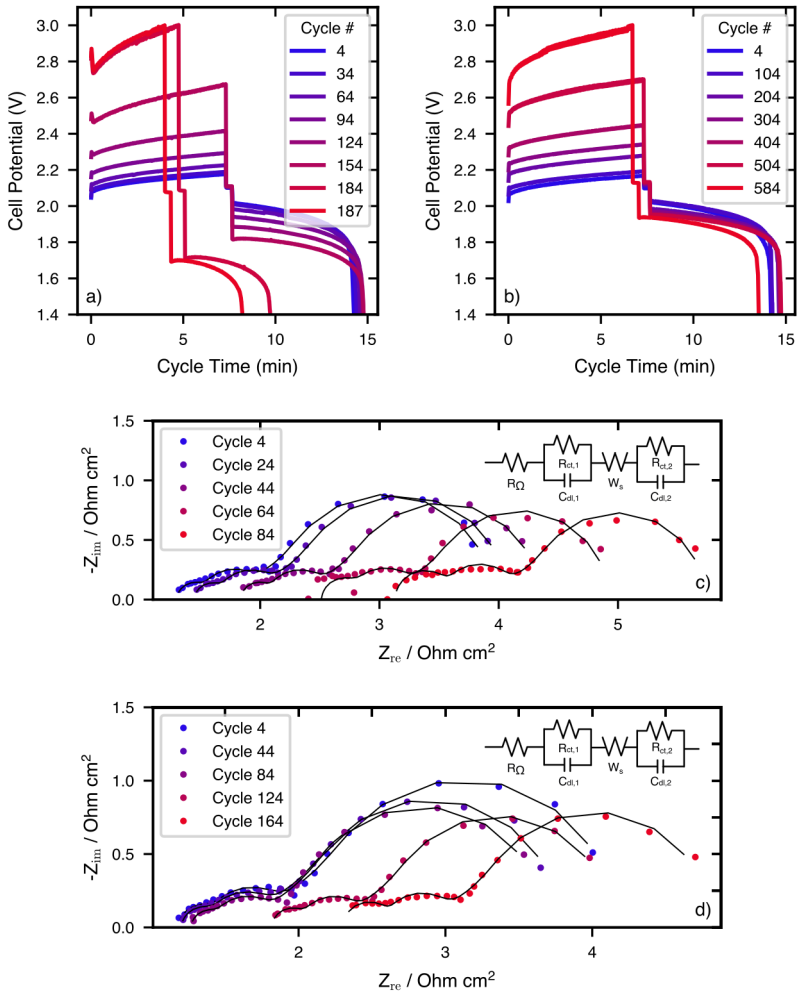

Figure 3.8: Representative voltage (a-b) and impedance (c-d) data for the (a,c) counter-current and (b,d) co-current cell without PID control. The black lines in the Nyquist plots are fits from the equivalent circuit model. Both cells were run with identical cycling conditions.

3.A.4 Improvements to level detection filter

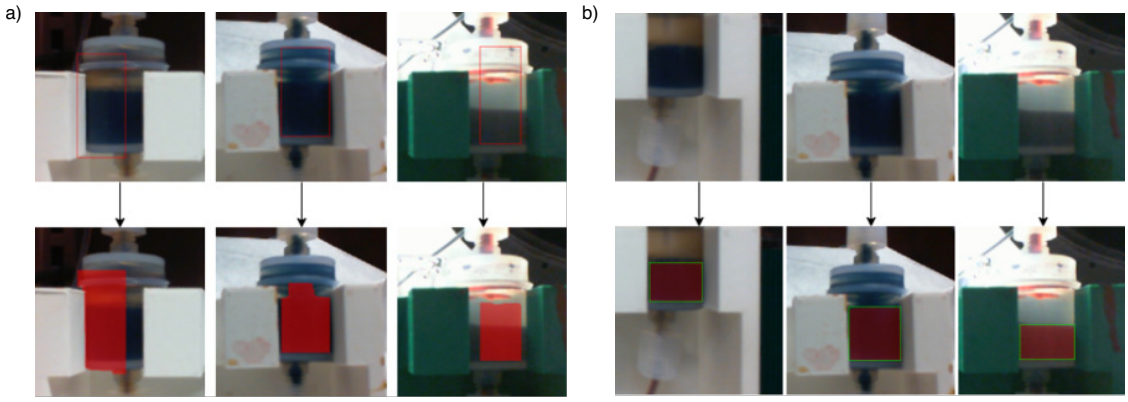

Figure 3.9: (a) Inaccurate filter detection under common perturbations, including camera movement, a thin film of electrolyte on the tank wall, and varying background lighting. (b) Improved level detection method demonstrating robustness against the same perturbations.

3.A.5 Galvanostatic cycling data for co-current cell with PID control

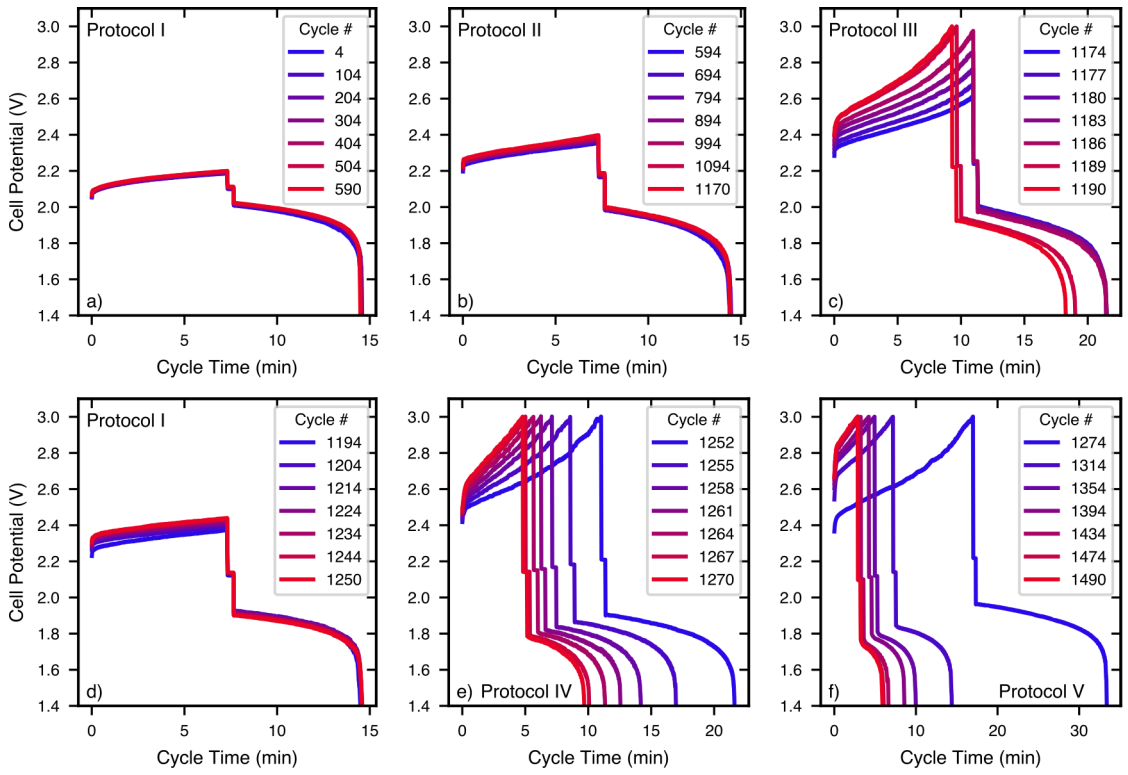

Figure 3.10: Representative voltage data for each protocol of the co-current cell with PID control and solvent refill.

3.A.6 Impedance data for co-current cell with PID control

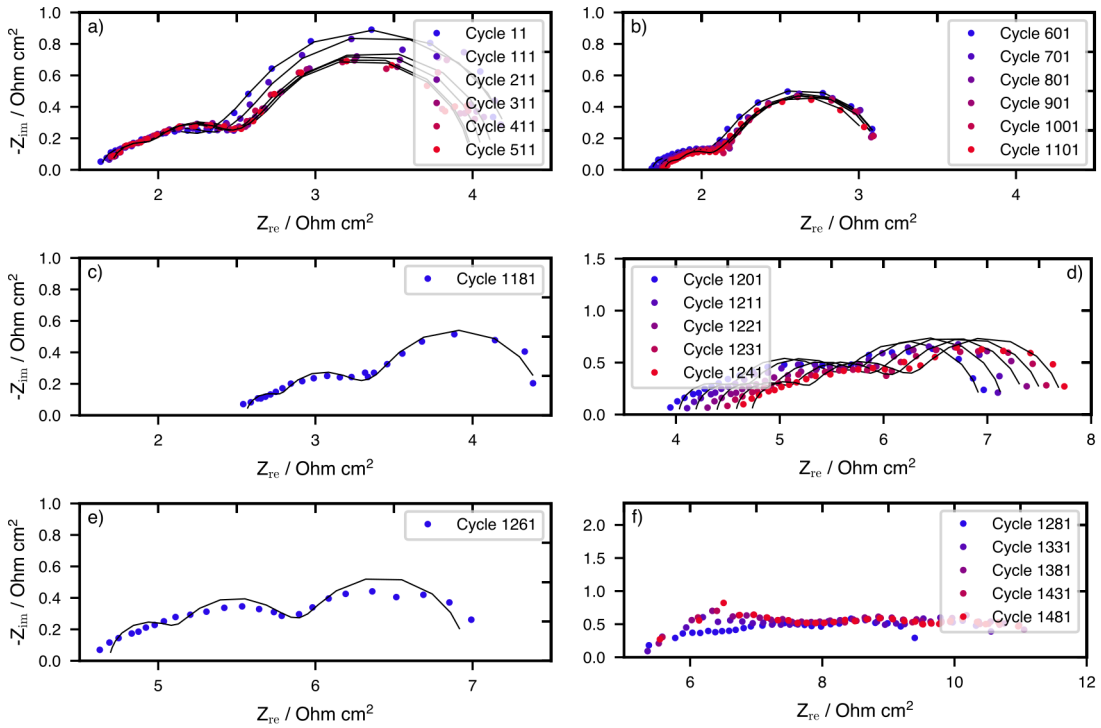

Figure 3.11: Impedance fits for the co-current cell with the active level-balancing controller during each protocol.

4

Deconstructing the Onsager-Stefan-Maxwell Framework

Contents

4.1 Introduction

Accurate modeling of ionic transport in concentrated electrolyte solutions requires accounting for complex interactions among ions and solvent molecules, as these interactions significantly influence electrolyte behavior and performance in electrochemical devices [89, 90]. Classical dilute-solution transport models, such as the Nernst–Planck theory, fail to describe ion transport accurately at high concentrations due to oversimplified assumptions about ion–ion and ion–solvent interactions [58, 91]. To overcome these limitations, the Onsager–Stefan–Maxwell (OSM) framework is utilized, providing a rigorous foundation for modeling mass transport in concentrated electrolyte solutions. This chapter does not revisit the established value of OSM theory itself, but introduces a salt–charge reformulation designed to independently assess the role of electroneutrality, thermodynamic factors, and model reduction in transport problems relevant to redox flow batteries.

The OSM framework originates from the principles established by Maxwell and Stefan, who first described multicomponent diffusive fluxes based on relative motion between species driven by chemical potential gradients [62, 92–94]. Onsager later introduced a theoretical underpinning by connecting irreversible thermodynamics to more general flux-force relationships [95, 96]. The OSM transport equations explicitly account for interactions between multiple species, enabling the accurate description of electrolyte behavior even at high ionic strengths where electrostatic and steric interactions between solute species become substantial.

For electrolytic solutions with n species in an isothermal, isotropic, isobaric phase, the Onsager–Stephan–Maxwell equations relate the gradient in electrochemical potentials as

$$-\nabla\mu_i = \sum_{j=1}^{n} M_{ij}\vec{N}_j, \tag{4.1}$$

where μ_i signifies the electrochemical potential of species i and $\vec{N}_j$, its total molar flux. The Stefan–Maxwell transport coefficients, M_{ij}, make up an $n \times n$ matrix

M whose entries are

$$M_{ij} = \begin{cases} -\dfrac{RT}{c_{\mathrm{T}}\mathscr{D}_{ij}} & \text{if} \quad i \neq j \\ \dfrac{RT}{c_{\mathrm{T}}} \displaystyle\sum_{k \neq i}^{n} \dfrac{c_k}{\mathscr{D}_{ik} c_j} & \text{if} \quad i = j, \end{cases} \tag{4.2}$$

in which R represents the gas constant, T, the absolute temperature, c_{T}, the total species molarity, c_i, the molarity of species i, and $\mathscr{D}_{ij}$, the Stefan–Maxwell diffusivity of species i through species j. This structure is derived by using principles of irreversible thermodynamics to formulate a general force-explicit transport equation explicit in chemical-potential gradients, and then comparing its transport matrix to the matrix of Stefan–Maxwell parameters.

Despite its accuracy, the OSM framework is usually not employed when modeling redox flow batteries (RFBs) due to practical constraints [97]. A significant barrier to widespread adoption is the substantial experimental and computational effort required to quantify numerous material parameters, including diffusivities and thermodynamic factors [98]. The complexity and experimental burden involved in accurately determining these parameters often lead researchers to adopt simpler, albeit less accurate, transport models.

Nonetheless, employing the OSM framework for RFBs is particularly crucial. RFB electrolytes frequently operate under concentrated conditions to achieve desirable energy densities, resulting in strong interactions among ionic species. Ignoring these interactions can lead to substantial inaccuracies when predicting battery performance metrics, including cell resistance, concentration polarization, and reaction kinetics at electrodes [99, 100]. The OSM approach thus becomes essential for accurately capturing nuanced transport phenomena within concentrated electrolytes, guiding optimization and technological improvements by providing realistic performance predictions.

As demonstrated in Chapters 2 and 3, concentration-driven inefficiencies can significantly impact the performance of redox flow batteries (RFBs). Accurate modeling using the Onsager–Stefan–Maxwell (OSM) framework enables a more rigorous description of the transport phenomena in the concentrated electrolytes commonly

employed in RFB systems. This chapter adopts a salt–charge basis to independently evaluate the validity of three frequently invoked assumptions in electrolyte modeling within the OSM framework: (1) electroneutrality, (2) thermodynamic ideality, and (3) negligible ion–ion friction (drag). Subsequently, several reduced submodels are introduced, culminating in an example that demonstrates how these assumptions can simplify the OSM equations into the more familiar Nernst–Planck formulation.

4.2 State variables in the salt–charge basis

This section introduces all the state variables required to derive the dynamics of isothermal, isobaric, stagnant electrolytic solutions through the Onsager–Stefan–Maxwell framework [96], and provides transformations to and from a salt–charge basis of the type proposed by Van-Brunt et al. [64]. Matrix notation will be used to simplify expressions and enhance the clarity of equations describing multispecies transport. By organizing state variables into column vectors – where each entry corresponds to a different species – we can represent full sets of species-specific equations compactly as single matrix equations. This transformation is not merely a change of variables, but provides a structured separation between charge-driven and mass-driven transport processes that is not explicit in standard species-based OSM formulations. The theory and new relationships provided here largely build upon prior works by Monroe et al. and Van-Brunt et al. [64, 101].

4.2.1 Chemical potentials

Transport models are fundamentally grounded in principles from equilibrium thermodynamics. In particular, chemical thermodynamics is based on the principle that the molar free energy of a mixture is distributed among its components in proportion to their molar quantities, with each species' contribution weighted by its chemical potential [102, 103]. At thermodynamic equilibrium, all species-specific bulk properties are determined by these chemical potentials. In the context of transport theory, chemical potentials are especially important, as gradients

in chemical potential between adjacent open systems serve as the driving force for material exchange.

A set of hypothetical simple association equilibria can be written to identify components within a mixture of charged species. For example, the equilibrium reaction of a binary salt that dissociates into species S_i and S_j with charges of z_i and z_j respectively can be written as

$$\nu_i \mathrm{S}_i^{z_i} + \nu_j \mathrm{S}_j^{z_j} \rightleftharpoons (\mathrm{S}_i)_{\nu_i} (\mathrm{S}_j)_{\nu_j}, \tag{4.3}$$

where the stoichiometric proportions of ν_i and ν_j must satisfy the Guggenheim condition such that $\nu_i z_i + \nu_j z_j = 0$, with ν_i and ν_j coprime whole numbers [104]. Throughout this chapter, I refer to the products of such association equilibria as *components* and the reactants as *species*. Note that the components, which are neutral by definition, have a measurable chemical potential which is the sum of its species chemical potentials μ_i such that

$$\nu_i \mu_{\mathrm{S}_i} + \nu_j \mu_{\mathrm{S}_j} = \mu_{(\mathrm{S}_i)_{\nu_i} (\mathrm{S}_j)_{\nu_j}}. \tag{4.4}$$

In the case of an uncharged uni-molecular species, S_i would just be in equilibrium with itself: whenever $z_i = 0$, $\nu_i = 1$ and $\nu_j = 0$.

Van-Brunt et al. introduced the idea of a *salt–charge basis* [64], an algebraic structure that systematically orders the n (generally charged) species in an electrolytic system and maps them into a set comprising $n-1$ (uncharged) components and the excess charge density. Every possible neutral component can be formed using recombination reactions involving $n-1$ association products, resulting in only $n-1$ independent simple association equilibria. For each simple association equilibrium k, let $\boldsymbol{\nu}_k$ be a n-dimensional column matrix whose ith entry is the stoichiometric coefficient of species i in reaction k. Additionally, define $\mathbf{z}$ as a n-dimensional column matrix whose ith entry is the equivalent charge of species i. From Eq. 4.3, we know that for every equilibrium reaction k, $\boldsymbol{\nu}_k^\top \mathbf{z} = 0$. This feature of Guggenheim's condition results in the orthogonality of each set of reaction-reactant stoichiometries $\boldsymbol{\nu}_k$ to the list of species charges $\mathbf{z}$. These two column vectors allow one to form

a measurable component chemical potential from species chemical potentials in a general and thermodynamically rigorous manner.

By construction, the combined column matrices of $\boldsymbol{\nu}_i$ and $\mathbf{z}$ are linearly independent; thus, the n-tuple $\{\boldsymbol{\nu}_1, \ldots, \boldsymbol{\nu}_{n-1}, \mathbf{z}\}$ form a basis for the entire composition space. By convention, the species in a salt–charge basis are ordered with n_0 uncharged species first and n_c charged species after ($n = n_0 + n_c$), such that species n and $n-1$ are stipulated to have opposed charges. This forms $\mathbf{z}$ where the first n_0 entries equal zero and its last n_c entries are nonzero, with $z_n/z_{n-1} < 0$. The choices making up the salt–charge basis are summarized by an invertible matrix $\mathbf{Z}$,

$$\mathbf{Z} = \begin{bmatrix} \boldsymbol{\nu}_1^\top \\ \vdots \\ \boldsymbol{\nu}_{n-1}^\top \\ \mathbf{z}^\top / \|\mathbf{z}\| \end{bmatrix} = \begin{bmatrix} \mathbf{N}^\top \\ \hat{\mathbf{z}}^\top \end{bmatrix} \tag{4.5}$$

where the superscript $\top$ indicates the matrix transpose, $\|\mathbf{z}\| = \sqrt{\mathbf{z}^\top \mathbf{z}}$, and $\mathbf{N}^\top$ is an $n \times (n-1)$ matrix whose ith column is $\boldsymbol{\nu}_i$. By design, $\mathbf{N}$ has a block structure

$$\mathbf{N} = \begin{bmatrix} \boldsymbol{\nu}_1 & \cdots & \boldsymbol{\nu}_{n-1} \end{bmatrix} = \begin{bmatrix} \mathbf{I}_{n_0} & \mathbf{O}_{n_0 \times (n_c-1)} \\ \mathbf{O}_{n_c \times n_0} & \mathbf{A} \end{bmatrix} \tag{4.6}$$

where $\mathbf{O}_{i,j}$ is a $i \times j$ matrix of zeros, $\mathbf{I}_{n_0}$ is the $n_0 \times n_0$ identity matrix and $\mathbf{A}$ is a $n_c \times (n_c - 1)$ matrix of rank $n_c - 1$. A concrete example of establishing a salt–charge basis for a 2 solvent, 4 ion electrolyte is demonstrated in Appendix 4.A.1.

The invertible transformation matrix $\mathbf{Z}$ can be used to convert the electrochemical potential of each species to their respective components through

$$\boldsymbol{\mu}_Z = \mathbf{Z}\boldsymbol{\mu} = \begin{bmatrix} \boldsymbol{\mu}_\nu \\ \mu_z \end{bmatrix}, \tag{4.7}$$

where $\mu_z = F\|\mathbf{z}\|\,\Phi_z$. The $(n-1)$-dimensional column matrix, $\boldsymbol{\mu}_\nu$, lists the component chemical potentials in order of the corresponding association equilibria. The last element of $\boldsymbol{\mu}_Z$ is the non-neutral free-energy contribution that involves the salt–charge potential Φ_z which is related to the solution potential Φ through Guggenheim's species activities by

$$\mu_z = \frac{RT}{\|\mathbf{z}\|} \sum_{i=1}^{n} z_i \ln a_i + F\|\mathbf{z}\|\,\Phi, \tag{4.8}$$

in which R is the gas constant, T is the absolute temperature, F is Faraday's constant and a_i represents the chemical activity of species i. Although the chemical and electrical contributions of both the solution and salt–charge potentials are indistinguishable, one can still understand the salt–charge potential Φ_z as a type of electrical potential with units of volts. As we shall see later, the Nernst–Planck potential and salt–charge potential identify with each other in a thermodynamically ideal ($a_i = 1$) solution. Van-Brunt et al. have shown how to relate the salt–charge potential to the potential measured by a given reference electrode [64].

The inverse of the transformation matrix is used to convert the component chemical potentials back into species chemical potentials as $\boldsymbol{\mu} = \mathbf{Z}^{-1}\boldsymbol{\mu}_Z$. In doing so it is worth noting that $\mathbf{Z}^{-1}$ can be written in block form determined entirely by the matrices $\mathbf{N}$ and $\hat{\mathbf{z}}$:

$$\mathbf{Z}^{-1} = \begin{bmatrix} \boldsymbol{\aleph} & \hat{\mathbf{z}}, \end{bmatrix}, \qquad \text{where} \qquad \boldsymbol{\aleph} = \mathbf{N}(\mathbf{N}^\top\mathbf{N})^{-1}; \tag{4.9}$$

the matrix $\boldsymbol{\aleph}$ is a $n \times (n-1)$ matrix whose block form is

$$\boldsymbol{\aleph} = \begin{bmatrix} \mathbf{I}_{n_0} & \mathbf{O}_{n_0\times(n_c-1)} \\ \mathbf{O}_{n_c\times n_0} & \mathbf{B} \end{bmatrix}, \tag{4.10}$$

where $\mathbf{B}$ is a $n_c \times (n_c - 1)$ submatrix. Note that the left inverse $\boldsymbol{\aleph}$ is fully defined by $\mathbf{N}$ and has equal rank to it. This results in two convenient properties,

$$\mathbf{N}^\top\boldsymbol{\aleph} = \mathbf{I}_{n-1} \qquad \text{and} \qquad \mathbf{N}\boldsymbol{\aleph}^\top = \boldsymbol{\aleph}\mathbf{N}^\top = \mathbf{I}_n - \hat{\mathbf{z}}\hat{\mathbf{z}}^\top, \tag{4.11}$$

which are derived from Eqs. 4.6 and 4.10 (see Appendices 4.A.2 and 4.A.3) and will prove useful later.

4.2.2 Extensive variables

Continuum transport models are generally formulated as systems of partial differential equations defined within a fixed, inertial reference frame. These equations describe how various physical quantities – such as scalar, vector, or tensor fields that represent the local state of a material – change over time within infinitesimal control volumes centered at specific points in space. According to the framework

of irreversible thermodynamics, all these neighboring control volumes are treated as open subsystems within the broader material system. In the case of a multicomponent mixture, the state at any point is typically characterized by the local temperature T, pressure p, and the molar concentrations c_i of each species (with $i = 1$ to n). Additionally, each species has an associated molar flux vector $\vec{N}_i$, which represents its net transport across the control volume's boundary. Depending on the context, these models may also include a heat flux vector [105], as well as traceless tensors that represent mechanical effects like strain, deformation rate, and deviatoric stress [106–108].

The instantaneous state of species composition within a control volume containing n species is quantified by the n-entry column matrix $\mathbf{c}$, whose ith entry is the scalar molar species concentration c_i; the dynamical state is quantified by the n-entry column matrix $\vec{\mathbf{n}}$, whose ith entry is the species flux vector $\vec{N}_i$. All n species continuity equations can thus be captured by the matrix equation

$$\frac{\partial \mathbf{c}}{\partial t} = -\vec{\nabla} \cdot \vec{\mathbf{n}} + \mathbf{r}, \tag{4.12}$$

where $\mathbf{r}$ is a column matrix whose ith entry quantifies the volumetric generation rate of species i. Here $\partial \mathbf{c}/\partial t$ and $\vec{\nabla} \cdot \vec{\mathbf{n}}$ respectively represent columns whose ith entries are $\partial c_i/\partial t$ and $\vec{\nabla} \cdot \vec{N}_i$.

Faraday's law for charge relates the local excess charge density ρ_e within a material to its species concentrations through

$$\rho_e = F\mathbf{z}^\top \mathbf{c}, \tag{4.13}$$

where F is Faraday's constant. Similarly, the current density $\vec{i}$ relates to the species fluxes through

$$\vec{i} = F\mathbf{z}^\top \vec{\mathbf{n}}, \tag{4.14}$$

which is Faraday's law for current. Homogeneous electrochemical reactions balance charge as well as mass, so $\mathbf{z}^\top \mathbf{r} = 0$ when all species within a mass-transport system are constrained to a single phase.

Goyal and Monroe discussed how mass conservation and Eq. 4.12 imply the familiar mass continuity relation from fluid mechanics,

$$\frac{\partial \rho}{\partial t} = -\vec{\nabla} \cdot (\rho \vec{v}) \,, \tag{4.15}$$

if a mixture's density ρ and mass-average flow velocity $\vec{v}$ are consistently defined through the molar masses of each species [107]. They also showed that charge conservation and Eq. 4.12 imply the same charge continuity equation which derives from Maxwell's equations,

$$\frac{\partial \rho_e}{\partial t} = -\vec{\nabla} \cdot \vec{i}, \tag{4.16}$$

if ρ_e and $\vec{i}$ are consistently defined through $\mathbf{z}$.

As we proceed, equation 4.12 alone suffices to express material continuity. It is important to note, however, that Eq. 4.12 implies the mass-continuity condition 4.15, while definitions 4.13 and 4.14 imply the charge-continuity condition 4.16. The interdependence among species, mass, and charge continuity equations can sometimes be leveraged to simplify transport analysis. For instance, Newman applied continuity equations for salt concentration and charge density instead of cation and anion concentrations to analyze transport near a rotating disk electrode [109]. Doyle et al. utilized charge continuity instead of an anion balance in their lithium-ion battery model [90]. Newman and Chapman employed molar-volume continuity, charge continuity, and salt continuity instead of species balances when examining restricted diffusion in a binary electrolytic solution [110], a method also employed by Liu and Monroe in their study of solute-volume effects [106].

It is sometimes convenient to consider the total molar mass of a mixture $\overline{m}$. Let the total species molarity c_{T} be defined as

$$c_{\mathrm{T}} = \sum_{i=1}^{n} c_i = \mathbf{1}^{\top} \mathbf{c}, \tag{4.17}$$

in which $\mathbf{1}$ is a column vector whose entries are all '1'. Then $\overline{m}$ is defined by the mixture's density ρ through $\overline{m} = \rho / c_{\mathrm{T}}$.

The transformation matrix $\mathbf{Z}$ can be used to convert a set of species concentrations and fluxes to the salt–charge basis such that

$$\mathbf{c}_Z = \mathbf{Z}^{-\top}\mathbf{c} = \begin{bmatrix} \mathbf{c}_\nu \\ \frac{\rho_e}{F\|\mathbf{z}\|} \end{bmatrix} \quad \text{and} \quad \vec{\mathbf{n}}_Z = \mathbf{Z}^{-\top}\vec{\mathbf{n}} = \begin{bmatrix} \vec{\mathbf{n}}_\nu \\ \frac{\vec{i}}{F\|\mathbf{z}\|} \end{bmatrix} \tag{4.18}$$

where the superscript $-\top$ represents the inverse transpose. Similar to the component chemical potentials, $\mathbf{c}_\nu$ and $\vec{\mathbf{n}}_\nu$ are $(n-1)$-dimensional column vectors consisting of the component concentrations and fluxes, respectively. The last entry of $\mathbf{c}_Z$ expresses the excess charge in molar units, while the last entry of $\vec{\mathbf{n}}_Z$ represent the normalized current density. The last entry of $\mathbf{c}_Z$ is nonzero under the assumption of electroneutrality, but the last entry of $\vec{\mathbf{n}}_Z$ is not.

Alternatively, one can left-multiply Eq. 4.18 by $\mathbf{Z}^\top$ to show that the decompositions

$$\mathbf{c} = \mathbf{N}\mathbf{c}_\nu + \frac{\hat{\mathbf{z}}}{F\|\mathbf{z}\|}\rho_e \quad \text{and} \quad \vec{\mathbf{n}} = \mathbf{N}\vec{\mathbf{n}}_\nu + \frac{\hat{\mathbf{z}}}{F\|\mathbf{z}\|}\vec{i} \tag{4.19}$$

express the species $\mathbf{c}$ and $\vec{\mathbf{n}}$ in terms of the $n-1$ electroneutral components $\mathbf{c}_\nu$ and $\vec{\mathbf{n}}_\nu$ and the non-neutral charge variations or current densities associated with ρ_e and $\vec{i}$.

The fluxes $\vec{\mathbf{n}}$ can also be written in terms of excess fluxes $\vec{\mathbf{j}}^*$ relative to any convective velocity $\vec{v}^*$. Letting $\vec{\mathbf{n}} = \vec{\mathbf{j}}^* + \mathbf{c}\vec{v}^*$, Eq. 4.19 implies that

$$\vec{\mathbf{j}}^* = \mathbf{N}\vec{\mathbf{j}}_\nu^* + \frac{\hat{\mathbf{z}}}{F\|\mathbf{z}\|}\left(\vec{i} - \rho_e\vec{v}^*\right) \tag{4.20}$$

where $\vec{\mathbf{j}}_\nu^* = \vec{\mathbf{n}}_\nu - \mathbf{c}_\nu\vec{v}^*$ defines the set of excess component fluxes relative to $\vec{v}^*$. From this, it is clear that the excess current density from charge convection $\vec{i}^*$ is related to the total electrical current density such that $\vec{i} = \vec{i}^* + \rho_e\vec{v}^*$. When electroneutrality is assumed, $\vec{i} = \vec{i}^*$, independent of convection.

4.2.3 Intensive variables

Molar masses, which are independent of pressure p, temperature T, and species makeup $\mathbf{c}$, allow one to define the intensive property of mass density ρ of any n-ary mixture through the inner product

$$\rho = \sum_{i=1}^{n} \overline{m}_i c_i = \overline{\mathbf{m}}^\top \mathbf{c}, \tag{4.21}$$

in which $\overline{\mathbf{m}}$ is an n-dimensional column matrix consisting of the molar mass m_i of species i. Note that combining this with Eq. 4.17, allows one to define $\overline{m} = \rho/c_{\mathrm{T}}$ as the total molar mass. Despite its foundational role, the thermodynamics of material volume is seldom explicitly considered in transport analyses. In the context of convective diffusion within condensed phases, the standard assumption of incompressibility (constant ρ) is frequently adopted without question [111]. However, even under constant temperature and pressure, a material's mass density can exhibit significant dependence on local composition. For example, density measurements of non-aqueous battery electrolytes such as $LiPF_6$ in carbonate solvents demonstrate systematic, concentration-dependent variations, with reported density changes on the order of several percent over typical operating concentration ranges[112, 113]. These deviations imply that applying the incompressibility assumption to multispecies mass transport can overlook key effects that may be critical to accurately capturing system behavior [99].

Additionally, define the mass-average flow velocity $\vec{v}$ as

$$\vec{v} = \frac{1}{\rho}\sum_{i=1}^{n} \overline{m}_i \vec{N}_i = \frac{\overline{\mathbf{m}}^{\top}\vec{\mathbf{n}}}{\rho} \tag{4.22}$$

which will be used to separate $\vec{\mathbf{n}}$ into its convective and diffusive motions in section 4.3.1. Assuming the absence of nuclear reactions and sufficiently low $\vec{v}$ to neglect relativistic effects, the principle that chemical reactions conserve mass requires that $\overline{\mathbf{m}}^{\top}\mathbf{r} = 0$ locally within any single-phase material. In other words, element conservation in chemical reactions implies that the set of species generation rates is orthogonal to the species molar masses.

Instead of using molar concentrations, the following analysis adopts species mole fractions as the composition variables in the thermodynamic constitutive relations. As noted by Liu and Monroe [114], mole fractions offer several advantages: they directly reflect the relative counts of molecular entities, are dimensionless, remain invariant with respect to temperature and pressure, and are inherently bounded between 0 and 1. However, it is worth briefly noting a limitation of this approach. Mole-fraction-based composition can become problematic in mixtures with highly

disparate species molecular weights, particularly in systems containing long-chain or polydisperse polymers. To address such challenges, prior studies – including those by Pintauro and Bennion [115], Fuller and Newman [116], Fornasiero et al. [117], and Salehi et al. [118] – have treated representative repeat units, rather than entire polymer chains, as distinct species for defining concentrations and computing partial properties. It is important to recognize, however, that the transport models of most canonical theories describing polymer mixture thermodynamics employ volume fractions to characterize composition [119]. Accurately measuring or controlling the volumes occupied by condensed phases presents significant experimental challenges. In isobaric, isothermal systems composed of liquids or solids, the total molar volume can vary with local composition. While molar concentrations offer intuitive insight into particle motion and mass density aids in understanding momentum transport, it is important to recognize that the physical volumes underpinning both $\mathbf{c}$ and ρ may vary spatially in nonequilibrium systems.

Let the species mole fractions $\mathbf{y}$ and component mole fractions $\mathbf{y}_Z$ be defined as

$$\mathbf{y} = \frac{1}{c_\mathrm{T}}\mathbf{c} \quad \text{and} \quad \mathbf{y}_Z = \frac{1}{c_\mathrm{T}}\mathbf{c}_Z = \begin{bmatrix} \mathbf{y}_\nu \\ \frac{\rho_e}{Fc_\mathrm{T}\|\mathbf{z}\|} \end{bmatrix} \tag{4.23}$$

respectively. Note that the traditional properties of mole fractions restrict the sum of the elements within $\mathbf{y}$ and therefore $\mathbf{y}_Z$ through

$$1 = \mathbf{1}^\top \mathbf{y} = \boldsymbol{\nu}_Z^\top \mathbf{y}_Z, \tag{4.24}$$

wherein the stoichiometric correction

$$\boldsymbol{\nu}_Z = \mathbf{Z}\mathbf{1} = \begin{bmatrix} \boldsymbol{\nu}_\nu \\ \nu_z \end{bmatrix} \tag{4.25}$$

expresses the number of species contributed by each neutral component and the effect of excess-charge variation on total molar content.

The restriction imposed by the mole fraction sums makes one of the entries in $\mathbf{y}$ and $\mathbf{y}_Z$ redundant. For example, the mole fraction of species n is defined by $y_n = 1 - \sum_i^{n-1} y_i$. Thus, it is often convenient to work with the truncated set of species mole fractions $\mathbf{y}_{\neg n}$ which discards the nth entry of $\mathbf{y}$ into a $n-1$

column matrix consisting of independent mole fractions. Specifically, one can form this set by using the matrix product

$$\mathbf{y}_{\neg n} = \begin{bmatrix} \mathbf{I}_{\neg n,\neg n} & \mathbf{o}_{\neg n} \end{bmatrix} \mathbf{y}, \tag{4.26}$$

in which $\mathbf{v}_{\neg k}$ represents the submatrix formed by striking the kth row entry of column $\mathbf{v}$ and $\mathbf{A}_{\neg k,\neg l}$, the submatrix formed by striking the kth row and lth column of matrix $\mathbf{A}$ but leaving all its columns (or rows). For example, matrices $\mathbf{N}$ and $\aleph$ can be defined concisely as $\mathbf{N}^\top = \mathbf{Z}_{\neg n,0}$ and $\aleph = \left(\mathbf{Z}^{-1}\right)_{0,\neg n}$.

4.2.4 Volume equation of state

The total species molarity c_T used in defining $\mathbf{y}$ and $\mathbf{y}_Z$ is a function of temperature, pressure, and composition through thermodynamic properties. Define the partial molar volume $\overline{V}_i$ as the variation in volume V of a solution with changes in the molar composition at a given temperature and pressure. Alternatively, the Maxwell relations from classical thermodynamics show that the chemical potential of species i varies with pressure through

$$\overline{V}_i := \left(\frac{\partial V}{\partial n_i}\right)_{T,p,\mathbf{y}} = \left(\frac{\partial \mu_i}{\partial p}\right)_{T,p,\mathbf{y}}. \tag{4.27}$$

Experimental determination of partial molar volumes typically involves studying how mass density ρ changes with mixture composition [120]. Computational approaches have also been employed, with values extracted from molecular dynamics simulations by analyzing thermodynamic fluctuations [121]. Again, let $\overline{\mathbf{v}}$ be a n-dimensional column matrix whose ith entry is $\overline{V}_i$. Note that the extensivity of volume requires that $\mathbf{y}^\top \vec{\nabla} \overline{\mathbf{v}} = \vec{0}$ at a fixed T and p. Dividing the total differential of V at constant T and p by the summation of the total moles in the system shows that

$$\frac{1}{c_\mathrm{T}} = \sum_{i=1}^{n} \overline{V}_i y_i = \overline{\mathbf{v}}^\top \mathbf{y}. \tag{4.28}$$

It is clear that $c_\mathrm{T}(\mathbf{y})$, which in turn implies that the solution density $\rho = \overline{m} c_\mathrm{T}$ is a thermodynamic function of $\mathbf{y}$ only. Multiplication of the equation of state

by c_T, taking the gradient of both sides, applying the Gibbs–Duhem equation for volume [122], and replacing $\mathbf{y}$ with $\mathbf{c}/c_\mathrm{T}$ shows that

$$\overline{\mathbf{v}}^\top \vec{\nabla}\mathbf{c} = \vec{0} \tag{4.29}$$

at constant temperature and pressure. Thus, within a multi-species single phase under isothermal and isobaric conditions, one of the species molarities must depend on the others and the set of species-concentration gradients $\vec{\nabla}\mathbf{c}$ is orthogonal to $\overline{\mathbf{v}}$.

The gradient of Eq. 4.23 can be simplified with Eqs. 4.17 and 4.28 to define the relationship between the concentration and mole fraction gradients as

$$\vec{\nabla}\mathbf{c} = c_\mathrm{T}(\mathbf{y})\left(\mathbf{I} - c_\mathrm{T}(\mathbf{y})\mathbf{y}\overline{\mathbf{v}}^\top\right)\vec{\nabla}\mathbf{y} \tag{4.30}$$

and

$$\vec{\nabla}\mathbf{y} = \frac{1}{c_\mathrm{T}(\mathbf{c})}\left(\mathbf{I} - \frac{1}{c_\mathrm{T}(\mathbf{c})}\mathbf{c}\mathbf{1}^\top\right)\vec{\nabla}\mathbf{c}. \tag{4.31}$$

Recall, however, that there are only $n-1$ independent entries of $\mathbf{c}$ and $\mathbf{y}$ due to Gibbs phase rule (Eq. 4.28) and the mole fraction sum requirement (Eq. 4.24). Eliminating the redundant nth entry of $\mathbf{c}$ and $\mathbf{y}$ results in the following forms of the state equations:

$$c_\mathrm{T}(\mathbf{c}_{\neg n}) = \frac{1}{\overline{V}_n} - \frac{1}{\overline{V}_n}\left(\overline{\mathbf{v}}_{\neg n} - \overline{V}_n\mathbf{1}_{\neg n}\right)^\top \mathbf{c}_{\neg n} \tag{4.32}$$

or

$$\frac{1}{c_\mathrm{T}\left(\mathbf{y}_{\neg n}\right)} = \overline{V}_n + \left(\overline{\mathbf{v}}_{\neg n} - \overline{V}_n\mathbf{1}_{\neg n}\right)^\top \mathbf{y}_{\neg n}. \tag{4.33}$$

The independent state equations from 4.32 and 4.33 can be used to map the concentration and mole fractions gradients again as

$$\vec{\nabla}\mathbf{y}_{\neg n} = \frac{1}{c_\mathrm{T}\left(\mathbf{c}_{\neg n}\right)}\left[\mathbf{I}_{\neg n,\neg n} + \frac{\mathbf{c}_{\neg n}}{c_\mathrm{T}\left(\mathbf{c}_{\neg n}\right)\overline{V}_n}\left(\overline{\mathbf{v}}_{\neg n} - \overline{V}_n\mathbf{1}_{\neg n}\right)^\top\right]\vec{\nabla}\mathbf{c}_{\neg n} \tag{4.34}$$

and

$$\vec{\nabla}\mathbf{c}_{\neg n} = c_\mathrm{T}\left(\mathbf{y}_{\neg n}\right)\left[\mathbf{I}_{\neg n,\neg n} - c_\mathrm{T}\left(\mathbf{y}_{\neg n}\right)\mathbf{y}_{\neg n}\left(\overline{\mathbf{v}}_{\neg n} - \overline{V}_n\mathbf{1}_{\neg n}\right)^\top\right]\vec{\nabla}\mathbf{y}_{\neg n}. \tag{4.35}$$

Note that because each entry of $\vec{\nabla}\mathbf{y}_{\neg n}$ and $\vec{\nabla}\mathbf{c}_{\neg n}$ is independent, both transformations are bijective, unlike the transformations of Eqs. 4.30 and 4.31.

4.3 Dynamics in the salt–charge basis

4.3.1 Onsager–Stefan–Maxwell framework

As discussed in the introduction, the force–explicit Onsager–Stefan–Maxwell constitutive laws take the matrix form

$$-\nabla\boldsymbol{\mu} = \mathbf{M}\vec{\mathbf{n}}, \tag{4.36}$$

where $\mathbf{M}$ is a $n \times n$ matrix containing the Onsager drag coefficients and whose elements relate to Stefan–Maxwell diffusivities through Eq. 4.2. The second law of thermodynamics mandates that $\mathbf{M}$ is both positive semidefinite [96] and symmetric $\left(\mathbf{M} = \mathbf{M}^{\top}\right)$ as a consequence of the time-reversal symmetry and time-translational invariance of correlations between microscopic composition fluctuations [96, 101, 123].

Transformation to the salt–charge basis yields

$$-\nabla\boldsymbol{\mu}_Z = \mathbf{M}_Z\vec{\mathbf{n}}_Z, \tag{4.37}$$

where $\mathbf{M}_Z$ can be decomposed in block form such that

$$\mathbf{M}_Z = \mathbf{Z}\mathbf{M}\mathbf{Z}^{\top} = \begin{bmatrix} \mathbf{M}_\nu & \mathbf{m}_z \\ \mathbf{m}_z^{\top} & M_{zz} \end{bmatrix}. \tag{4.38}$$

The submatrix $\mathbf{M}_\nu$ is an $(n-1)\times(n-1)$ square matrix, $\mathbf{m}_z$ is a $(n-1)$-dimensional column matrix, and M_{zz} is a scalar. The congruence transformation in equation 4.37 implies that $\mathbf{M}$ is symmetric positive semidefinite if and only if $\mathbf{M}_Z$ is symmetric positive semidefinite, and that both matrices have equal rank [64].

Flux-explicit formulations of the tranpsort laws are often used to facilitate practical implementations of mass-transfer models. Therefore it is useful to develop an inverted form of the Onsager–Stefan–Maxwell equations. This requires some care because of the singularity of $\mathbf{M}$. To understand this inversion it is important to consider convective mass transport.

Analyses of molecular transport distinguish between *convective motion*, where all species are carried together at the same velocity, and *diffusive motion*, where

species move relative of one another. To represent this separation, the molar flux vector is typically decomposed as

$$\vec{\mathbf{n}} = \vec{\mathbf{j}} + \vec{v}\mathbf{c}, \tag{4.39}$$

where $\vec{\mathbf{j}}$ denotes the diffusive component, capturing species fluxes relative to the mass-average velocity, and $\vec{v}\mathbf{c}$ accounts for convective transport, with each component representing the product between the corresponding entry of $\mathbf{c}$ and the mass-average velocity $\vec{v}$ defined through Eq. 4.22. Utilizing fluxes relative to the mass-average velocity, the inverted, flux-explicit OSM equations, stated respectively over the species and salt–charge bases, take the form

$$\vec{\mathbf{j}} = -\mathbf{L}\nabla\boldsymbol{\mu} \quad \text{and} \quad \vec{\mathbf{j}}_Z = -\mathbf{L}_Z\nabla\boldsymbol{\mu}_Z, \tag{4.40}$$

respectively. Here $\mathbf{L}$ is a $n \times n$ matrix consisting of the Onsager transport coefficient matrix and $\mathbf{L}_Z$ follows a similar construction of $\mathbf{M}_Z$ such that

$$\vec{\mathbf{j}}_Z = \begin{bmatrix} \vec{\mathbf{j}}_\nu \\ \frac{\vec{i}}{F\|\mathbf{z}\|} \end{bmatrix} = -\begin{bmatrix} \mathbf{L}_\nu & \mathbf{l}_z \\ \mathbf{l}_z^\top & L_{zz} \end{bmatrix} \begin{bmatrix} \nabla\boldsymbol{\mu}_\nu \\ F\|\mathbf{z}\|\nabla\Phi_z \end{bmatrix}. \tag{4.41}$$

Converting the matrix of force–explicit transport matrix $\mathbf{M}$ to the Onsager transport matrix $\mathbf{L}$ is challenging because of the nullspace of $\mathbf{M}$; however, Helfand [124] and Fong [63] have resolved the transformations between these transport coefficients in the case where the excess fluxes are referenced to the mass-average velocity as

$$\mathbf{L} = \lim_{\gamma\to 0}\left(\mathbf{M} + \frac{\overline{\mathbf{m}}\,\overline{\mathbf{m}}^\top}{\gamma}\right)^{-1} \quad \text{or} \quad \mathbf{M} = \lim_{\gamma\to 0}\left(\mathbf{L} + \frac{\mathbf{c}\mathbf{c}^\top}{\gamma}\right)^{-1}. \tag{4.42}$$

It was proved that $\mathbf{L}$ is symmetric and positive semidefinite whenever $\mathbf{M}$ is, and that $\mathbf{L}$ has a one-dimensional nullspace for which $\overline{\mathbf{m}}$ is a basis, i.e., $\mathbf{L}\overline{\mathbf{m}} = \mathbf{o}$ [105].

For solutions where a singular species m is present in great excess, it is convenient to use the species velocity $\vec{v}_m$ as the reference velocity for convection, following Newman [58]. The excess molar flux of species i relative to the velocity of species m, notated $\vec{J}_i^{\,m}$, can be transformed to and from the mass-average velocity $\vec{J}_i$ through

$$\vec{\mathbf{j}}^{\,m} = \left(\mathbf{I} - \frac{\mathbf{c}\mathbf{i}_m^\top}{c_m}\right)\vec{\mathbf{j}} \quad \text{and} \quad \vec{\mathbf{j}} = \left(\mathbf{I} - \frac{\mathbf{c}\overline{\mathbf{m}}^\top}{\rho}\right)\vec{\mathbf{j}}^{\,m}, \tag{4.43}$$

where $\mathbf{i}_m$ represents the mth column of the $n \times n$ identity matrix $\mathbf{I}$. Similar to the total species fluxes $\vec{\mathbf{n}}$, the excess species fluxes $\vec{\mathbf{j}}$ and $\vec{\mathbf{j}}^m$ are n-dimensional column vectors whose ith entries are the species excess fluxes relative to the mass-average velocity $\vec{J}_i$ and species-referenced excess fluxes $\vec{J}_i^m$, respectively. Use of species-referenced excess fluxes changes the corresponding Onsager transport coefficients $\mathbf{L}^m$ in the flux-explicit transport laws. Because the row and column spaces of $\mathbf{L}$ and $\mathbf{L}^m$ share the same kernel, they are linked by transformations of the form

$$\mathbf{L}^m = \left(\mathbf{I} - \frac{\mathbf{c}\mathbf{i}_m^\top}{c_m}\right)\mathbf{L}\left(\mathbf{I} - \frac{\mathbf{i}_m\mathbf{c}^\top}{c_m}\right) \quad \text{and} \quad \mathbf{L} = \left(\mathbf{I} - \frac{\mathbf{c}\overline{\mathbf{m}}^\top}{\rho}\right)\mathbf{L}^m\left(\mathbf{I} - \frac{\overline{\mathbf{m}}\mathbf{c}^\top}{\rho}\right), \tag{4.44}$$

which do not require passage through the force-explicit form of the transport laws.

While the mass-averaged and species-referenced excess fluxes are the most common forms of reference velocities, any particular reference velocity $\vec{v}^*$ can be used in establishing the flux-explicit parametrization of the Onsager laws. Similar to Eq. 4.40, letting $\mathbf{L}^*$ represent the Onsager transport coefficients based on the excess species fluxes $\vec{\mathbf{j}}^*$ relative to some particular reference velocity $\vec{v}^*$,

$$\vec{\mathbf{j}}^* = -\mathbf{L}^*\vec{\nabla}\boldsymbol{\mu}, \tag{4.45}$$

where

$$\mathbf{M} = \lim_{\gamma\to 0}\left(\mathbf{L}^* + \frac{\mathbf{c}\mathbf{c}^\top}{\gamma}\right)^{-1} \tag{4.46}$$

defines the process of converting the Onsager transport coefficient to the unique force-explicit transport matrix $\mathbf{M}$. Note that $\mathbf{M}$ so defined has a one-dimensional nullspace spanned by $\mathbf{c}$ and is positive semidefinite and symmetric if and only if the transport matrix $\mathbf{L}^*$ is.

4.3.2 Electroneutral composition

It is often useful to isolate the effects of charge variation on electrolyte properties. The salt–charge basis provides a starting point for this; any set of concentrations in the salt–charge basis $\mathbf{c}_Z$ can be sent to a neutralized composition $\mathbf{c}^0$ by setting the last element to zero (remember c_z is directly proportional to excess charge

density through Eq. 4.18). One can use the properties of $\mathbf{Z}^{-1}$ outlined in Eqs. 4.9 and 4.11 to show that

$$\mathbf{c}^0 = \mathbf{N}\mathbf{c}_\nu = \aleph\mathbf{N}^\top\mathbf{c} = \left(\mathbf{I} - \hat{\mathbf{z}}\hat{\mathbf{z}}^\top\right)\mathbf{c}. \tag{4.47}$$

Notice that $(\mathbf{I} - \hat{\mathbf{z}}\hat{\mathbf{z}}^\top)$ is a linear operator that orthogonally projects any set of concentrations to its nearest neutral set (an electroneutral set of concentrations maps to itself). In other words, the $\left(\mathbf{I} - \hat{\mathbf{z}}\hat{\mathbf{z}}^\top\right)$ operator finds the 'closest' neutral concentration set $\mathbf{c}^0$ in the sense that the magnitude of $\mathbf{c} - \mathbf{c}^0$ is minimized. The updated total electroneutral concentration can be defined through

$$c_{\mathrm{T}}^0 = \mathbf{1}^\top\mathbf{c}^0. \tag{4.48}$$

This generally differs from c_{T}; the two total concentrations match when $\rho_{\mathrm{e}} \neq 0$ only if $\mathbf{1}^\top\mathbf{z} = 0$.

The newly defined set of electroneutral concentrations can be used to define corresponding electroneutral mole fractions $\mathbf{y}^0$ following a process similar to that discussed in Section 4.2.3. The nearest neutral mole fractions corresponding to $\mathbf{c}^0$ are

$$\mathbf{y}^0\left(\rho_e\right) = \frac{1}{c_{\mathrm{T}}^0}\mathbf{c}^0 = \left(\frac{1}{\boldsymbol{\nu}_\nu^\top\mathbf{y}_\nu}\right)\left(\mathbf{I} - \hat{\mathbf{z}}\hat{\mathbf{z}}^\top\right)\mathbf{y}. \tag{4.49}$$

There are two important things to note here: (1) electroneutral mole fractions still satisfy the mole fraction sum requirement $\left(\mathbf{1}^\top\mathbf{y}^0 = 1\right)$ and (2) the matrix inner product $\boldsymbol{\nu}_\nu^\top\mathbf{y}_\nu$, and therefore $\mathbf{y}^0$, may be a function of excess charge density ρ_e because of the mole-fraction-sum constraint. Expansion of Eq. 4.24 shows their explicit relationship to be

$$\boldsymbol{\nu}_\nu^\top\mathbf{y}_\nu = 1 - \nu_z y_z = \left(1 - \frac{\nu_z\rho_e}{F\|\mathbf{z}\|c_{\mathrm{T}}}\right). \tag{4.50}$$

As expected, the $\left(\mathbf{I} - \hat{\mathbf{z}}\hat{\mathbf{z}}^\top\right)$ operator appears in the right of Eq. 4.49. Define the nearest set of electroneutral mole fractions $\mathbf{y}^\perp$ as

$$\mathbf{y}^\perp = \left(\mathbf{I} - \hat{\mathbf{z}}\hat{\mathbf{z}}^\top\right)\mathbf{y}. \tag{4.51}$$

The column matrix $\mathbf{y}^{\perp}$ is convenient because it is entirely independent of charge; however, it violates the traditional requirement that mole fractions sum to one, as the charged component is simply omitted.

We now define a unique set of charge-dependent mole fractions $\mathbf{y}^{\varnothing}$ that is directly proportional to excess charge density. This definition introduces an electroneutral reference composition that isolates purely chemical variations from charge-induced perturbations, enabling the portion of species flux attributable to non-electroneutrality to be distinguished from other transport contributions. Replacing $\mathbf{y}$ with $\mathbf{y}_Z$, utilizing the relationships in Eqs. 4.5, 4.23, and 4.49 , and rearranging leads to

$$\mathbf{y}^{\varnothing} = y_z \left(\hat{\mathbf{z}} - \nu_z \mathbf{y}^0 \right). \tag{4.52}$$

Left multiplying by $\mathbf{1}^{\top}$ verifies that the elements of $\mathbf{y}^{\varnothing}$ sum to zero (since $\mathbf{1}^{\top}\mathbf{y}^0 = 1$ and $\mathbf{1}^{\top}\hat{\mathbf{z}} = \nu_z$). Finally, the definitions in Eqs. 4.49 and 4.52 can be used to decompose $\mathbf{y}$ as

$$\mathbf{y} = \mathbf{y}^0 + \mathbf{y}^{\varnothing} \quad \text{or} \quad \mathbf{y} = \mathbf{y}^{\perp} + y_z \hat{\mathbf{z}}. \tag{4.53}$$

Each formulation has its advantages – the decomposition on the left ensures that mole fractions of $\mathbf{y}^0$ and $\mathbf{y}^{\varnothing}$ always sum to one and zero, respectively, while the equation on the right isolates charge-related effects, as $\mathbf{y}^{\perp}$ is independent of charge. These systematic methods of decomposing $\mathbf{y}$ will prove useful when isolating and understanding the independent effects of charge variance in electrolytes.

4.3.3 Thermodynamic factors

Thermodynamic factors are essential when implementing a simulation of any transport system because they map composition gradients into electrochemical-potential gradients in isothermal, isobaric situations. Monroe and Newman introduced dimensionless Darken factors [125] which are the derivative of the (log) activity of species i with respect to the mole fraction of species $j < n$, leaving temperature,

pressure, and all mole fractions except those of species j and n constant. In terms of species activities, the Darken factor Q_{ij} between species i and j is defined as

$$Q_{ij} = y_i \left(\frac{\partial \ln a_i}{\partial y_j} \right)_{T,p,y_{k\neq j,n}} = \delta_{ij} + y_i \left(\frac{\partial \ln \lambda_i}{\partial y_j} \right), \tag{4.54}$$

where δ_{ij} represents the Kronecker delta and λ_i is the activity coefficient of species i such that $a_i = \lambda_i y_i$ [101]. Let $\mathbf{Q}$ represent the $n \times n$ matrix of dimensionless Darken factors consisting of entries Q_{ij}.

Due to the constraint on species mole fractions expressed by Eq. 4.24, one cannot alter the mole fraction of one species alone. By convention, Monroe and Newman's definition assumes that when y_j is experimentally varied, y_n is appropriately altered to maintain the mole fraction sum. Because any direct variation in y_n is infeasible, resulting in $Q_{in} = 0$ for all i (that is, the last column of $\mathbf{Q}$ is zero). Another restriction that is placed on the Darken factors is through the Gibbs-Duhem equation. The y_i proportionality constant in the Darken factor's definition ensures that $\mathbf{1}^\top \mathbf{Q} = \mathbf{o}^\top$ (i.e., the terms in each column of $\mathbf{Q}$ sum to zero). These two constraints on Q_{ij} make the last column and row redundant because only $\mathbf{Q}_{\neg n,\neg n}$ (the $(n-1) \times (n-1)$ submatrix of $\mathbf{Q}$ formed by deleting the nth row and nth column) needs to be considered for a full thermodynamic characterization.

We now have the tools to parameterize isothermal, isobaric chemical potentials generally, by starting with the formulation developed by Monroe and Newman [125]. The set of all chemical potential gradients, as constrained by the Gibbs–Duhem equation, takes the form

$$\operatorname{diag}(\mathbf{y}) \nabla \boldsymbol{\mu} = RT \mathbf{Q} \nabla \mathbf{y} = RT \begin{bmatrix} \mathbf{I}_{n-1} \\ -\mathbf{1}^\top \end{bmatrix} \mathbf{Q}_{\neg n,\neg n} \begin{bmatrix} \mathbf{I}_{n-1} & \mathbf{o} \end{bmatrix} \nabla \mathbf{y}, \tag{4.55}$$

where $\operatorname{diag}(\mathbf{v})$ represents the diagonal matrix whose ith diagonal entry is v_i, the ith row entry of $\mathbf{v}$, and $\mathbf{I}_{n-1}$ is the $(n-1) \times (n-1)$ identity matrix. One key advantage of working with Monroe and Newman's Darken factors is that they easily relate to the Hessian with respect to composition $\mathbf{K}$ of the molar Gibbs energy $\overline{G}$, whose entries are

$$K_{ij} = \frac{1}{RT} \left(\frac{\partial^2 \overline{G}}{\partial y_i \partial y_j} \right)_{T,p,y_{k\neq i,j,n}} \tag{4.56}$$

within this space of independent variable composition descriptors. It has been proven that $\mathbf{K}$ is symmetric and necessarily positive semidefinite [101], and the thermodynamic derivatives in its definition require that $K_{in} = K_{nj} = 0$ for all i and j. The independent Darken factors $\mathbf{Q}_{\neg n,\neg n}$ depend on $\mathbf{K}_{\neg n,\neg n}$ through

$$\mathbf{Q}_{\neg n,\neg n} = \mathbf{Y}^{-1}\mathbf{K}_{\neg n,\neg n} \tag{4.57}$$

where the definition

$$\mathbf{Y}^{-1} = \mathrm{diag}(\mathbf{y}_{\neg n}) - \mathbf{y}_{\neg n}\mathbf{y}_{\neg n}^{\top} \tag{4.58}$$

adapts Monroe and Newman's indicial definition into the matrix nomenclature. Using Eq. 4.53 we can decompose $\mathbf{Y}^{-1}$ into the sum of its electroneutral and charge variation component as

$$\mathbf{Y}^{-1} = \mathbf{Y}^{-1,0} + \mathbf{Y}^{-1,\varnothing} \tag{4.59}$$

where

$$\mathbf{Y}^{-1,0} = \mathrm{diag}(\mathbf{y}_{\neg n}^{0}) - \mathbf{y}_{\neg n}^{0}\mathbf{y}_{\neg n}^{0^{\top}} \tag{4.60}$$

and

$$\mathbf{Y}^{-1,\varnothing} = \mathrm{diag}(\mathbf{y}_{\neg n}^{\varnothing}) - \mathbf{y}_{\neg n}^{0}\mathbf{y}_{\neg n}^{\varnothing^{\top}} - \mathbf{y}_{\neg n}^{\varnothing}\mathbf{y}_{\neg n}^{0^{\top}} - \mathbf{y}_{\neg n}^{\varnothing}\mathbf{y}_{\neg n}^{\varnothing^{\top}}. \tag{4.61}$$

The Hessian $\mathbf{K}$ helps to express the Darken factors more simply under non-ideal situations since it conveniently separates into two parts,

$$\mathbf{K}_{\neg n,\neg n} = \mathbf{Y} + \Delta\mathbf{K}_{\neg n,\neg n}, \tag{4.62}$$

where $\Delta\mathbf{K}$ is a $n \times n$ symmetric matrix which accounts for deviations from ideal mixing free energy. The structure of $\mathbf{K}$ mandates that $\Delta K_{in} = \Delta K_{nj} = 0$; thus only the $\Delta\mathbf{K}_{\neg n,\neg n}$ submatrix is needed for a full thermodynamic characterization. The $(n-1) \times (n-1)$ matrix $\mathbf{Y}$ expresses the derivatives of ideal mixing free energy and is defined as

$$\mathbf{Y} = \mathrm{diag}(\mathbf{y}_{\neg n})^{-1} + \frac{\mathbf{1}\mathbf{1}^{\top}}{y_n} \tag{4.63}$$

such that $y_n = \mathbf{i}_n^\top \mathbf{y}$ (that is, y_n is the last element of $\mathbf{y}$). Again, using Eq. 4.53 we can decompose $\mathbf{Y}$ into

$$\mathbf{Y} = \mathbf{Y}^0 + \mathbf{Y}^\varnothing \tag{4.64}$$

where

$$\mathbf{Y}^0 = \mathrm{diag}(\mathbf{y}_{\neg n}^0)^{-1} + \frac{\mathbf{1}\mathbf{1}^\top}{y_n^0} \tag{4.65}$$

and

$$\mathbf{Y}^\varnothing = -\mathrm{diag}(\mathbf{y}_{\neg n}^\varnothing)\mathrm{diag}(\mathbf{y}_{\neg n}^0)^{-1}\mathrm{diag}(\mathbf{y}_{\neg n})^{-1} - \frac{y_n^\varnothing}{y_n^0 y_n}\mathbf{1}\mathbf{1}^\top \tag{4.66}$$

such that $y_n^0 = \mathbf{i}_n^\top \mathbf{y}^0$ and $y_n^\varnothing = \mathbf{i}_n^\top \mathbf{y}^\varnothing$.

Van-Brunt's formulation of $\boldsymbol{\Delta}\mathbf{K}$ inherits a symmetry property from $\mathbf{K}$, making it easier to track the constraints that Maxwell relations impose on experimentally measured parameters. The definitions of standard thermodynamic states can be used to verify that $\mathbf{Q}_{\neg n,\neg n} = \mathbf{I}_{n-1}$ for ideal gas mixtures or isobaric ideal solutions, so $\boldsymbol{\Delta}\mathbf{K} = \mathbf{O}$ (the zero matrix) in these cases. Combining Eqs. 4.57, 4.62, and 4.64 results in a direct relationship between the Darken factors and the excess non-ideal free energies:

$$\mathbf{Q}_{\neg n,\neg n} = \mathbf{I}_{n-1} + \left(\mathbf{Y}^0 + \mathbf{Y}^\varnothing\right)\boldsymbol{\Delta}\mathbf{K}_{\neg n,\neg n}. \tag{4.67}$$

We start with the excess free energy, which can be decomposed as

$$\boldsymbol{\Delta}\mathbf{K} = \boldsymbol{\Delta}\mathbf{K}^0 + \boldsymbol{\Delta}\mathbf{K}^\varnothing, \tag{4.68}$$

wherein

$$\boldsymbol{\Delta}\mathbf{K}^0 = \aleph\mathbf{N}^\top\left(\boldsymbol{\Delta}\mathbf{K}\right)\aleph\mathbf{N}^\top \tag{4.69}$$

and

$$\boldsymbol{\Delta}\mathbf{K}^\varnothing = \left(\boldsymbol{\Delta}\mathbf{K}\right)\mathbf{z}\mathbf{z}^\top + \mathbf{z}\mathbf{z}^\top\left(\boldsymbol{\Delta}\mathbf{K}\right) - \mathbf{z}\mathbf{z}^\top\left(\boldsymbol{\Delta}\mathbf{K}\right)\mathbf{z}\mathbf{z}^\top. \tag{4.70}$$

Plugging Eqs. 4.68 and 4.64 into Eq. 4.62 yields

$$\mathbf{K} = \mathbf{K}^0 + \mathbf{K}^\varnothing = \left(\mathbf{Y}^0 + \boldsymbol{\Delta}\mathbf{K}^0\right) + \left(\mathbf{Y}^\varnothing + \boldsymbol{\Delta}\mathbf{K}^\varnothing\right) \tag{4.71}$$

Generally, the charge-dependent excess free energy $\left(\Delta\mathbf{K}^{\varnothing}\right)$ cannot be determined through macroscopic experiments. These contributions are typically minor and may be safely neglected in most systems.

We can now use the decomposition from Eqs. 4.59 and 4.68 to plug into the matrix of Darken factors. Simplifying and rearranging terms results in

$$\mathbf{Q}_{\neg n,\neg n} = \mathbf{I}_{n-1} + \left(\mathbf{Y}^{-1,0}\Delta\mathbf{K}^{0}_{\neg n,\neg n}\right) + \left(\mathbf{Y}^{-1}\Delta\mathbf{K}^{\varnothing}_{\neg n,\neg n} + \mathbf{Y}^{-1,\varnothing}\Delta\mathbf{K}^{0}_{\neg n,\neg n}\right), \quad (4.72)$$

where the first term expresses the ideal mixing energies, the second term outlines the electroneutral contribution, and the last term reveals the charge dependence.

4.3.4 Neutralizable composition

The complete parametrization of the Darken factors is impeded for electrolytes because the $(n-1)$th species concentration cannot generally be varied without changing the system's electrical state. Goyal and Monroe addressed this issue with their 'core potential' approach, in which y_{n-1} is replaced by a normalized charge density such that charge is only associated with a single independent variable [126]. Unlike the salt–charge basis, however, the core potentials do not preserve the structures of the free energy and dissipation functions, and also lack the clear connection to reaction equilibria that underpins component chemical potentials. The following uses Goyal's core potential approach to extend Van-Brunt's salt–charge basis outside the conditions of local electroneutrality.

In the salt–charge basis, the nth entry of $\mathbf{y}_Z$ expresses the independent effects of excess-charge variation. As a result, one cannot directly apply the Monroe–Newman expansion of diffusion driving forces from Eq. 4.55 with Van-Brunt's parametrization from Eq. 4.67. Instead of discarding the nth entry, we discard the first entry of $\mathbf{y}_Z$ to create a sub-column of independent component composition variables. The resulting $(n-1)$-entry column matrix $\mathbf{x}$, defined as

$$\mathbf{x} = (\mathbf{y}_Z)_{\neg 1} = \mathbf{I}_{\neg 1,0}\mathbf{y}_Z, \quad (4.73)$$

contains the mole fractions of independent neutral components two through $n-1$ and molar excess charge, such that the mole fraction of component one is then

determined by Eq. 4.24. Note that this basis is analogous to Goyal's *neutralizable composition*, where the first $n-2$ entries are the *component composition* variables and the $(n-1)$-th entry is the *electrical state* variable.

The composition bases of $\mathbf{x}$ and $\mathbf{y}_{\neg n}$ connect through the affine transformation

$$\mathbf{x} = \mathbf{T}^{\mathbf{Z}\leftarrow\mathbf{I}}_{\neg 1,\neg n}\mathbf{y}_{\neg n} + (\mathbf{Z}^{-\top}\mathbf{i}_n)_{\neg 1} \quad \text{or} \quad \mathbf{y}_{\neg n} = \mathbf{T}^{\mathbf{I}\leftarrow\mathbf{Z}}_{\neg n,\neg 1}\mathbf{x} + \frac{1}{\boldsymbol{\nu}_Z^\top \mathbf{i}_1}(\mathbf{Z}^\top \mathbf{i}_1)_{\neg n} \tag{4.74}$$

in which the transformation matrices $\mathbf{T}^{\mathbf{Z}\leftarrow\mathbf{I}}_{\neg 1,\neg n}$ and $\mathbf{T}^{\mathbf{I}\leftarrow\mathbf{Z}}_{\neg n,\neg 1}$ are defined as

$$\mathbf{T}^{\mathbf{Z}\leftarrow\mathbf{I}}_{\neg 1,\neg n} = (\mathbf{Z}^{-\top})_{\neg 1,\neg n} - (\mathbf{Z}^{-\top}\mathbf{i}_n)_{\neg 1}\mathbf{1}^\top_{\neg n} \tag{4.75}$$

and

$$\mathbf{T}^{\mathbf{I}\leftarrow\mathbf{Z}}_{\neg n,\neg 1} = (\mathbf{Z}^{\top})_{\neg n,\neg 1} - \frac{1}{\boldsymbol{\nu}_Z^\top \mathbf{i}_1}(\mathbf{Z}^\top \mathbf{i}_1)_{\neg n}(\boldsymbol{\nu}_Z)^\top_{\neg 1} \tag{4.76}$$

Both transformation matrices are nonsingular and inverses of each other such that $\mathbf{T}^{\mathbf{Z}\leftarrow\mathbf{I}}_{\neg 1,\neg n} = (\mathbf{T}^{\mathbf{I}\leftarrow\mathbf{Z}}_{\neg n,\neg 1})^{-1}$.

This affine and invertible transformation affords a straightforward method of parameterizing the thermodynamic driving forces for diffusion. Similar to $\mathbf{K}$, the Hessian of molar Gibbs energy with respect to the salt–charge composition, $\mathbf{H}$, has entries

$$H_{ij} = \frac{1}{RT}\left(\frac{\partial^2 \overline{G}}{\partial(\mathbf{y}_Z)_i \partial(\mathbf{y}_Z)_j}\right)_{T,p,(\mathbf{y}_Z)_{k\neq i,j,1}} \tag{4.77}$$

where the first component (compared to the n-th component in $\mathbf{K}$) is varied to preserve mole-fraction sums. This definition mandates that $H_{i1} = H_{1j} = 0$ for all i and j, meaning that only the $\mathbf{H}_{\neg 1,\neg 1}$ submatrix needs to be considered for a full thermodynamic characterization.

The composition and salt–charge Hessian matrices, $\mathbf{K}_{\neg n,\neg n}$ and $\mathbf{H}_{\neg 1,\neg 1}$, respectively, have similar properties. Differentiation of Eq. 4.74 shows that the composition gradients connect through a bijective linear map,

$$\nabla\mathbf{x} = \mathbf{T}^{\mathbf{Z}\leftarrow\mathbf{I}}_{\neg 1,\neg n}\nabla\mathbf{y}_{\neg n} \quad \text{and} \quad \nabla\mathbf{y}_{\neg n} = \mathbf{T}^{\mathbf{I}\leftarrow\mathbf{Z}}_{\neg n,\neg 1}\nabla\mathbf{x}. \tag{4.78}$$

By applying the chain rule, one therefore gets

$$\mathbf{K}_{\neg n,\neg n} = \left(\mathbf{T}^{\mathbf{Z}\leftarrow\mathbf{I}}_{\neg 1,\neg n}\right)^\top \mathbf{H}_{\neg 1,\neg 1}\mathbf{T}^{\mathbf{Z}\leftarrow\mathbf{I}}_{\neg 1,\neg n}, \tag{4.79}$$

showing that a congruence transformation connects the two Hessian matrices. Because $\mathbf{K}_{\neg n,\neg n}$ and $\mathbf{H}_{\neg 1,\neg 1}$ are congruent, they have equal signatures: both are positive semidefinite, with equal numbers of positive eigenvalues. We can use this transformation to eliminate $\mathbf{K}_{\neg n,\neg n}$ from Eq. 4.57 to yield

$$\mathbf{Q}_{\neg n,\neg n} = \mathbf{Y}^{-1} \left(\mathbf{T}^{\mathbf{Z}\leftarrow\mathbf{I}}_{\neg 1,\neg n}\right)^{\top} \mathbf{H}_{\neg 1,\neg 1} \mathbf{T}^{\mathbf{Z}\leftarrow\mathbf{I}}_{\neg 1,\neg n}. \tag{4.80}$$

Here we have a direct relation between the independent Darken factors and the independent entries of the molar Gibbs energy Hessian. All the terms that express how species activities and electric potential vary with excess charge reside in the nth row of $\mathbf{H}_{\neg 1,\neg 1}$, and the electric potential's composition dependence resides in the nth column, thereby distinguishing electrical effects. The symmetry of $\mathbf{H}_{\neg 1,\neg 1}$ implies that it can be parameterized in terms of its $\frac{1}{2}n(n-1)$ independent lower-triangular material properties alone. The bottom right entry of $\mathbf{H}_{\neg 1,\neg 1}$ provides an equation of state for charge, as we will explore in future sections.

4.4 Common assumptions in transport modeling

Eqs. 4.40 and 4.55 present a comprehensive framework for modeling isobaric and isothermal electrolytic systems. However, the generalized form of this law depends on n^2 composition-dependent parameters. These include:

- n partial molar volumes, which form the vector $\bar{\mathbf{v}}$ and define how total molarity changes with composition;
- $\frac{1}{2}n(n-1)$ thermodynamic derivatives, which contribute to the symmetric excess Hessian $\Delta\mathbf{K}_{\neg n,\neg n}$, used to compute the Darken-factor matrix $\mathbf{Q}_{\neg n,\neg n}$;
- $\frac{1}{2}n(n-1)$ Onsager diffusivities, defining the symmetric, transport matrix $\mathbf{L}$, or the same number of Stefan–Maxwell diffusivities, which relate to the Onsager drag matrix $\mathbf{M}$.

This section examines several simplifications that are often used to reduce the burden of specifying all these transport parameters. A summary of each assumption and their structural effect on the OSM framework is outlined in Table 4.1.

Assumption	Mathematical Implication	Comments
Constant total concentration	$\overline{\mathbf{v}}_{\neg n} = \overline{V}_n \mathbf{1}_{\neg n}$	Each species in the mixture has equal molar volumes $\overline{V}_i$.
Negligible mixing energies	$\Delta\mathbf{K}_{\neg n,\neg n} \propto \left[\mathrm{diag}(\mathbf{y}^0_{\neg n})^{-1} + \frac{\mathbf{1}\mathbf{1}^\top}{y^0_n}\right]$	The set of independent Darken factors $\mathbf{Q}_{\neg n,\neg n}$ must be diagonal.
Negligible ion-ion drag	$\mathbf{L}^{m,\mathrm{ideal}} = \frac{c_\mathrm{T}}{RTc_m}\mathrm{diag}(\mathscr{D})\mathrm{diag}(\mathbf{c})$	The activity drag coefficients not including the solvent or excess species m are set to zero.
Nernst-Planck	• All of the above • $c_\mathrm{T} = c_m$ • $\frac{F\lVert\mathbf{z}\rVert}{RT}\Phi_\mathrm{P} = \sum_{i=1}^n \hat{z}_i \ln\left(1 + \frac{y_z \hat{z}_i}{y_i^\perp}\right)$ • $\rho_e = 0$ • $\nabla\rho_e = 0$ • $\Delta k = 0$	The Poisson overpotential is set equal to the charge contribution of the chemical potentials. Additionally, charge is prohibited from accumulating.

Table 4.1: Mathematical consequences of common modeling assumptions on the OSM framework

4.4.1 Excluded volume effects

In many analyses of mass transport in condensed systems, solute-volume effects are often disregarded by assuming that the total molar concentration c_T remains nearly constant with changing composition. In order for this assumption to hold, the off-diagonal terms of the bracketed term of Eqs. 4.34 and 4.35 must be zero when mapping between $\vec{\nabla}\mathbf{c}_{\neg n}$ and $\vec{\nabla}\mathbf{y}_{\neg n}$. This assumption only holds if

$$\overline{\mathbf{v}}_{\neg n} = \overline{V}_n \mathbf{1}_{\neg n}. \tag{4.81}$$

In other words, each species in the mixture must have equal molar volumes. While this assumption can be made safely for ideal gasses, they are almost never valid

for solids or liquids. For example, Zhao et al. measured apparent molar volumes of lithium salts in ethylene carbonate–based solvent mixtures and showed that extrapolation to infinite dilution yields standard partial molar volumes that vary systematically with solvent composition. Reported partial molar volumes for $LiClO_4$ and LiBr differ by 20–40% across common carbonate mixtures [127]. These observations confirm that assuming constant partial molar volumes can introduce non-negligible errors in liquid transport models. Note that the assumption of a constant c_T cannot be justified through this dilute solution approximation.

4.4.2 Negligible mixing energies

Similar to the assumption of negligible volume effects, cross-diffusion induced mixing is zero if and only if $\mathbf{Q}_{\neg n,\neg n}$ is diagonal. Combined Eqs. 4.57 and 4.62 reveal that this criteria is met when

$$\mathbf{Q}_{\neg n,\neg n} = \mathbf{I}_{\neg n,\neg n} + \mathbf{Y}^{-1}\Delta\mathbf{K}_{\neg n,\neg n} \approx (1+\Delta k)\,\mathbf{I}_{\neg n,\neg n} \tag{4.82}$$

where Δk is a function of $\mathbf{y}_{\neg n}$. The structure of 4.82 suggests that $\Delta\mathbf{K}^{\text{ideal}}_{\neg n,\neg n}$ must be proportional to $\mathbf{Y}$ such that

$$\Delta\mathbf{K}_{\neg n,\neg n} \propto \left[\text{diag}(\mathbf{y}^0_{\neg n})^{-1} + \frac{\mathbf{1}\mathbf{1}^\top}{y^0_n}\right]. \tag{4.83}$$

Additionally, thermodynamic stability demands that that the parameter $\Delta k > -1$ because the free-energy Hessians must be positive definite.

Studies that simplify transport models by invoking 'ideal behavior' typically assume thermodynamically ideal mixing, meaning that the entropy of mixing for each component is equivalent to that in an ideal gas mixture [128]. This assumption is expressed mathematically by setting $\mathbf{Q}_{\neg n,\neg n} = \mathbf{I}_{\neg n,\neg n}$ [129]. In the case of volatile species, ideal behavior also implies that each component follows Raoult's law — this is referred to as the 'ideal solution' approximation. Alternatively, one may assume all solutes follow Henry's law with constant solubility [130]. Both of these thermodynamic idealizations ultimately require $\Delta k = 0$ in Eq. 4.82 for the Darken factors.

4.4.3 Negligible ion-ion drag

In the force-explicit form of the Onsager-Stefan-Maxwell transport laws, the thermodynamic forces are balanced by the frictional forces between different species in the solution. For some electrolytic solutions certain species' drag coefficients are negligible in relation to others within the system, allowing one to set the frictional interaction parameter $\mathscr{K}_{ij}$ between two minimally interacting species i and j to zero. This simplifying assumption has the potential to significantly reduce the complexity of the Onsager transport coefficients contained in $\mathbf{L}$ and thus the computational effort required in practical implementations of this framework. Newman [58] and others often work with diffusion coefficients $\mathscr{D}_{ij}$ which are inversely proportional to the drag coefficients through

$$\mathscr{K}_{ij} = \frac{RTc_i c_j}{c_{\mathrm{T}} \mathscr{D}_{ij}}. \tag{4.84}$$

When considering the neglect of certain species–species interactions, however, it is often convenient to work with $\mathscr{K}_{ij}$ because the diffusion coefficients become infinitely large under the no-drag assumption. After setting $\mathscr{K}_{ij}$ to zero when pairwise interactions between i and j are to be neglected, the remaining drag coefficients can be converted back into diffusion coefficients for further simulations.

In the case of a singular excess species m dominating all species–species interactions within an electrolyte, the transport coefficients $\mathbf{L}$ simplify considerably. In this scenario, it is convenient to work with velocities referenced to species m as outlined in Eq. 4.43. Assuming $\mathscr{K}_{i\neq m,j} = 0$ for all species j except for m, the species-referenced transport coefficients reduce to

$$\mathbf{L}^{m,\mathrm{ideal}} = \mathrm{diag}(\mathbf{c}_{\neg m})\mathrm{diag}(\boldsymbol{\mathscr{K}}_{\neg m})^{-1}\mathrm{diag}(\mathbf{c}_{\neg m}), \tag{4.85}$$

where $\boldsymbol{\mathscr{K}}$ is a n-entry column matrix whose ith element is the drag coefficient $\mathscr{K}_{im}$. Alternatively, one can transform this back to the commonly used diffusion coefficients yielding

$$\mathbf{L}^{m,\mathrm{ideal}} = \frac{c_{\mathrm{T}}}{RTc_m}\mathrm{diag}(\boldsymbol{\mathscr{D}}_{\neg m})\mathrm{diag}(\mathbf{c}_{\neg m}), \tag{4.86}$$

where $\mathscr{D}$ is a n-dimensional column matrix whose the ith element is $\mathscr{D}_{im}$. One could also apply Eq. 4.44 to compute the mass-average velocity referenced transport matrix $\mathbf{L}^{\text{ideal}}$. Note that the diagonal structure of $\mathbf{L}^{m,\text{ideal}}$ in Eqs. 4.85 and 4.86 confirms the absence of cross-diffusional drag.

Defining what constitutes a 'moderately dilute' electrolyte remains ambiguous. Even at low salt concentrations, interactions between solutes—particularly ions—can produce noticeable drag effects in electrolyte solutions. This drag stems primarily from electrostatic interactions, which are much stronger than typical molecular forces and thus have a greater impact on diffusion. When ions move in a correlated way, the resulting drag increases significantly, as demonstrated by molecular dynamics studies from Wheeler and Newman [131, 132] and Persson and colleagues [133, 134]. Drawing on data compiled by Chapman and Newman [135], Bizeray et al. showed that in aqueous systems, ion-ion drag becomes non-negligible above 0.05 M salt concentration [59]. Furthermore, nonaqueous solvents may exhibit these effects at even lower concentrations due to their lower salt solubility.

4.5 Case study: simplification of OSM to Nernst–Planck

The Nernst Planck equation is perhaps the most ubiquitous transport model used throughout electrochemistry. Here we show that applying all the simplifying assumptions outlined in section 4.4 distills the OSM framework down to the form of the Nernst-Planck equation.

Although binary electrolytes are often treated using simplified transport models, such formulations are commonly introduced only for single-salt systems and rely on assumptions that are not always made explicit. The value of the present approach is that Nernst–Planck–type transport equations emerge here as controlled reductions of the full OSM framework, and can be obtained for more general concentrated electrolytes rather than being restricted to the binary limit. This provides a transparent connection between commonly used transport models and

the underlying multicomponent description, while clarifying the assumptions under which such simplifications are valid.

First, start with the species-referenced flux equation. Combining Eqs. 4.7, 4.9, and 4.45, we can expand the flux OSM equation as

$$\vec{\mathbf{j}}^{m} = -\mathbf{L}^{m}[\aleph\vec{\nabla}\boldsymbol{\mu}_{\nu} + F\mathbf{z}\vec{\nabla}\Phi_{z}] \tag{4.87}$$

where

$$\nabla\boldsymbol{\mu}_{\nu} = RT\mathbf{N}^{\top}\left(\mathrm{diag}(\mathbf{y})^{-1} + (\mathbf{I}_{n} - \mathbf{1}\mathbf{y}^{\top})\Delta\mathbf{K}_{\neg n,\neg n}\right)\nabla\mathbf{y}. \tag{4.88}$$

The combination of Eqs. 4.87 and 4.88 fully describes transport in any isothermal and isobaric electrolyte.

Applying the assumtion of thermodynamic ideality simplifies the matrix of Darken factors in Eq. 4.82 to

$$\mathbf{Q}^{\mathrm{ideal}}_{\neg n,\neg n} = \mathbf{I}_{n-1}. \tag{4.89}$$

Plugging $\mathbf{Q}^{\mathrm{ideal}}_{\neg n,\neg n}$ into Eq. 4.55 and using the fact that $\sum y_i = 1$ results in the reduction of Eq. 4.88 to

$$\nabla\boldsymbol{\mu}^{\mathrm{ideal}}_{\nu} = RT\mathbf{N}^{\top}\nabla\ln(\mathbf{y}). \tag{4.90}$$

Additionally, from Eq. 4.8 we know $\Phi_z = \Phi$ for ideal solutions ($a_i = 1$ for all i species), simplifying the total flux equation to

$$\vec{\mathbf{j}}^{m,\mathrm{ideal}} = -\mathbf{L}^{m}[RT\aleph\mathbf{N}^{\top}\nabla\ln(\mathbf{y}) + F\mathbf{z}\nabla\Phi]. \tag{4.91}$$

Following a similar to the approach by Goyal and Monroe [126], we partition the naive potential Φ as

$$\Phi(\mathbf{x}) = \Phi_{0}(\mathbf{x}_{\neg n}) - \Phi_{\mathrm{P}}(\mathbf{x}) \tag{4.92}$$

such that it is referenced to the *electroneutral potential* Φ_0 corresponding to the electroneutral reference compositions $\mathbf{y}^0$. The *Poisson overpotential* Φ_{P} is the portion of the naive potential that contributes to electrical non-neutrality. This is negative because non-neutrality is typically thought of as being imposed by an

externally applied voltage, whereas the naive potential and electroneutral potential measures internal electrical energy.

In order to arrive at a form similar to the Nernst–Planck equation, define the Nernst–Planck overpotential Φ_{NP} as the charge contribution of the ideal chemical potentials in Eq. 4.91 such that

$$\nabla \Phi_{\mathrm{NP}} = -\frac{RT}{F\|\mathbf{z}\|}\hat{\mathbf{z}}^{\top}\nabla \ln(\mathbf{y}). \tag{4.93}$$

Recall that the $\aleph\mathbf{N}^{\top}$ operator sends a set of mole fractions to its nearest neutral set. Eq. 4.93 is effectively incorporating the excluded charge contribution from the first term of 4.91 into its second term involving the solution potential. Integrating this equation with the boundary equation of $\Phi_{\mathrm{NP}}|_{y_z=0} = 0$ yields the charge EOS for the Nernst-Planck overpotential:

$$\frac{F\|\mathbf{z}\|}{RT}\Phi_{\mathrm{NP}} = \sum_{i=1}^{n}\hat{z}_i \ln\left(\frac{y_i^{\perp}}{y_i}\right) = \sum_{i=1}^{n}\hat{z}_i \ln\left(1+\frac{y_z\hat{z}_i}{y_i^{\perp}}\right), \tag{4.94}$$

where Eq. 4.53 is used to separate the charge contribution to each mole fraction. Intuitively, the Nernst–Planck potential is dependent on all independent $(n-1)$ mole fractions. Unfortunately, an explicit function of charge density (x_n) is not able to be written in a closed form algebraic expression. Alternatively, one could assume changes in Φ_{NP} are small such that it is approximated by the linearized form of Eq. 4.94—a valid assumption for most electrolytic solutions. Linearizing Eq. 4.94 and rearranging for y_z yields

$$y_z \approx -\frac{F\Phi_{\mathrm{NP}}}{RT}\left(\sum_{i=1}^{n}\frac{\hat{z}_i^2}{y_i^{\perp}}\right)^{-1}, \tag{4.95}$$

where the case $y_i^{\perp} = 0$ is non-physical. The structure of equation 4.95 is somewhat jarring because it consists of a weighted harmonic mean of $y_i^{\perp}$, where the weights are $\hat{z}_i^2$ (i.e. $y_i^{\perp}$ values with a larger $\hat{z}_i^2$ contribute more significantly to y_z). This is in stark contrast with the linearized Poisson-Boltzmann theory where charge density is proportional to a charge-weighted arithmetic mean [136]. Nonetheless, simplification of the general OSM flux equation of 4.91 to Nernst–Planck form mandates the charge EOS to follow 4.94.

We now assume that a reference species m dominates the ion-ion interactions by applying $\mathbf{L}^{m,\text{ideal}}$ from Eq. 4.86 to simplify the flux expression to

$$\vec{\mathbf{j}}^{m,\text{ideal}} = -\frac{c_\text{T}^2}{c_m}\text{diag}(\boldsymbol{\mathscr{D}})\text{diag}(\mathbf{y})\boldsymbol{\aleph}\mathbf{N}^\top\text{diag}(\mathbf{y})^{-1}\nabla\mathbf{y} - \frac{c_\text{T}}{c_m}F\text{diag}(\mathbf{u})\text{diag}(\mathbf{c})\mathbf{z}\nabla\Phi \quad (4.96)$$

where $\mathbf{u}$ is a column matrix containing each of the the species mobilities u_i defined through the Nernst–Einstein relation $u_i = \mathscr{D}_{i,m}/RT$.

Incorporating the Nernst–Planck overpotential into Eq. 4.96 conveniently splits the flux equation into two portions as

$$\vec{\mathbf{j}}^{m,\text{ideal}} = \mathbf{j}_\text{NP} - \frac{c_\text{T}^2}{c_m}\text{diag}(\boldsymbol{\mathscr{D}})\hat{\mathbf{z}}\nabla y_z - y_z\frac{Fc_\text{T}^2}{c_m}\text{diag}(\mathbf{u})\text{diag}(\mathbf{z})\hat{\mathbf{z}}\nabla\Phi_0 \quad (4.97)$$

where $\mathbf{j}_\text{NP}$ represents the Nernst–Planck contribution towards the general flux, defined as

$$\mathbf{j}_\text{NP} = -\frac{c_\text{T}^2}{c_m}\text{diag}(\boldsymbol{\mathscr{D}})\nabla\mathbf{y}^\perp - \frac{Fc_\text{T}^2}{c_m}\text{diag}(\mathbf{u})\text{diag}(\mathbf{z})\mathbf{y}^\perp\nabla\Phi_0. \quad (4.98)$$

Under the condition of electroneutrality ($y_z = 0$ uniformly), the last two terms in Eq. 4.97 vanish. The remaining flux equation is

$$\vec{\mathbf{j}}^{m,\text{ideal},0} = -\frac{c_\text{T}^2}{c_m}\text{diag}(\boldsymbol{\mathscr{D}})\nabla\mathbf{y}^\perp - \frac{Fc_\text{T}^2}{c_m}\text{diag}(\mathbf{u})\text{diag}(\mathbf{z})\mathbf{y}^\perp\nabla\Phi_0 \quad (4.99)$$

Finally, upon exclusion of volume effects ($\overline{\mathbf{v}}_{\neg n} = \overline{V}_n\mathbf{1}_{\neg n}$ from section 4.4.1) and assumption of dilute solution ($c_\text{T} \approx c_m$), we are left with the familiar Nernst–Planck expression of

$$\vec{\mathbf{j}}^{m,\text{ideal},0} = -\text{diag}(\boldsymbol{\mathscr{D}})\nabla\mathbf{c}^0 - F\text{diag}(\mathbf{u})\text{diag}(\mathbf{z})\mathbf{c}^0\nabla\Phi_0. \quad (4.100)$$

This is identical to the commonly used indicial form of the Nernst–Planck equation,

$$j_i = -\mathscr{D}_i\nabla c_i - Fz_iu_ic_i\nabla\Phi \quad (4.101)$$

4.6 Conclusions

This chapter has presented a rigorous examination of the Onsager–Stefan–Maxwell (OSM) framework, an essential approach for modeling ionic transport phenomena in concentrated electrolyte solutions. Through detailed derivations and structured analysis, it demonstrates that the OSM equations offer significant advantages over classical dilute-solution models like the Nernst–Planck equations, particularly in systems where ion–ion and ion–solvent interactions are pronounced, where thermodynamic nonideality is significant, and where excluded-volume effects cannot be neglected.

In systematically exploring the theoretical foundations, the salt–charge basis emerged as a particularly effective representation for analyzing complex multicomponent electrolytes. This framework clearly delineates charge and concentration related effects, facilitating deeper insight into the subtle interplay of thermodynamics and transport processes. The chapter's exploration into electroneutral compositions and thermodynamic factors underscored the intricate relationship between these aspects, reinforcing the critical role played by charge neutrality and mixing effects in dictating electrolyte behavior.

The evaluation of common simplifying assumptions – such as excluded volume effects, negligible mixing energies, and ion–ion drag – reveals the practical limitations inherent in simplified models. While these approximations can significantly ease computational and experimental demands, the analysis indicates caution is required in their application. Especially under high-concentration conditions common to redox flow batteries, overlooking these interactions can introduce significant inaccuracies in modeling electrolyte behavior and thus battery performance.

The case study provided in this chapter, which simplified the full OSM equations into the electroneutral Nernst–Planck laws, illustrated the limitations of employing simpler theoretical constructs. Although the Nernst–Planck model remains broadly useful for ideal and infinitely dilute solutions, the nuanced behavior captured by the comprehensive OSM framework is critical for the accurate prediction of transport phenomena in most practical electrolytes.

From a broader perspective, the significance of the Onsager–Stefan–Maxwell (OSM) framework in electrochemistry arises from its ability to describe ionic transport under the coupled, non-ideal, and high-concentration conditions that are intrinsic to redox flow battery operation. In RFBs, electrolytes are continuously circulated through porous electrodes and separators, giving rise to sustained spatial gradients in concentration, electrostatic potential, and pressure that cannot be reliably captured using dilute-solution models. The OSM framework therefore provides the theoretical basis required to interpret transport-driven phenomena central to RFB performance, including active-species crossover, membrane fouling, and capacity fade observed in earlier chapters.

Although the OSM framework remains computationally and experimentally demanding, the transport insights it enables are uniquely valuable. Future research should aim to systematically quantify the influence of each simplifying assumption explored in this chapter. By doing so, it will become possible to identify which assumptions are benign across different regimes and which introduce significant inaccuracies. Such efforts will refine the criteria for applying reduced-order models and enhance the practical utility of the OSM framework in real-world electrochemical applications.

4.A Appendices

4.A.1 Worked example of a salt–charge basis

Consider a solution of water (H_2O) and acetonitrile (CH_3CN) containing the dissolved salts of potassium chloride (KCl) and calcium phosphate ($(Ca)_3(PO_4)_2$). In this electrolytic solution, a total of $n = 6$ species are present [H_2O, CH_3CN, K^+, Cl^-, Ca^{+2}, and ${PO_4}^{-3}$] which results in $n - 1 = 5$ independent simple association equilibrium reactions. One possible combination is

$$\begin{aligned} H_2O &\rightleftharpoons H_2O \\ CH_3CN &\rightleftharpoons CH_3CN \\ K^+ + Cl^- &\rightleftharpoons KCl \\ 3\,Ca^+ + 2\,{PO_4}^{-3} &\rightleftharpoons Ca_3(PO_4)_2 \\ Ca^{+2} + 2\,Cl^- &\rightleftharpoons CaCl_2 \end{aligned}$$

where the first two reactions are the trivial equilibrium between the neutral species and themselves. Salts such as K_3PO_4 were omitted here for simplicity, as their inclusion would not alter the transport formulation; equivalent electrolyte representations differ only by choice of basis and lead to the same governing equations. Additionally, recall that products of the equilibrium reactions are referred to as *components* and the reactants as *species*.

With the electrolyte fully defined, let $\mathbf{z}$ be a n-dimensional column matrix consisting of the species equivalent charges. For the outlined example, $\mathbf{z} = [0, 0, +1, -1, +2, -3]^\top$. Additionally, let $\boldsymbol{\nu}_i$ be defined as a n-dimensional column matrix containing the stoichiometric coefficients ν_{ij} of reactant species j in the ith equilibrium equation. As a result of Guggenheim's relation, each column of $\boldsymbol{\nu}_i$ must be orthogonal to $\mathbf{z}$ such that $\boldsymbol{\nu}_i^\top \mathbf{z} = 0$ [137]. For example, in the

fifth equilibrium reaction above:

$$\boldsymbol{\nu}_5^\top \mathbf{z} = \begin{bmatrix} 0 & 0 & 0 & 2 & 1 & 0 \end{bmatrix} \cdot \begin{bmatrix} 0 \\ 0 \\ +1 \\ -1 \\ +2 \\ -3 \end{bmatrix} = 0$$

By construction, the combined column matrices of $\boldsymbol{\nu}_i$ and $\mathbf{z}$ are linearly independent; thus, the n-tuple $\{\boldsymbol{\nu}_1, \ldots, \boldsymbol{\nu}_{n-1}, \mathbf{z}\}$ form a basis for the entire composition space.

The mapping of the electrochemical potentials of any n species to $n-1$ components and its charge density through the salt–charge basis is captured by the $n \times n$ transformation matrix $\mathbf{Z}$. For the electrolyte outlined above,

$$\mathbf{Z} = \begin{bmatrix} \boldsymbol{\nu}_1^\top \\ \boldsymbol{\nu}_2^\top \\ \boldsymbol{\nu}_3^\top \\ \boldsymbol{\nu}_4^\top \\ \boldsymbol{\nu}_5^\top \\ \mathbf{z}^\top / \|\mathbf{z}\| \end{bmatrix} = \begin{bmatrix} 1 & 0 & 0 & 0 & 0 & 0 \\ 0 & 1 & 0 & 0 & 0 & 0 \\ 0 & 0 & 1 & 1 & 0 & 0 \\ 0 & 0 & 0 & 0 & 3 & 2 \\ 0 & 0 & 0 & 2 & 1 & 0 \\ 0 & 0 & 1/\sqrt{15} & -1/\sqrt{15} & 2/\sqrt{15} & -3/\sqrt{15} \end{bmatrix}$$

where $\|\mathbf{z}\| = \sqrt{\mathbf{z}^\top \mathbf{z}}$. By construction, $\mathbf{Z}$ is an invertible matrix where each of the first $n-1$ rows is orthogonal to the last row.

Let $\boldsymbol{\mu}$ be a n-dimensional column matrix containing the species electrochemical potentials. Multiplication of $\boldsymbol{\mu}$ by the transformation matrix $\mathbf{Z}$ converts the electrochemical potential of each species to their respective components. Following the example through,

$$\boldsymbol{\mu}_Z = \begin{bmatrix} \boldsymbol{\mu}_\nu \\ \mu_z \end{bmatrix} = \begin{bmatrix} \mu_{\mathrm{H_2O}} \\ \mu_{\mathrm{CH_3CN}} \\ \mu_{\mathrm{KCl}} \\ \mu_{\mathrm{Ca_3(PO_4)_2}} \\ \mu_{\mathrm{CaCl_2}} \\ \mu_z \end{bmatrix} = \mathbf{Z}\boldsymbol{\mu} = \begin{bmatrix} \mu_{\mathrm{H_2O}} \\ \mu_{\mathrm{CH_3CN}} \\ \mu_{\mathrm{K^+}} + \mu_{\mathrm{Cl^-}} \\ 3\mu_{\mathrm{Ca^{+2}}} + 2\mu_{\mathrm{PO_4^{-3}}} \\ \mu_{\mathrm{Ca^{+2}}} + 2\mu_{\mathrm{Cl^-}} \\ (\mu_{\mathrm{K^+}} - \mu_{\mathrm{Cl^-}} + 2\mu_{\mathrm{Ca^{+2}}} - 3\mu_{\mathrm{PO_4^{-3}}})/\|\mathbf{z}\| \end{bmatrix}$$

where the first $n-1$ rows are the component electrochemical potentials, $\boldsymbol{\mu}_{\boldsymbol{\nu}}$. The last element, μ_z is related to the salt–charge potential, Φ_z, such that

$$\mu_z = F\|\mathbf{z}\|\,\Phi_z$$

The construction of $\boldsymbol{\mu}_Z$ above highlights the generalization of Guggenheim's process of grouping species electrochemical potentials into new quantities that represent electrically neutral combinations of species [104].

4.A.2 Decomposing the inverse transformation matrix

The proof begins by showing that $\mathbf{N}^\top\mathbf{N}$ is always invertible.

> Assertion: For every real $m \times n$ matrix $\mathbf{C}$ with rank m and $n > m$, the matrix product $\mathbf{C}^\top\mathbf{C}$ is invertible.
>
> Proof: Let $\mathbf{C}^\top\mathbf{a} = \mathbf{0}$ for an m-element vector $\mathbf{a}$. Thus,
>
> $$\mathbf{C}^\top\mathbf{a} = \mathbf{C}\mathbf{C}^\top\mathbf{a} = \mathbf{a}^\top\mathbf{C}\mathbf{C}^\top\mathbf{a} = \left(\mathbf{C}^\top\mathbf{a}\right)^\top\mathbf{C}^\top\mathbf{a} = \mathbf{0}$$
>
> It is known that $\mathbf{b}^\top\mathbf{b} = \mathbf{0}$ if and only if $\mathbf{b} = \mathbf{0}$. Let $\mathbf{b} = \mathbf{C}^\top\mathbf{a}$ to reveal that $\mathbf{C}\mathbf{C}^\top\mathbf{a} = \mathbf{0}$ implies $\mathbf{C}^\top\mathbf{a} = \mathbf{0}$.
>
> The rank of $\mathbf{C}^\top$ is m so $\mathbf{C}^\top\mathbf{a} = \mathbf{0}$ if and only if $\mathbf{a} = \mathbf{0}$. From the proof above, it is known that $\mathbf{C}\mathbf{C}^\top\mathbf{a} = \mathbf{0}$ if and only if $\mathbf{a} = \mathbf{0}$. Thus, $\mathbf{C}\mathbf{C}^\top$ is invertible.
>
> Let $\mathbf{C} = \mathbf{N}^\top$ to see that $\mathbf{C}\mathbf{C}^\top = \mathbf{N}^\top\mathbf{N}$. Thus, $\mathbf{N}^\top\mathbf{N}$ is invertible.

Given the $(n-1) \times n$ matrix $\mathbf{N}^\top$ with rank $(n-1)$, aim to construct a unique $n \times (n-1)$ right inverse matrix $\boldsymbol{\aleph}$ such that $\mathbf{N}^\top\boldsymbol{\aleph} = \mathbf{I}$. Using results from the proof above,

$$\mathbf{I} = \mathbf{N}^\top\boldsymbol{\aleph} = \left(\mathbf{N}^\top\mathbf{N}\right)\left(\mathbf{N}^\top\mathbf{N}\right)^{-1} = \mathbf{N}^\top\left[\mathbf{N}\left(\mathbf{N}^\top\mathbf{N}\right)^{-1}\right],$$

thus proving

$$\boldsymbol{\aleph} = \mathbf{N}\left(\mathbf{N}^\top\mathbf{N}\right)^{-1}.$$

4.A.3 Deriving the electroneutral projection operator

Algebraic manipulation of $\boldsymbol{\aleph}$ shows that $\mathbf{N}\boldsymbol{\aleph}^\top = \boldsymbol{\aleph}\mathbf{N}^\top$:

$$\mathbf{N}\boldsymbol{\aleph}^\top = \mathbf{N}\left[\mathbf{N}\left(\mathbf{N}^\top\mathbf{N}\right)^{-1}\right]^\top = \mathbf{N}\left(\mathbf{N}^\top\mathbf{N}\right)^{-\top}\mathbf{N}^\top = \mathbf{N}\left(\mathbf{N}^\top\mathbf{N}\right)^{-1}\mathbf{N}^\top = \boldsymbol{\aleph}\mathbf{N}^\top.$$

Now, use the fact that $\mathbf{Z}$ is invertible to show $\boldsymbol{\aleph}\mathbf{N}^\top = \mathbf{I} - \hat{\mathbf{z}}\hat{\mathbf{z}}^\top$:

$$\mathbf{I} = \mathbf{Z}^{-1}\mathbf{Z} = \begin{bmatrix}\boldsymbol{\aleph} & \hat{\mathbf{z}}\end{bmatrix}\begin{bmatrix}\mathbf{N}^\top \\ \hat{\mathbf{z}}^\top\end{bmatrix} = \boldsymbol{\aleph}\mathbf{N}^\top + \hat{\mathbf{z}}\hat{\mathbf{z}}^\top.$$

5

Thermo-mechanical Properties of Electrolytes

Contents

5.1 Introduction

Critical to the long-term viability of flow batteries systems is the understanding of electrolyte mechanical properties, which can substantially impact electrolyte management, system efficiency, and component durability [37]. Although prior chapters of this work have extensively explored electrolyte behavior specific to RFB systems, directly characterizing the mechanical properties of RFB chemistries is of limited long-term value due to the rapid evolution of electrolyte formulations [138, 139]. Instead, this chapter focuses on techniques to measure mechanical properties of a well-established and prevalent lithium-ion electrolyte system—namely, $LiPF_6$ in a mixture of ethylene carbonate (EC) and ethyl methyl carbonate (EMC)—which serves as an effective proxy due to its widespread industrial application, well-characterized thermodynamic and transport properties, and relevance to contemporary battery technologies [112, 140–142].

Specifically, this chapter reports measurements of the dynamic viscosity, density, and speed of sound of electrolytic solutions. These measurements are used to determine four key mechanical parameters: the isentropic bulk modulus (K_s), the thermal expansion modulus (K_θ), the isothermal bulk modulus (K_T), and the coefficient of thermal expansion (α_V). These parameters are fundamental to understanding the mechanical response and thermomechanical behavior of concentrated electrolytes, directly influencing electrolyte design, fluid handling, and safety considerations [143, 144]. Insights derived from the Li-ion electrolyte system characterization presented here are leveraged to draw broader conclusions applicable to RFB electrolytes. By elucidating these general mechanical behaviors, this analysis aims to inform the design, operation, and optimization of future RFB systems, facilitating advancements in electrolyte design and enhancing overall system reliability and efficiency.

5.2 Background

Electrolytes, which mediate ion transport in lithium-ion batteries, are crucial to device performance [141]. Almost all electrolytes in commercial lithium-ion batteries are liquids containing ethylene carbonate (EC), a cyclic compound whose high dielectric constant raises ionic conductivity by facilitating dissociation of lithium salts [145–150]. Because it also reacts to form a stable, ionically conductive and electronically insulating solid–electrolyte interphase (SEI) on graphite, EC is touted as an essential constituent of state-of-the-art lithium-ion electrolytes [151, 152]. Pure EC is solid at room temperature, however, so lithium-ion electrolytes also typically contain at least one linear-carbonate cosolvent—e.g., ethyl methyl carbonate (EMC) or dimethyl carbonate (DMC)—to enable mixing and ultimately lower the solution's viscosity [153, 154]. Importantly, the molarities of linear and cyclic carbonates are comparable within the cosolvent blends typically used for commercial lithium-ion batteries [155–158].

Despite linear and cyclic carbonates being present in similar proportions, most battery models treat liquid-electrolyte cosolvents as a single entity, neglecting specific solvent–solvent interactions. Recent studies have probed this 'single-solvent approximation' by studying the distinct behaviours of EC and EMC in dual-solvent blends. In a previous study by Wang et al., ternary EMC:EC:$LiPF_6$ blends were subjected to constant-current polarization in Hittorf experiments [159]. The EMC and EC components were found to move at substantially different rates relative to the dissolved salt, resulting in extreme solvent segregation near the electrode/liquid interfaces that could be parametrized quantitatively in the form of an electro-osmotic drag coefficient for EC. Meanwhile, Jung et al. set out to challenge the electrical aspect of the single-solvent approximation, showing with concentration-cell measurements that steady liquid-junction potentials of the order of tens to hundreds of millivolts arise between solutions with different cosolvent fractions but identical salt contents [99]. Because battery operation drives solvent segregation, it is imperative to understand how local variations in cosolvent composition within porous electrodes impact liquid-phase transport properties.

The effects of local pressure and temperature variations on electrolyte performance have been fairly well established, but the impact of cosolvent segregation on bulk thermal and mechanical properties remains largely unexplored. Heenan et al. tracked internal mechanical strain and temperature within commercial 18650 lithium-ion cells using advanced in-situ synchrotron X-ray diffraction methods [160]. They found that internal temperatures reach 70°C during a discharge rate of 2.9C for NMC811 versus Gr-SiOx cells with ambient temperatures at 20°C. Azimuthal tensile stress in the Cu current collector was reported to reach approximately 250 MPa. While this stress does not directly correspond to a liquid-phase pressure and would not translate quantitatively to electrolyte pressure, it indicates substantial internal mechanical loading, suggesting that assuming constant electrolyte pressure may not always be appropriate. The effect of temperature on electrolyte flow is mediated by the liquid's thermal expansion coefficient, and that of stress is mediated by viscosity. This study explores how the local composition variation accompanying solvent segregation impacts these mechanical properties.

Recent literature provides evidence of current-driven electrolyte flow on both macroscopic and microscopic scales, further compounding the need to understand electrolyte properties. Aiken et al. found evidence of systematic electrolyte movement within cylindrical Li-ion cells as they charge and discharge [161]. In the fully discharged state, electrolyte is absorbed into the electrode winding and evenly distributed. During charging, however, lithium intercalation into anodes can drive substantial volume expansion that forces pores to close and drives liquid out of the winding. On a microscopic scale, other groups have shown that solvent molecules within cation solvation shells experience drag associated with electric fields, leading to bulk electrolyte motion [162–166]. This evidence of electrolyte flow during battery operation forces us to consider a volume balance for nonisothermal, nonisobaric systems where electrolyte density varies with its species' molar concentrations.

The Newtonian viscosity η of an electrolytic solution depends on temperature, pressure, and composition, and appears in equations that model momentum transport. Mechanical and thermomechanical properties can also contribute to

mass transport, and mesh into the governing equations from concentrated-solution theory. The continuity of species i within an electrolytic solution in the absence of homogeneous reactions is governed by

$$\frac{\partial c_{\mathrm{T}} y_i}{\partial t} = -\vec{\nabla} \cdot \vec{N}_i, \tag{5.1}$$

where the total molar concentration c_{T} is defined as the inverse of the molar volume $\overline{V}$ $\left(c_{\mathrm{T}} = 1/\overline{V}\right)$, y_i is the particle fraction of species i, and $\vec{N}_i$ is a vector representing the total molar flux of species i. Newman and Chapman's analysis of restricted diffusion in binary solutions showed how the species material balances can be combined with thermodynamic constitutive laws to obtain an equation that expresses solution-volume continuity [110]. Goyal and Monroe employed a similar strategy [107], extending the volume balance to account for variations in local pressure p and absolute temperature T, showing that the local volume balance in a diffusion system comprising n species is

$$\frac{1}{K_T}\frac{\partial p}{\partial t} - \alpha_V \frac{\partial T}{\partial t} = -\vec{\nabla} \cdot \vec{v}^{\square} + \sum_i \vec{N}_i \cdot \vec{\nabla}\overline{V}_i, \tag{5.2}$$

in which the isothermal bulk modulus K_T and volumetric coefficient of thermal expansion α_V are intensive material properties, defined as

$$\frac{1}{K_T} = -\frac{1}{V}\left(\frac{\partial V}{\partial p}\right)_T \quad \text{and} \quad \alpha_V = \frac{1}{V}\left(\frac{\partial V}{\partial T}\right)_p, \tag{5.3}$$

respectively, and $\vec{v}^{\square}$ is the material's volume average velocity, defined as

$$\vec{v}^{\square} = \sum_i \overline{V}_i \vec{N}_i. \tag{5.4}$$

Generally, α_V, K_T, and $\overline{V}_i$ are functions of an electrolyte's temperature, pressure, and composition, and are needed to simulate how stress, temperature, and composition changes within electrolytes can drive their flow.

This chapter first quantifies how mass density ρ varies as a function of temperature and composition across the EMC:EC:$LiPF_6$ composition space, data which largely establish the composition and temperature dependences of the component partial molar volumes $\overline{V}_i$ [58]. Correlations describing density are developed and

used to determine the coefficient of thermal expansion α_V across the EMC:EC:$LiPF_6$ composition space, providing deeper insights into how local temperature variation might drive the flow of a battery electrolyte. Next, acoustic time-of-flight measurements are reported; combined with densitometry, these determine the composition and temperature dependence of the isentropic bulk modulus K_s for EMC:EC:$LiPF_6$ solutions. I discuss the importance of this compressibility parameter and develop thermodynamic relationships that connect K_s to the solution's isothermal bulk modulus K_T, which appears in volume continuity equation 5.2. Finally, I discuss the relative importances of α_V and K_T for the accurate modeling of electrolyte flow.

5.3 Experimental

5.3.1 Electrolyte preparation

Due to the strong reactivity of lithium with oxygen and moisture in the air, all electrolyte samples were combined from their precursors within an argon-filled glovebox (4GB, Inert Technologies) with trace amounts of O_2 and H_2O (<1 ppm). The samples were prepared using an analytical balance (EX124, OHAUS Explorer) with a readability of 0.1 mg and uncertainty of 0.2 mg. All precursor chemicals were battery-grade and were sourced from Sigma-Aldrich with purities of 99.9% or higher.

Each sample is defined by its $LiPF_6$ salt molality m and fraction of EMC cosolvent f. Given the mass fractions of EC ω_{EC}, EMC ω_{EMC}, and $LiPF_6$ ω_{LiPF_6}, the salt molalities and cosolvent fractions are defined as

$$m = \frac{\omega_{LiPF_6}/M_{LiPF_6}}{\omega_{EC} + \omega_{EMC}} \quad \text{and} \quad f = \frac{\omega_{EC}}{\omega_{EC} + \omega_{EMC}} \tag{5.5}$$

where $M_{LiPF_6} = 151.905\ \mathrm{g\,mol^{-1}}$ is the molar mass of $LiPF_6$. Mass fractions are positive, and by definition are constrained such that $\omega_{EC} + \omega_{EMC} + \omega_{LiPF_6} = 1$. In the current experimental programme, a total of 23 electrolytes were characterized mechanically; their compositions are shown on the ternary diagram in Fig. 5.1.

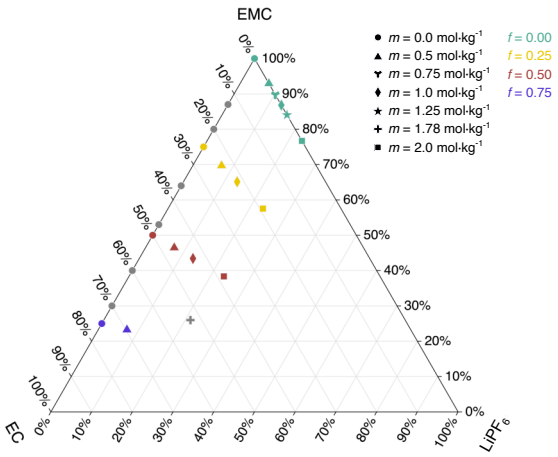

Figure 5.1: Ternary diagram of the mass fractions of $LiPF_6$ in EC/EMC cosolvent. Each of the 23 tested solutions were gravimetrically mixed in an argon-filled glovebox.

5.3.2 Densitometry

Densities ρ for each solution were measured using a high-precision oscillating U-tube density meter (DMA4100, Anton Paar), with an accuracy of 0.1 mg cm^{-3} and an uncertainty of 0.2 mg cm^{-3} during standard calibration with ultrapure water ($\leq 0.05\ \mu S\,cm^{-1}$, Avidity Science) and ethanol ($\geq$99.5%, Sigma-Aldrich). The inbuilt Peltier thermostat maintains temperature with a precision of 5 mK. Measurements were taken at ambient pressure with temperatures ranging from 281.15 K to 318.15 K in 1 K increments. A few samples were tested to a lower temperature of 278.15 K.

5.3.3 Acoustic measurements

The experimental setup for the speed of sound measurements was reported earlier by Wang et al. [113]. Experimental studies of $LiPF_6$ in carbonate-based non-aqueous electrolytes indicate that hydrolysis and decomposition reactions at room temperature proceed slowly in the absence of significant moisture, such that short-term exposure to ambient conditions does not lead to rapid degradation [167]. On this basis, speed-of-sound measurements were conducted outside the glovebox within one day of electrolyte preparation.

Experiments measured acoustic time-of-flight through a quartz cuvette filled with electrolyte and immersed in an isothermal bath. A 5-MHz contact transducer (V109, Olympus NDT) was connected to a pulser/receiver (DPR300, JST Ultrasonics), which outputs to an oscilloscope (HS5, TiePie) to digitize the reflected waveform received by the computer. The echo signal was amplified and digitized at a rate of 100 MHz. The transducer was coupled to the quartz cuvette (100-QS, Hellma Macrocell) with ultrasound gel (Aquasonic 100, Parker Labs) to match their acoustic impedances. Approximately 8 mL of sample was pipetted into the cuvette and covered with parafilm before submerging both the transducer and cuevette into a water bath (Haake A10, Thermo Scientific). Extreme care was taken to ensure that no part of the parafilm was in contact with the water bath and the liquid level of the sample was below that of the water bath. A K-type stainless steel thermocouple (397-1236, RS Pro) was placed inside the cuvette and in the adjacent water bath; temperatures were recorded every 90 seconds to ensure that temperature was equilibrated between the sample and the bath.

The speed of sound measurements range from temperatures of 278.15 K to 318.15 K in 1 K increments. Two measurements were obtained per temperature per sample. The temperature ramp rate of the water bath was 20 $\mathrm{K\,hr^{-1}}$. To minimize dissolution of the ultrasound gel during an experiment, each sample was split into two runs with temperatures ramped slowly from 298.15 K to 318.15 K back to 298.15 K, and 298.15 K to 278.15 K back to 298.15 K. Fresh ultrasound gel was reapplied between each run.

The acoustic transit time was calculated through a cross-correlation of the echo signal to find the location in time of the reflected peaks. The total distance traveled by the pulse $2L$, where L is the internal distance between faces of the cuvette, was then divided by the transit time to obtain the sound speed for each liquid sample. Note that the internal length of the cuvette was calibrated by a separate experiment in which the measured times of flight for ultrapure water were matched to previously reported data sets [168, 169], as shown in Appendix 5.A.1.

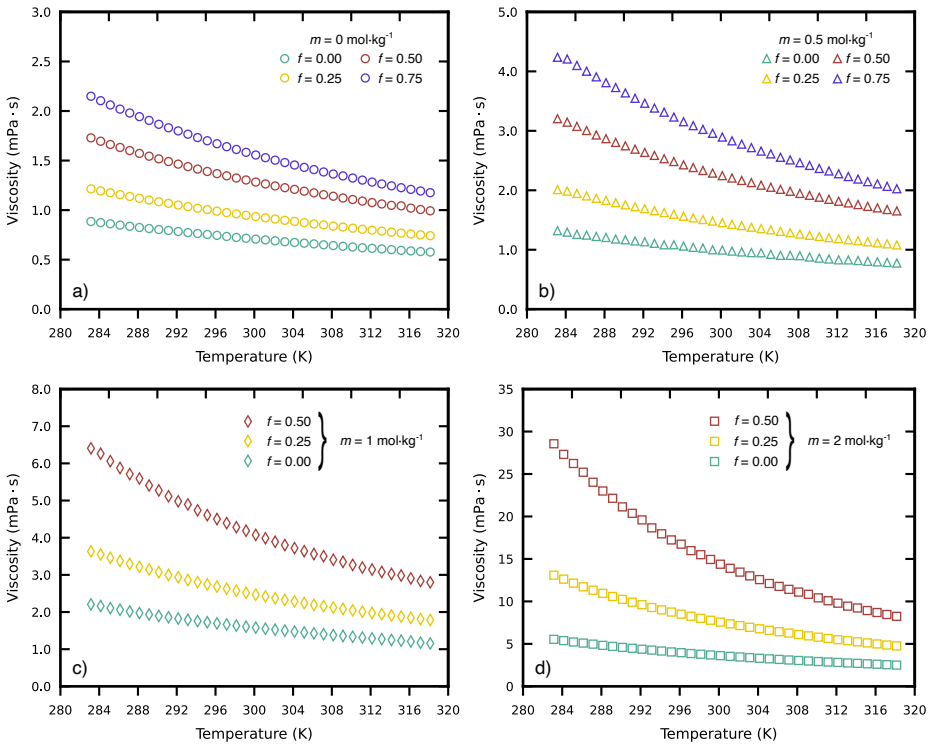

Figure 5.2: Viscosity measurements for $LiPF_6$ in EC/EMC. For conciseness, only solutions with salt molalities $m = 0, 0.5, 1, 2$ and fraction EC $f = 0, 0.25, 0.5, 0.75$ are plotted. Tabular data for each of the tested electrolyte compositions are included in Appendix 5.A.2

5.4 Results and discussion

5.4.1 Dynamic viscosity

Fig. 5.2 depicts the dynamic viscosities for select compositions. Appendix 5.A.2 contains data for each of the tested electrolyte compositions. As expected, the viscosity for all samples decreased with increasing temperature. At lower temperatures (below 300 K), increasing EC weight fraction dramatically increases its viscosity. This usually leads to a severe drop in conductivity which, in turn, will limit cell performance. While this trend is true for all $LiPF_6$ molalities, it is especially pronounced at higher concentrations—a feature attributed to the high melting point of EC. As a result, higher EC content contributes to a larger increase in viscosity compared to $LiPF_6$ molarity at temperatures below 300 K. At higher temperatures, both EC and $LiPF_6$ increase the bulk electrolyte's viscosity to a similar extent. Similar trends have been observed with other electrolyte formulations [153, 170–173].

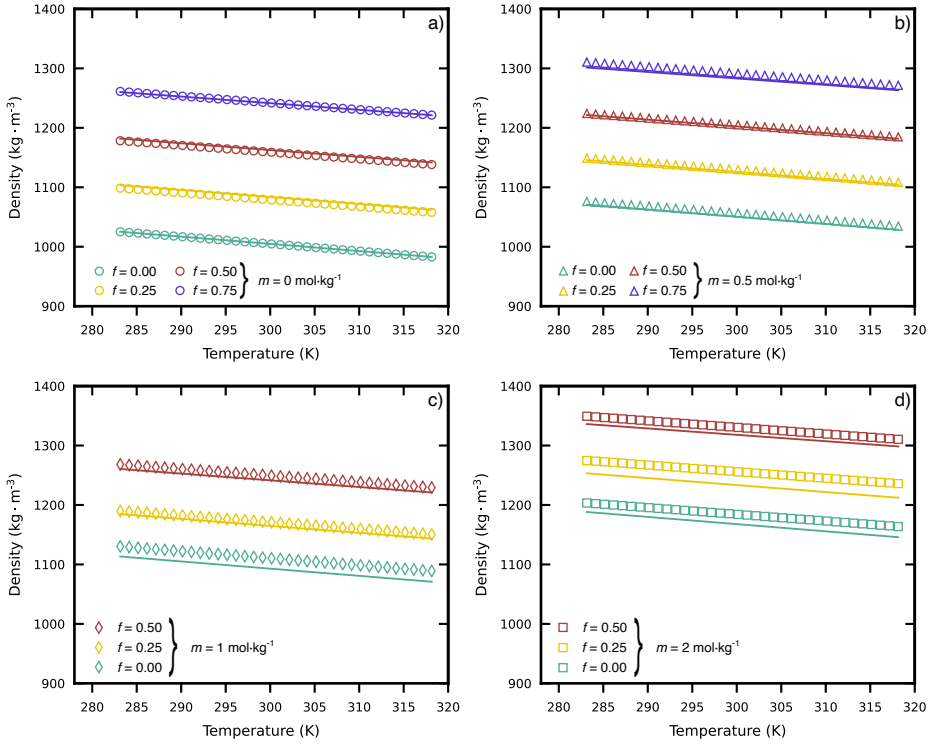

Figure 5.3: Density measurements for $LiPF_6$ in EC/EMC. For conciseness, only solutions with salt molalities $m = 0, 0.5, 1, 2$ and fraction EC $f = 0, 0.25, 0.5, 0.75$ are plotted. Tabular data for each of the tested electrolyte compositions are included in Appendix 5.A.3

5.4.2 Density and sound speed

Densitometry data for select samples are shown in Fig. 5.3; Appendix 5.A.3 contains the data for all tested solutions in tabular form. The densities for the binary $LiPF_6$ in pure EMC solutions are consistent with previous studies [174] (see Appendix 5.A.4). Density appears to have a strong linear dependence on temperature for all the tested solutions, which is commensurate with previous studies of $LiPF_6$ in PC.[120] Furthermore, both higher salt molalities m and EC cosolvent-weight-fraction f result in larger densities. Note that the data in Appendix 5.A.3 can be used to compute partial molar volumes but are not reported here since partial molar volumes for the same ternary electrolyte have already been published in a previous study [99].

Fig. 5.4 presents the speed of sound in various electrolyte compositions; Appendix 5.A.5 displays data for all electrolyte compositions. The speed of sound of pure EMC was within 1% of the value measured previously by Wang et al. [113]. Similar

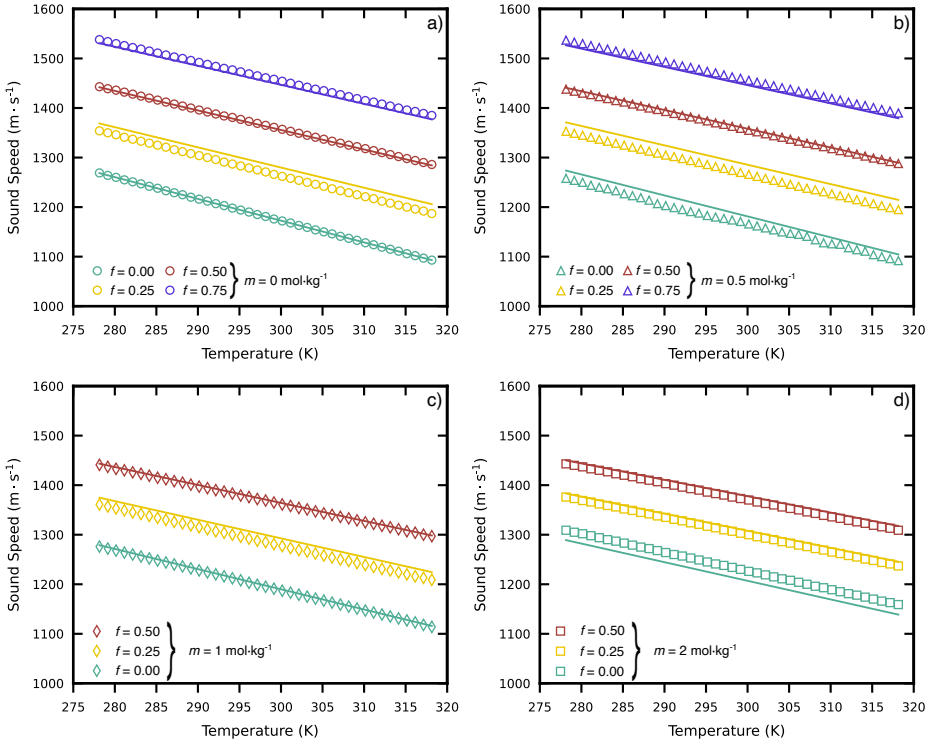

Figure 5.4: Speed of sound measurements for $LiPF_6$ in EC/EMC. For conciseness, only solutions with salt molalities $m = 0, 0.5, 1, 2$ and fraction EC $f = 0, 0.25, 0.5, 0.75$ are plotted. Tabular data for each of the tested electrolyte compositions are included in Appendix 5.A.5

to densities, sound velocities exhibit a strong linear relationship on temperature. Over the range of explored compositions, variations in ethylene carbonate content were observed to produce larger changes in sound velocity than variations in $LiPF_6$ concentration.

To simplify model implementation, a correlation was created relating m, f, and T to density and speed of sound. The Python PySRRegressor package [175] (a machine learning-based open-source tool for symbolic regression) was used to determine expressions for densities and speed of sound. The selected expression had the highest *score* among expressions with a least squares loss better than at least 1.5 times the most accurate model. The *score* was defined as the negative derivative of the log-loss with respect to complexity. The full list of optimized PySRRegressor parameters are outlined in Appendix 5.A.6. Before training the PySRRegressor models, each solution was first fit to a least squares regression line (LSRL). The slopes and y-intercepts from the LSRL were then used as the

training dataset for subsequent symbolic regression analyses. This method forced a linear relationship with respect to temperature. Upon finding the optimum symbolic expressions for density and speed of sound, the constants independent of m and f — A_0, B_0, C_0, and D_0 — were forced through the experimental data for pure EMC. The rest of the constants were then re-optimized by running a least squares curve fit to the experimental data.

The optimal correlation based on accuracy and parsimony for the densities of EMC:EC:$LiPF_6$ solutions was found to be

$$\rho = A(f, m) + B(f, m)T, \tag{5.6}$$

where the y-intercept A and slope B are related to the salt molalities m and weight fractions EC f through

$$A = A_0 + A_1 m + A_2 f + A_3 m f + A_4 m^2 \tag{5.7}$$

and

$$B = B_0 + B_1 f + B_2 f^4 m^2. \tag{5.8}$$

The coefficients are provided in Table 5.1. The linear fits have root mean squared percentage errors (RMSPEs) of less than 2% across the range of electrolyte compositions. The lower salt molalities of $m = 0$ and 0.5 are slightly more accurate with RMSPEs under 1%. The relative impacts of $LiPF_6$ concentration and EC weight fraction on the densities are seen in the magnitude of the A_1 (94.479) and A_2 (276.06) coefficients; within the composition ranges investigated, electrolyte density is more sensitive to changes in ethylene carbonate content than to changes in $LiPF_6$.

Upon conducting an identical symbolic regression analysis with the speed of sound measurements, the linear expression relating c to m, f, and T was

$$c = C(f, m) + D(f, m)T, \tag{5.9}$$

where the y-intercept C and slope D are expressed as

$$C = C_0 + C_1 m + \left(C_2 f + C_3 \sqrt{m}\right)^2 \tag{5.10}$$

Density, ρ		Speed of Sound, c	
Parameter	Value	Parameter	Value
A_0	1368.4	C_0	2489.5
A_1	94.479	C_1	-78.062
A_2	276.06	C_2	13.955
A_3	-29.056	C_3	-0.6238
A_4	-6.4893	D_0	-4.3895
B_0	-1.2118	D_1	0.3161
B_1	0.1313	D_2	0.6334
B_2	0.2865		

Table 5.1: Coefficients for symbolic regression fits for density and speed of sound.

and

$$D = D_0 + D_1 m + D_2 \sqrt{f}. \tag{5.11}$$

The speed of sound linear fits have RMSPEs of less than 2% for all tested electrolytes. In comparison to D_0, the magnitudes of D_1 and D_2 imply that neither the $LiPF_6$ molality nor EC weight fraction has a substantial impact on the slope of $c(T)$.

5.4.3 Isentropic bulk modulus

Characterizing the isentropic bulk modulus K_s can improve the understanding of the mechanical stiffness of the bulk solution [176]. This can, in turn, enable acoustic monitoring of the state of charge and state of health of Li-ion batteries by linking changes in sound velocity to composition- and degradation-induced variations in electrolyte density and compressibility [177–181]. The Newton–Laplace equation relates K_s to a solution's density and speed of sound through

$$K_s = c^2 \rho. \tag{5.12}$$

As with c and ρ, the isentropic bulk modulus is expected to vary with temperature and composition.

Fig. 5.5 depicts the bulk moduli for the EMC:EC:$LiPF_6$ composition space. The solid lines are obtained by using the correlations for ρ and c outlined in Eqs. 5.6 and 5.9, respectively, along with their relation to K_s through Eq. 5.12. The RMSPEs are under 1% in all instances. Furthermore, K_s appears mostly linear

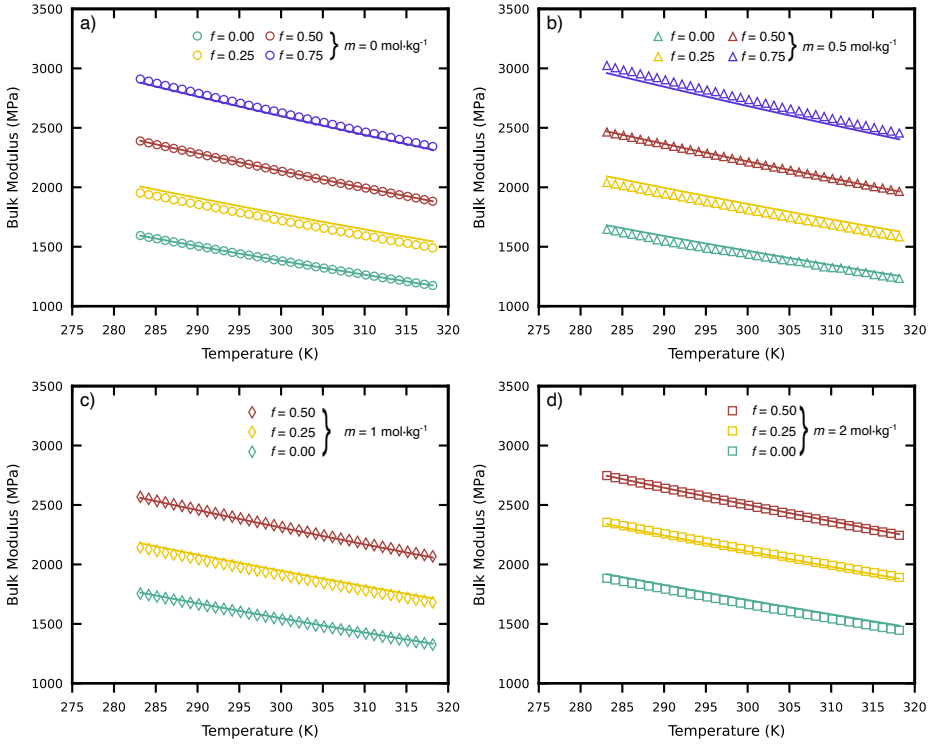

Figure 5.5: Plots of the isentropic bulk modulus K_s for $LiPF_6$ in EMC/EC. The solid lines are obtained by using the correlations for ρ and c outlined in Eqs. 5.6 and 5.9, respectively, along with their relation to K_s through Eq. 5.12. For conciseness, only solutions with salt molalities $m = 0, 0.5, 1, 2$ and fraction EC $f = 0, 0.25, 0.5, 0.75$ are plotted.

with respect to temperature, with slight deviations at higher temperatures. Within the examined composition ranges, variations in ethylene carbonate content produce larger changes in K_s than variations in $LiPF_6$ concentration. This is similar to trends seen with the EMC:PC cosolvent [113]. We hypothesize that both PC's and EC's rigid ring structures provide additional resistance to compression of the bulk electrolyte. In all instances, the bulk modulus varies between 1–3 GPa across the composition space tested in this study.

5.4.4 Coefficient of thermal expansion

As discussed in the introduction, the volumetric coefficient of thermal expansion α_V is required to simulate volume flow within an electrolyte when its temperature locally varies. One can rewrite Eq. 5.3 as

$$\alpha_V = -\frac{1}{\rho}\left(\frac{\partial \rho}{\partial T}\right)_p \tag{5.13}$$

which shows that α_V is proportional to the partial derivative of density with respect to temperature. As a result, α_V is fully determined by an electrolyte's density, its EC weight fraction, and $LiPF_6$ molality through Eq. 5.8, or

$$\alpha_V(m, f, T) = -\frac{1}{\rho(m, f, T)} \left(B_0 + B_1 f + B_2 f^4 m^2 \right), \tag{5.14}$$

where the coefficients B_0, B_1, and B_2 are provided in Table 5.1. Note that in this expression, only ρ depends on temperature, and it decreases with temperature. Thus, α_V for any electrolytic solution should generally decrease with increasing temperature. This trend is shown in Table 5.2, where the coefficient of thermal expansion decreases with respect to temperature across all the pure solvents.

5.4.5 Isothermal bulk modulus

Classical thermodynamic anslysis shows that the isothermal bulk modulus K_T of a fluid is a direct function of its isentropic bulk modulus K_s and thermal expansion modulus K_θ through

$$K_T = \left(\frac{1}{K_\theta} + \frac{1}{K_\mathrm{s}} \right)^{-1}, \tag{5.15}$$

in which K_θ is defined as

$$K_\theta = \frac{\rho \hat{C}_p}{T \alpha_V^2}, \tag{5.16}$$

where $\hat{C}_p$ represents the solution's specific isobaric heat capacity. Note that if $K_\theta >> K_\mathrm{s}$, the isothermal bulk modulus is well approximated by K_s, or $K_T \approx K_\mathrm{s}$. Alternatively, if $K_\mathrm{s} >> K_\theta$, K_T can be estimated by K_θ such that $K_T \approx K_\theta$. Knowledge of the magnitude of on the isentropic and thermal expansion moduli aids understanding the relative impact of each modulus.

In order to fully characterize K_T, specific heats are needed for each of the tested compositions. Experimental data for the $LiPF_6$:EMC:EC electrolyte do not appear to be available in the literature, but previous studies have reported $\hat{C}_p$ for common pure solvents. Table 5.2 summarizes these values. The thermal expansion moduli K_θ range between 4–10 GPa for the common solvents of EMC, EC, and PC across

Solvent	Temp. (K)	$\hat{C}_p$ $\left(\text{J mol}^{-1}\text{ K}^{-1}\right)$	ρ (kg m^{-3})	α_V $\left(\text{K}^{-1}\cdot 10^{-3}\right)$	K_θ (GPa)
EMC	283	179.2 [182]	1025.2	1.182	4.5
	300	182.8 [182]	1004.7	1.206	4.0
	318	186.7 [182]	982.8	1.233	3.6
EC	288	131.4 [182]	1343.0 [183]	0.826	10.2
	300	133.0 [182]	1329.7 [183]	0.835	9.6
	318	135.5 [182]	1309.7 [183]	0.848	8.8
PC	283	150.8 [182]	1216.1 [184]	0.944	7.1
	293	152.7 [182]	1204.6 [184]	0.953	6.8

Table 5.2: Thermal expansion modulus K_θ and volumetric coefficients of thermal expansion α_V for common pure solvents.

a temperature range of 283 K to 318 K. Addition of the $LiPF_6$ salt will likely cause the heat capacities to rise, however the close agreement of each cosolvent's volumetric heat capacity $\left(\rho\hat{C}_p\right)$ implies that they will retain a similar order of magnitude. Thus, it is safe to assume that K_θ for the ternary electrolyte ranges from 1–10 GPa. Comparison of K_θ to K_s reveals that they are of similar orders of magnitudes, as Fig. 5.5 shows that K_s range between 1–3 GPa for both the pure and ternary systems. This suggests that both moduli are of similar importance in defining the isothermal bulk modulus.

Similarities between the magnitudes of K_T and α_V reveal that pressure and temperature changes could counteract each other. For example, for pure EMC, $\alpha_V = 1.182 \cdot 10^{-3}$ K^{-1} and $1/K_T = 1.103 \cdot 10^{-3}$ MPa^{-1} at 300 K. Application of Eq. 5.2 reveals that the effects of a temperature increase of 1 K h^{-1} and a pressure increase of 1 MPa h^{-1} cancel each other, resulting in a negligible flux. In systems where batteries are thermally managed such that temperature variations are minimized, one could assume that pressure variations are dominating (i.e. NMC vs. Gr-SiOx cells). In any case, electrically driven flow in cylindrical and pouch cells may be accompanied by substantial pressure and temperature variations.

5.5 Conclusion

The ubiquitous cosolvent electrolyte of ethyl methyl carbonate (EMC) and ethylene carbonate (EC) was characterized to provide understanding how varying electrolyte composition and temperature affect electrolyte volume and bulk electrolyte flow.

The dynamic viscosity, density, and speed of sound were measured for 23 different ratios of EC mass fraction and $LiPF_6$ salt molality. A correlation was determined to relate the composition of the ternary system and its density and speed of sound. These correlations can be used to predict the isentropic bulk modulus K_s to a root mean squared percentage accuracy of 1%, in addition to its volumetric coefficient of thermal expansion α_V. The isentropic bulk moduli ranged between 1–3 GPa for all tested compositions, while the thermal expansion moduli is expected to range between 1–10 GPa. This implies that both are similarly relevant in determining the isothermal bulk modulus K_T which is required for modeling bulk electrolyte velocities with large pressure gradients. Finally, the isothermal bulk modulus was determined to be of similar orders of magnitude to α_V. Thus, this chapter provides the necessary parameters to model bulk electrolyte flow for the EMC:EC:$LiPF_6$ solvent system.

Although the $LiPF_6$ / EC–EMC system investigated here targets lithium-ion cells rather than flow batteries, several mechanistic insights translate directly to redox-flow contexts. First, both media are non-aqueous and feature rigid cyclic solutes—ethylene-carbonate in the Li-ion electrolyte and $V(acac)_3$ in the prototypical non-aqueous RFB studied in Chapters 2 and 3. In each case the rigid ring is solvated by more flexible linear carbonates, producing comparable local packing motifs. Consequently, trends of bulk moduli climbing as the ring-to-linear-solvent ratio rises should likewise govern the compressibility of $V(acac)_3$ electrolytes and, by extension, other non-aqueous RFB chemistries rich in rigid polar ligands. This cross-system consistency suggests that the acoustic/volumetric workflow demonstrated here can be applied towards RFB solvents and additives.

As an illustrative extreme, consider fast charging of Li-ion batteries which can experience temperature gradients approaching 60 K over 30 minutes [160], leading to dominant temperature-driven flux contributions. In contrast, in the absence of forced convection, liquid-phase pressure gradients are expected to remain well below the kPa-level drops typical of flow batteries [185], rendering pressure-driven effects secondary in fast-charge modeling.

That said, temperature-driven fluxes will play a more muted role in practical flow batteries than in static Li-ion cells. In situ X-ray studies of cylindrical Li-ion cells report temperature swings approaching 60°C, whereas well-engineered flow batteries rarely deviate by more than 5°C [186, 187]. While pressure gradients in the liquid phase of Li-ion cells have not been measured, flow batteries experience only kPa-level pressure drops [188–190] across a cell thanks to well-engineered flow fields and forced convection. Under these gentler gradients, thermo-mechanical diffusion terms become sub-dominant to convective transport, suggesting that the thermal expansion modulus K_θ and volumetric coefficients of thermal expansion α_V dependencies quantified here set conservative upper bounds for RFB systems. Despite the well-known economic limitations of aqueous vanadium electrolytes, extending the present protocol to VRFB systems could refine these inferences for a chemistry that already has large-scale commercial deployments.

5.A Appendices

5.A.1 Speed of sound calibration

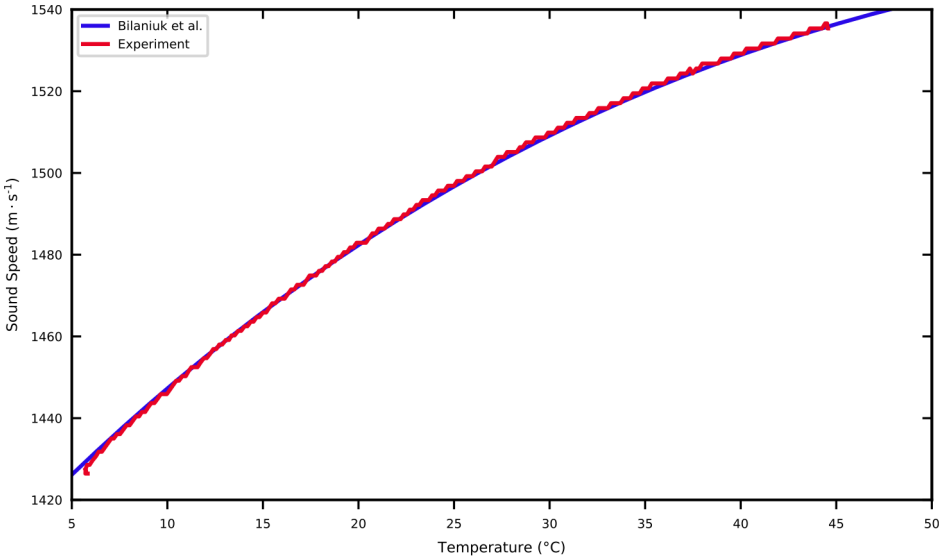

Figure 5.6: Calibration of the speed of sound experiments with ultrapure water. The length of the cuvette was altered to match data from literature [168, 169]. All measurements are within 0.2% of each other.

5.A.2 Experimental viscosity data

	$f = 0$						$f = 0.13$	$f = 0.2$	$f = 0.247$	$f = 0.25$		
Temp. (K)	$m = 0$	$m = 0.5$	$m = 0.75$	$m = 1$	$m = 1.25$	$m = 2$	$m = 0$	$m = 0.5$	$m = 0.75$	$m = 0$	$m = 0.5$	$m = 1$
281.15	0.910	1.363	1.812	–	3.303	5.853	–	–	–	1.250	–	3.756
282.15	0.901	1.351	1.798	–	3.230	5.702	–	–	–	1.233	–	3.722
283.15	0.885	1.320	1.746	2.206	3.075	5.534	0.925	0.984	1.047	1.214	2.011	3.633
284.15	0.874	1.296	1.710	2.161	3.004	5.388	0.918	0.971	1.031	1.194	1.986	3.552
285.15	0.862	1.258	1.678	2.106	2.936	5.227	0.903	0.955	1.015	1.175	1.946	3.460
286.15	0.849	1.246	1.646	2.062	2.867	5.095	0.888	0.946	0.999	1.156	1.906	3.376
287.15	0.837	1.223	1.612	2.015	2.797	4.972	0.872	0.927	0.983	1.138	1.866	3.296
288.15	0.825	1.206	1.582	1.973	2.733	4.827	0.859	0.913	0.968	1.119	1.830	3.218
289.15	0.814	1.180	1.553	1.935	2.676	4.701	0.846	0.898	0.952	1.102	1.791	3.145
290.15	0.804	1.167	1.524	1.895	2.620	4.587	0.832	0.883	0.938	1.085	1.756	3.071
291.15	0.795	1.148	1.497	1.859	2.559	4.482	0.822	0.871	0.924	1.068	1.724	2.998
292.15	0.784	1.134	1.470	1.823	2.505	4.369	0.810	0.859	0.910	1.051	1.690	2.936
293.15	0.773	1.108	1.443	1.790	2.454	4.272	0.799	0.846	0.897	1.035	1.657	2.862
294.15	0.764	1.083	1.419	1.757	2.404	4.160	0.788	0.834	0.883	1.019	1.624	2.804
295.15	0.754	1.084	1.395	1.724	2.353	4.053	0.776	0.822	0.869	1.005	1.597	2.744
296.15	0.745	1.061	1.370	1.694	2.306	3.963	0.765	0.810	0.857	0.989	1.564	2.684
297.15	0.734	1.040	1.348	1.665	2.263	3.864	0.755	0.799	0.845	0.975	1.536	2.628
298.15	0.724	1.028	1.326	1.634	2.218	3.784	0.746	0.788	0.834	0.962	1.508	2.574
299.15	0.716	1.000	1.305	1.606	2.173	3.697	0.737	0.777	0.822	0.947	1.483	2.518
300.15	0.707	0.995	1.284	1.579	2.136	3.618	0.727	0.767	0.810	0.935	1.456	2.467
301.15	0.699	0.977	1.263	1.551	2.093	3.531	0.718	0.757	0.800	0.922	1.428	2.419
302.15	0.690	0.963	1.242	1.525	2.059	3.457	0.707	0.747	0.789	0.910	1.405	2.371
303.15	0.681	0.951	1.222	1.499	2.020	3.382	0.699	0.736	0.779	0.897	1.379	2.328
304.15	0.673	0.949	1.214	1.473	1.986	3.308	0.690	0.726	0.768	0.886	1.354	2.286
305.15	0.666	0.923	1.185	1.450	1.951	3.240	0.681	0.716	0.757	0.873	1.335	2.240
306.15	0.659	0.905	1.166	1.426	1.918	3.173	0.672	0.708	0.748	0.861	1.309	2.192
307.15	0.650	0.905	1.148	1.404	1.885	3.105	0.665	0.699	0.739	0.851	1.285	2.158
308.15	0.642	0.899	1.130	1.379	1.850	3.044	0.656	0.691	0.730	0.839	1.265	2.120
309.15	0.635	0.878	1.112	1.356	1.816	2.986	0.648	0.682	0.720	0.829	1.243	2.082
310.15	0.628	0.859	1.095	1.334	1.784	2.927	0.641	0.674	0.711	0.818	1.223	2.047
311.15	0.620	0.844	1.078	1.314	1.753	2.869	0.633	0.666	0.702	0.807	1.203	2.010
312.15	0.614	0.830	1.062	1.291	1.722	2.816	0.626	0.657	0.694	0.798	1.185	1.976
313.15	0.608	0.829	1.046	1.271	1.694	2.759	0.618	0.649	0.686	0.788	1.167	1.942
314.15	0.601	0.818	1.031	1.249	1.666	2.710	0.611	0.641	0.677	0.778	1.151	1.908
315.15	0.594	0.805	1.016	1.229	1.642	2.656	0.605	0.634	0.669	0.768	1.134	1.878
316.15	0.588	0.796	1.002	1.208	1.614	2.602	0.599	0.627	0.661	0.759	1.115	1.844
317.15	0.582	0.786	0.987	1.175	1.586	2.554	0.591	0.620	0.653	0.750	1.099	1.811
318.15	0.577	0.776	0.973	1.155	1.566	2.503	0.586	0.613	0.645	0.742	1.081	1.786

Table 5.3: Dynamic viscosities (cP) for the EMC:EC:$LiPF_6$ electrolyte ($0 \leq f \leq 0.25$).

	$f = 0.25$	$f = 0.36$	$f = 0.47$	$f = 0.50$				$f = 0.60$	$f = 0.67$	$f = 0.70$	$f = 0.75$	
Temp. (K)	$m = 2$	$m = 0$	$m = 0$	$m = 0$	$m = 0.5$	$m = 1$	$m = 2$	$m = 0$	$m = 1.78$	$m = 0$	$m = 0$	$m = 0.5$
281.15	14.380	–	–	1.796	3.328	6.789	31.200	–	–	–	–	–
282.15	13.710	–	–	1.762	3.279	6.601	30.340	–	–	–	–	–
283.15	13.090	1.247	1.456	1.729	3.204	6.406	28.560	1.769	30.250	2.024	2.149	4.237
284.15	12.620	1.228	1.429	1.695	3.146	6.262	27.310	1.734	28.700	1.986	2.104	4.208
285.15	12.150	1.206	1.407	1.662	3.074	6.060	26.240	1.702	27.290	1.947	2.061	4.099
286.15	11.720	1.185	1.383	1.632	3.005	5.876	25.210	1.668	26.000	1.908	2.019	4.003
287.15	11.320	1.166	1.357	1.601	2.930	5.712	24.030	1.637	24.750	1.870	1.980	3.908
288.15	10.950	1.145	1.336	1.572	2.868	5.593	23.000	1.608	23.590	1.835	1.943	3.810
289.15	10.580	1.127	1.309	1.544	2.805	5.406	22.140	1.578	22.510	1.799	1.905	3.728
290.15	10.240	1.109	1.289	1.517	2.748	5.272	21.130	1.549	21.520	1.765	1.866	3.638
291.15	9.910	1.090	1.270	1.490	2.692	5.115	20.370	1.522	20.560	1.730	1.831	3.547
292.15	9.612	1.072	1.248	1.464	2.637	4.980	19.600	1.495	19.710	1.699	1.799	3.464
293.15	9.280	1.062	1.227	1.439	2.587	4.895	18.660	1.467	18.860	1.667	1.766	3.383
294.15	9.007	1.046	1.205	1.414	2.531	4.737	17.960	1.443	18.090	1.636	1.732	3.313
295.15	8.750	1.030	1.185	1.390	2.483	4.607	17.240	1.416	17.330	1.607	1.700	3.232
296.15	8.502	1.015	1.167	1.368	2.428	4.502	16.740	1.392	16.670	1.578	1.670	3.153
297.15	8.255	1.001	1.146	1.346	2.382	4.393	15.980	1.370	16.000	1.550	1.640	3.087
298.15	8.008	0.984	1.126	1.324	2.333	4.282	15.500	1.347	15.380	1.525	1.612	3.024
299.15	7.782	0.970	1.112	1.304	2.289	4.187	14.940	1.323	14.800	1.499	1.583	2.959
300.15	7.568	0.957	1.094	1.283	2.246	4.076	14.380	1.302	14.240	1.472	1.556	2.895
301.15	7.359	0.943	1.078	1.264	2.206	3.985	13.900	1.281	13.740	1.449	1.529	2.832
302.15	7.158	0.930	1.068	1.244	2.165	3.891	13.450	1.262	13.260	1.425	1.504	2.776
303.15	6.954	0.916	1.054	1.226	2.129	3.803	13.010	1.241	12.780	1.402	1.480	2.717
304.15	6.777	0.903	1.037	1.209	2.086	3.720	12.570	1.221	12.330	1.380	1.455	2.659
305.15	6.603	0.891	1.024	1.191	2.051	3.638	12.110	1.203	11.920	1.357	1.431	2.612
306.15	6.438	0.879	1.010	1.174	2.016	3.560	11.770	1.185	11.510	1.337	1.409	2.555
307.15	6.273	0.867	0.997	1.156	1.983	3.503	11.420	1.166	11.160	1.316	1.385	2.511
308.15	6.106	0.855	0.982	1.140	1.947	3.407	11.100	1.150	10.790	1.295	1.364	2.464
309.15	5.945	0.843	0.969	1.122	1.916	3.350	10.840	1.133	10.450	1.275	1.345	2.418
310.15	5.788	0.833	0.956	1.107	1.884	3.268	10.420	1.118	10.150	1.257	1.324	2.367
311.15	5.643	0.821	0.943	1.091	1.848	3.196	10.080	1.102	9.856	1.237	1.303	2.325
312.15	5.498	0.811	0.930	1.076	1.816	3.144	9.792	1.087	9.566	1.218	1.283	2.278
313.15	5.374	0.800	0.916	1.062	1.788	3.078	9.446	1.073	9.273	1.200	1.264	2.231
314.15	5.245	0.791	0.906	1.048	1.759	3.025	9.230	1.057	8.993	1.184	1.245	2.189
315.15	5.114	0.780	0.894	1.043	1.729	2.983	8.926	1.038	8.726	1.167	1.226	2.145
316.15	4.994	0.771	0.882	1.020	1.704	2.906	8.695	1.023	8.399	1.150	1.209	2.108
317.15	4.871	0.763	0.872	1.006	1.676	2.837	8.461	1.010	8.054	1.132	1.193	2.066
318.15	4.764	0.754	0.861	0.993	1.653	2.799	8.245	0.996	7.676	1.117	1.176	2.026

Table 5.4: Dynamic viscosities (cP) for the EMC:EC:$LiPF_6$ electrolyte ($0.25 \leq f \leq 0.75$).

5.A.3 Experimental density data

	$f = 0$						$f = 0.13$	$f = 0.2$	$f = 0.247$	$f = 0.25$		
Temp. (K)	$m = 0$	$m = 0.5$	$m = 0.75$	$m = 1$	$m = 1.25$	$m = 2$	$m = 0$	$m = 0.5$	$m = 0.75$	$m = 0$	$m = 0.5$	$m = 1$
281.15	1.0276	1.0781	1.1044	1.1327	1.1535	1.2057	–	–	–	1.1009	–	1.1923
282.15	1.0264	1.0771	1.1033	1.1315	1.1524	1.2046	–	–	–	1.0998	–	1.1911
283.15	1.0252	1.0760	1.1021	1.1303	1.1513	1.2034	1.0620	1.0835	1.0972	1.0986	1.149	1.1900
284.15	1.0240	1.0749	1.1009	1.1291	1.1501	1.2023	1.0608	1.0823	1.0960	1.0974	1.1479	1.1889
285.15	1.0228	1.0738	1.0998	1.1279	1.1490	1.2011	1.0597	1.0812	1.0949	1.0963	1.1468	1.1877
286.15	1.0216	1.0728	1.0986	1.1268	1.1478	1.2000	1.0585	1.0800	1.0937	1.0951	1.1456	1.1866
287.15	1.0204	1.0716	1.0974	1.1256	1.1466	1.1989	1.0573	1.0788	1.0926	1.0940	1.1445	1.1855
288.15	1.0192	1.0705	1.0963	1.1244	1.1455	1.1977	1.0561	1.0777	1.0914	1.0928	1.1434	1.1843
289.15	1.0180	1.0694	1.0951	1.1232	1.1444	1.1966	1.0550	1.0765	1.0902	1.0916	1.1422	1.1832
290.15	1.0168	1.0683	1.0939	1.1221	1.1432	1.1955	1.0538	1.0753	1.0891	1.0905	1.1411	1.1821
291.15	1.0156	1.0671	1.0928	1.1209	1.1420	1.1943	1.0526	1.0741	1.0879	1.0893	1.1400	1.1810
292.15	1.0144	1.0660	1.0916	1.1197	1.1409	1.1932	1.0514	1.0730	1.0867	1.0882	1.1388	1.1798
293.15	1.0132	1.0648	1.0904	1.1185	1.1397	1.1921	1.0502	1.0718	1.0856	1.0870	1.1377	1.1787
294.15	1.0120	1.0637	1.0893	1.1174	1.1386	1.1909	1.0491	1.0706	1.0844	1.0858	1.1365	1.1776
295.15	1.0107	1.0626	1.0881	1.1162	1.1374	1.1898	1.0479	1.0695	1.0832	1.0847	1.1354	1.1764
296.15	1.0095	1.0614	1.0869	1.1150	1.1363	1.1887	1.0467	1.0683	1.0821	1.0835	1.1343	1.1753
297.15	1.0083	1.0602	1.0858	1.1138	1.1351	1.1875	1.0455	1.0671	1.0809	1.0823	1.1331	1.1742
298.15	1.0071	1.0590	1.0846	1.1126	1.1340	1.1864	1.0443	1.0660	1.0798	1.0812	1.1320	1.1730
299.15	1.0059	1.0578	1.0834	1.1115	1.1328	1.1853	1.0431	1.0648	1.0786	1.0800	1.1308	1.1719
300.15	1.0047	1.0566	1.0822	1.1103	1.1317	1.1841	1.0420	1.0636	1.0774	1.0788	1.1297	1.1708
301.15	1.0035	1.0554	1.0811	1.1091	1.1305	1.1830	1.0408	1.0624	1.0763	1.0777	1.1285	1.1697
302.15	1.0023	1.0542	1.0799	1.1079	1.1294	1.1819	1.0396	1.0613	1.0751	1.0765	1.1274	1.1685
303.15	1.0011	1.0530	1.0787	1.1067	1.1282	1.1807	1.0384	1.0601	1.0739	1.0754	1.1262	1.1674
304.15	0.9999	1.0518	1.0776	1.1055	1.1271	1.1796	1.0372	1.0589	1.0728	1.0742	1.1251	1.1663
305.15	0.9986	1.0506	1.0764	1.1044	1.1260	1.1785	1.0360	1.0577	1.0716	1.0730	1.1239	1.1651
306.15	0.9974	1.0493	1.0752	1.1032	1.1248	1.1773	1.0349	1.0566	1.0704	1.0718	1.1227	1.1640
307.15	0.9962	1.0481	1.0740	1.1020	1.1237	1.1762	1.0337	1.0554	1.0693	1.0707	1.1215	1.1629
308.15	0.9950	1.0469	1.0729	1.1008	1.1225	1.1751	1.0325	1.0542	1.0681	1.0695	1.1204	1.1617
309.15	0.9938	1.0457	1.0717	1.0996	1.1214	1.1740	1.0313	1.0530	1.0669	1.0683	1.1192	1.1606
310.15	0.9926	1.0445	1.0705	1.0985	1.1202	1.1728	1.0301	1.0519	1.0657	1.0672	1.1180	1.1595
311.15	0.9913	1.0433	1.0693	1.0973	1.1191	1.1717	1.0289	1.0507	1.0646	1.0660	1.1168	1.1583
312.15	0.9901	1.0420	1.0682	1.0961	1.1179	1.1706	1.0277	1.0495	1.0634	1.0648	1.1156	1.1572
313.15	0.9889	1.0408	1.0670	1.0949	1.1168	1.1694	1.0265	1.0483	1.0622	1.0637	1.1144	1.1561
314.15	0.9877	1.0396	1.0658	1.0937	1.1156	1.1683	1.0253	1.0471	1.0611	1.0625	1.1132	1.1549
315.15	0.9865	1.0384	1.0646	1.0926	1.1145	1.1672	1.0241	1.0460	1.0599	1.0613	1.1120	1.1538
316.15	0.9852	1.0371	1.0634	1.0914	1.1133	1.1660	1.0229	1.0448	1.0587	1.0601	1.1108	1.1527
317.15	0.9840	1.0359	1.0623	1.0902	1.1122	1.1649	1.0217	1.0436	1.0576	1.0590	1.1096	1.1516
318.15	0.9828	1.0347	1.0611	1.0891	1.1110	1.1637	1.0205	1.0424	1.0564	1.0578	1.1084	1.1504

Table 5.5: Densities (kg/m^3) for the EMC:EC:$LiPF_6$ electrolyte ($0 \leq f \leq 0.25$).

	$f = 0.25$	$f = 0.36$	$f = 0.47$	$f = 0.50$				$f = 0.60$	$f = 0.67$	$f = 0.70$	$f = 0.75$	
Temp. (K)	$m = 2$	$m = 0$	$m = 0$	$m = 0$	$m = 0.5$	$m = 1$	$m = 2$	$m = 0$	$m = 1.78$	$m = 0$	$m = 0$	$m = 0.5$
281.15	1.2770	–	–	1.1806	1.2264	1.2705	1.3515	–	–	–	–	–
282.15	1.2759	–	–	1.1795	1.2253	1.2694	1.3503	–	–	–	–	–
283.15	1.2748	1.1321	1.1656	1.1783	1.2241	1.2682	1.3492	1.2091	1.3831	1.2435	1.2612	1.3106
284.15	1.2737	1.1310	1.1645	1.1772	1.2230	1.2671	1.3481	1.2080	1.3817	1.2424	1.2601	1.3095
285.15	1.2726	1.1298	1.1634	1.1760	1.2219	1.2660	1.3470	1.2069	1.3798	1.2413	1.2589	1.3083
286.15	1.2715	1.1287	1.1622	1.1749	1.2207	1.2649	1.3459	1.2057	1.3778	1.2401	1.2578	1.3072
287.15	1.2703	1.1275	1.1611	1.1738	1.2196	1.2637	1.3448	1.2046	1.3757	1.2390	1.2567	1.3061
288.15	1.2692	1.1264	1.1599	1.1726	1.2185	1.2626	1.3437	1.2034	1.3745	1.2379	1.2555	1.3050
289.15	1.2681	1.1252	1.1588	1.1715	1.2174	1.2615	1.3426	1.2023	1.3744	1.2367	1.2544	1.3039
290.15	1.2670	1.1240	1.1576	1.1703	1.2162	1.2604	1.3414	1.2011	1.3718	1.2356	1.2532	1.3028
291.15	1.2659	1.1229	1.1565	1.1692	1.2151	1.2593	1.3403	1.2000	1.3718	1.2344	1.2521	1.3016
292.15	1.2648	1.1217	1.1554	1.1680	1.2140	1.2582	1.3392	1.1989	1.3712	1.2333	1.2509	1.3005
293.15	1.2637	1.1206	1.1542	1.1669	1.2129	1.2570	1.3381	1.1977	1.3696	1.2322	1.2498	1.2994
294.15	1.2625	1.1194	1.1531	1.1657	1.2117	1.2559	1.3370	1.1966	1.3683	1.2310	1.2487	1.2983
295.15	1.2614	1.1183	1.1519	1.1646	1.2106	1.2548	1.3359	1.1954	1.3671	1.2299	1.2475	1.2972
296.15	1.2603	1.1171	1.1508	1.1635	1.2095	1.2537	1.3348	1.1943	1.3658	1.2287	1.2464	1.2960
297.15	1.2592	1.1160	1.1496	1.1623	1.2084	1.2526	1.3337	1.1932	1.3647	1.2276	1.2453	1.2949
298.15	1.2581	1.1148	1.1485	1.1612	1.2072	1.2515	1.3326	1.1920	1.3635	1.2265	1.2441	1.2938
299.15	1.2570	1.1137	1.1473	1.1600	1.2061	1.2504	1.3315	1.1909	1.3624	1.2253	1.2430	1.2927
300.15	1.2559	1.1125	1.1462	1.1589	1.2050	1.2493	1.3304	1.1897	1.3613	1.2242	1.2418	1.2915
301.15	1.2548	1.1114	1.1450	1.1577	1.2039	1.2481	1.3293	1.1886	1.3602	1.2230	1.2407	1.2904
302.15	1.2537	1.1102	1.1439	1.1566	1.2028	1.2470	1.3282	1.1875	1.3591	1.2219	1.2396	1.2893
303.15	1.2526	1.1091	1.1428	1.1555	1.2016	1.2459	1.3270	1.1863	1.3580	1.2208	1.2384	1.2882
304.15	1.2514	1.1079	1.1416	1.1543	1.2005	1.2448	1.3259	1.1852	1.3571	1.2196	1.2373	1.2871
305.15	1.2503	1.1068	1.1405	1.1532	1.1994	1.2437	1.3248	1.1841	1.3574	1.2185	1.2362	1.2859
306.15	1.2492	1.1056	1.1393	1.1520	1.1983	1.2426	1.3237	1.1829	1.3571	1.2174	1.2350	1.2848
307.15	1.2481	1.1044	1.1382	1.1509	1.1971	1.2415	1.3226	1.1818	1.3566	1.2162	1.2339	1.2837
308.15	1.2470	1.1033	1.1370	1.1497	1.1960	1.2404	1.3215	1.1806	1.3556	1.2151	1.2327	1.2826
309.15	1.2459	1.1021	1.1359	1.1486	1.1949	1.2393	1.3204	1.1795	1.3546	1.2140	1.2316	1.2815
310.15	1.2448	1.1010	1.1347	1.1474	1.1938	1.2382	1.3193	1.1784	1.3537	1.2128	1.2305	1.2804
311.15	1.2437	1.0998	1.1336	1.1463	1.1927	1.2371	1.3182	1.1772	1.3526	1.2117	1.2293	1.2792
312.15	1.2426	1.0987	1.1324	1.1451	1.1915	1.2360	1.3171	1.1761	1.3515	1.2105	1.2282	1.2781
313.15	1.2415	1.0975	1.1313	1.1440	1.1904	1.2348	1.3160	1.1749	1.3523	1.2094	1.2271	1.2770
314.15	1.2404	1.0964	1.1301	1.1429	1.1893	1.2337	1.3149	1.1738	1.3523	1.2083	1.2259	1.2759
315.15	1.2393	1.0952	1.1290	1.1417	1.1882	1.2326	1.3138	1.1727	1.3516	1.2071	1.2248	1.2747
316.15	1.2382	1.0940	1.1278	1.1406	1.1870	1.2315	1.3127	1.1715	1.3514	1.2060	1.2237	1.2736
317.15	1.2371	1.0929	1.1267	1.1394	1.1859	1.2304	1.3116	1.1704	1.3507	1.2049	1.2225	1.2725
318.15	1.2360	1.0917	1.1256	1.1383	1.1848	1.2293	1.3104	1.1693	1.3497	1.2037	1.2214	1.2714

Table 5.6: Densities (kg/m^3) for the EMC:EC:$LiPF_6$ electrolyte ($0.25 \leq f \leq 0.75$).

5.A.4 Comparison of density data with literature

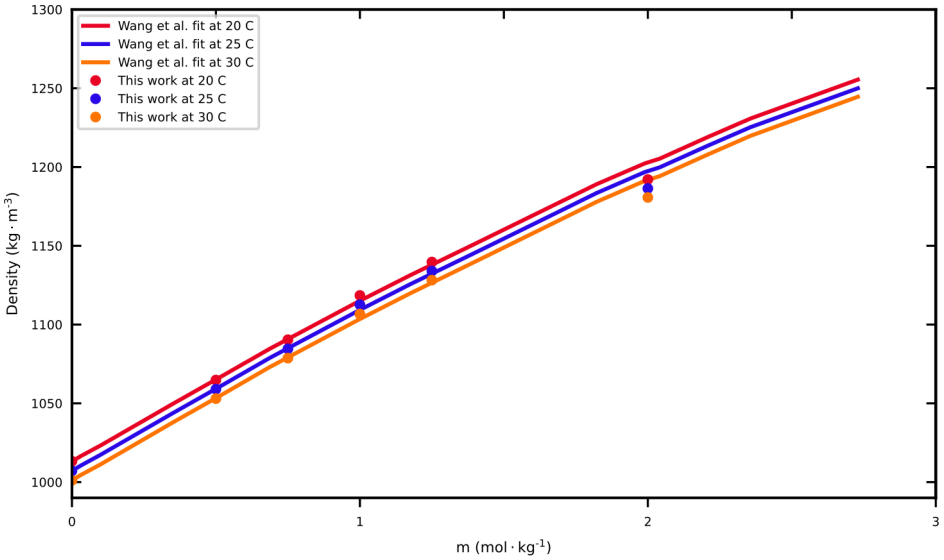

Figure 5.7: Comparison of density data for the binary $LiPF_6$:EMC electrolytes with Wang et al. at 20°C, 25°C, and 30°C [174]. All measurements are within 1.2% of each other.

5.A.5 Experimental speed of sound data

	$f = 0$						$f = 0.13$	$f = 0.2$	$f = 0.247$		$f = 0.25$	
Temp. (K)	$m = 0$	$m = 0.5$	$m = 0.75$	$m = 1$	$m = 1.25$	$m = 2$	$m = 0$	$m = 0.5$	$m = 0.75$	$m = 0$	$m = 0.5$	$m = 1$
278.15	1269	1258	1283	1276	1299	1309	1308	1332	1349	1354	1353	1361
279.15	1264	1254	1279	1272	1295	1305	1304	1328	1345	1350	1349	1357
280.15	1260	1250	1274	1268	1291	1302	1300	1324	1341	1346	1345	1353
281.15	1255	1244	1270	1264	1287	1298	1296	1320	1337	1341	1341	1349
282.15	1251	1240	1266	1260	1283	1294	1291	1316	1333	1337	1337	1345
283.15	1247	1237	1262	1256	1279	1290	1287	1312	1329	1333	1333	1342
284.15	1242	1233	1258	1252	1275	1287	1283	1308	1325	1329	1329	1338
285.15	1238	1227	1254	1248	1271	1283	1279	1304	1321	1325	1325	1334
286.15	1233	1223	1250	1244	1267	1279	1275	1300	1316	1321	1321	1330
287.15	1229	1219	1246	1240	1264	1275	1271	1296	1312	1316	1317	1326
288.15	1225	1214	1241	1236	1260	1272	1266	1292	1308	1312	1313	1323
289.15	1220	1207	1237	1232	1256	1268	1262	1288	1304	1308	1309	1319
290.15	1216	1203	1233	1228	1252	1264	1258	1283	1300	1304	1305	1315
291.15	1212	1199	1229	1224	1248	1260	1254	1279	1296	1300	1302	1311
292.15	1207	1195	1225	1220	1244	1257	1250	1275	1292	1296	1298	1307
293.15	1203	1191	1221	1216	1240	1253	1246	1271	1288	1291	1294	1304
294.15	1198	1188	1217	1212	1236	1249	1242	1267	1284	1287	1290	1300
295.15	1194	1183	1213	1208	1232	1245	1237	1263	1280	1283	1286	1296
296.15	1190	1180	1208	1203	1228	1241	1233	1259	1276	1279	1282	1292
297.15	1185	1177	1204	1199	1224	1238	1229	1255	1272	1275	1278	1288
298.15	1181	1174	1200	1195	1220	1234	1225	1251	1268	1271	1274	1285
299.15	1176	1171	1196	1191	1216	1230	1221	1247	1264	1266	1270	1281
300.15	1172	1166	1192	1187	1212	1226	1217	1243	1260	1262	1266	1277
301.15	1168	1162	1188	1183	1208	1223	1212	1239	1256	1258	1262	1273
302.15	1163	1158	1184	1179	1204	1219	1208	1235	1252	1254	1258	1269
303.15	1159	1154	1180	1175	1200	1215	1204	1230	1248	1250	1254	1266
304.15	1154	1150	1175	1171	1197	1211	1200	1226	1244	1246	1250	1262
305.15	1150	1147	1171	1167	1193	1208	1196	1222	1240	1242	1246	1258
306.15	1146	1145	1167	1163	1189	1204	1192	1218	1235	1237	1242	1254
307.15	1141	1141	1163	1159	1185	1200	1188	1214	1231	1233	1238	1250
308.15	1137	1134	1159	1155	1181	1196	1183	1210	1227	1229	1235	1247
309.15	1133	1128	1155	1151	1177	1193	1179	1206	1223	1225	1231	1243
310.15	1128	1126	1151	1147	1173	1189	1175	1202	1219	1221	1227	1239
311.15	1124	1125	1147	1143	1169	1185	1171	1198	1215	1217	1223	1235
312.15	1119	1118	1142	1139	1165	1181	1167	1194	1211	1212	1219	1231
313.15	1115	1114	1138	1135	1161	1178	1163	1190	1207	1208	1215	1228
314.15	1111	1111	1134	1131	1157	1174	1158	1186	1203	1204	1211	1224
315.15	1106	1104	1130	1127	1153	1170	1154	1181	1199	1200	1207	1220
316.15	1102	1100	1126	1123	1149	1166	1150	1177	1195	1196	1203	1216
317.15	1097	1096	1122	1118	1145	1163	1146	1173	1191	1192	1199	1213
318.15	1093	1092	1118	1114	1141	1159	1142	1169	1187	1187	1195	1209

Table 5.7: Sound speeds (m/s) through the EMC:EC:$LiPF_6$ electrolyte ($0 \leq f \leq 0.25$).

	$f = 0.25$	$f = 0.36$	$f = 0.47$	$f = 0.50$				$f = 0.60$	$f = 0.67$	$f = 0.70$	$f = 0.75$	
Temp. (K)	$m = 2$	$m = 0$	$m = 0$	$m = 0$	$m = 0.5$	$m = 1$	$m = 2$	$m = 0$	$m = 1.78$	$m = 0$	$m = 0$	$m = 0.5$
278.15	1376	1388	1427	1443	1438	1441	1443	1480	1500	1521	1538	1537
279.15	1373	1384	1423	1439	1434	1437	1440	1476	1496	1517	1534	1533
280.15	1369	1380	1419	1436	1430	1433	1437	1473	1493	1513	1530	1530
281.15	1366	1376	1415	1432	1427	1430	1433	1469	1490	1509	1526	1526
282.15	1362	1372	1411	1428	1423	1426	1430	1465	1486	1505	1522	1522
283.15	1359	1368	1407	1424	1419	1423	1427	1461	1483	1502	1519	1519
284.15	1356	1364	1403	1420	1415	1419	1423	1457	1480	1498	1515	1515
285.15	1352	1360	1399	1416	1412	1415	1420	1453	1476	1494	1511	1511
286.15	1349	1356	1395	1412	1408	1412	1417	1449	1473	1490	1507	1508
287.15	1345	1352	1392	1408	1404	1408	1413	1445	1470	1486	1503	1504
288.15	1342	1349	1388	1404	1400	1405	1410	1441	1466	1482	1500	1500
289.15	1338	1345	1384	1400	1397	1401	1407	1437	1463	1478	1496	1497
290.15	1335	1341	1380	1396	1393	1397	1403	1433	1460	1475	1492	1493
291.15	1331	1337	1376	1392	1389	1394	1400	1430	1456	1471	1488	1489
292.15	1328	1333	1372	1388	1385	1390	1396	1426	1453	1467	1484	1485
293.15	1324	1329	1368	1384	1382	1387	1393	1422	1450	1463	1480	1482
294.15	1321	1325	1364	1381	1378	1383	1390	1418	1446	1459	1477	1478
295.15	1317	1321	1360	1377	1374	1379	1386	1414	1443	1455	1473	1474
296.15	1314	1317	1356	1373	1370	1376	1383	1410	1440	1452	1469	1471
297.15	1310	1313	1352	1369	1367	1372	1380	1406	1436	1448	1465	1467
298.15	1307	1309	1348	1365	1363	1369	1376	1402	1433	1444	1461	1463
299.15	1303	1305	1344	1361	1359	1365	1373	1398	1430	1440	1458	1460
300.15	1300	1301	1340	1357	1355	1361	1370	1394	1426	1436	1454	1456
301.15	1296	1297	1336	1353	1352	1358	1366	1390	1423	1432	1450	1452
302.15	1293	1293	1332	1349	1348	1354	1363	1387	1420	1428	1446	1449
303.15	1290	1289	1329	1345	1344	1351	1360	1383	1416	1425	1442	1445
304.15	1286	1285	1325	1341	1341	1347	1356	1379	1413	1421	1438	1441
305.15	1283	1281	1321	1337	1337	1343	1353	1375	1410	1417	1435	1438
306.15	1279	1277	1317	1333	1333	1340	1350	1371	1406	1413	1431	1434
307.15	1276	1274	1313	1329	1329	1336	1346	1367	1403	1409	1427	1430
308.15	1272	1270	1309	1325	1326	1333	1343	1363	1400	1405	1423	1427
309.15	1269	1266	1305	1322	1322	1329	1339	1359	1396	1402	1419	1423
310.15	1265	1262	1301	1318	1318	1325	1336	1355	1393	1398	1415	1419
311.15	1262	1258	1297	1314	1314	1322	1333	1351	1390	1394	1412	1416
312.15	1258	1254	1293	1310	1311	1318	1329	1347	1386	1390	1408	1412
313.15	1255	1250	1289	1306	1307	1315	1326	1343	1383	1386	1404	1408
314.15	1251	1246	1285	1302	1303	1311	1323	1340	1380	1382	1400	1405
315.15	1248	1242	1281	1298	1299	1307	1319	1336	1376	1378	1396	1401
316.15	1244	1238	1277	1294	1296	1304	1316	1332	1373	1375	1393	1397
317.15	1241	1234	1273	1290	1292	1300	1313	1328	1370	1371	1389	1394
318.15	1237	1230	1269	1286	1288	1297	1309	1324	1366	1367	1385	1390

Table 5.8: Sound speeds (m/s) through the EMC:EC:$LiPF_6$ electrolyte ($0.25 \leq f \leq 0.75$).

5.A.6 PySRRegressor parameters

PySR Parameter	Value
Populations	30
Binary Operators	$+$,$-$, $\times$
Unary Operators	Square, cube, square root, logarithm
Number of iterations	120
Population size	60
Number of cycles per iteration	50
Maximum size	20
Maximum depth	60
Complexity of constants	0.5
Complexity of variables	1

Table 5.9: Parameter settings for PySRRegressor during symbolic regression of speed of sound and density.

6
Conclusions

This dissertation set out to unravel the coupled chemical, transport, and mechanical phenomena that presently constrain the performance and durability of non-aqueous redox-flow batteries (NARFBs). Although each chapter addresses a distinct scale—from cell level operation to molecular interactions—their collective narrative is intentionally circuitous: the work begins by motivating long-duration storage on modern grids, follows the fate of membranes during extended cycling, constructs a rigorous theoretical framework to quantify motion under realistic concentrations, and finally supplies the material constants that anchor theory to practice. The present chapter synthesises the primary findings across that trajectory, paying particular attention to the theoretical and data-centric advances articulated in the prior two chapters and explaining how they knit together with the earlier mechanistic studies.

The empirical core of the thesis, presented in Chapters 2 and 3, demonstrated that separator fouling—not electrolyte degradation—is the dominant mode of capacity fade in the $V(acac)_3$/$TEABF_4$ electrolyte. By carefully isolating the separator from the electrolyte and showing that capacity recovers when a fresh membrane is installed, those chapters shifted the focus from chemical stability to transport and reactor design. Yet this re-orientation raised an immediate question: how can one predict, quantitatively, how multicomponent electrolytes will evolve under the

steep concentration, potential, and pressure gradients encountered in practical flow cells? Chapters 4 and 5 provide a foundation to respond to this challenge.

Chapter 4 reconceptualises multicomponent transport through a salt–charge transformation of the Onsager–Stefan–Maxwell (OSM) equations. By projecting the fluxes into electroneutral and net-charge subspaces, the reformulation achieves two ends. First, it provides a coherent hierarchy of models—from the classical Nernst–Planck equation at one extreme to the complete OSM formalism at the other—together with transparent criteria for selecting the level of complexity warranted by a particular operating regime. Second, the salt–charge basis deconvolutes chemical-electrical entanglements so that the electrical contribution stands alone in the Gibbs-free-energy expression. A robust electroneutral reference state is developed which does not give particular charged species special roles. This insight has immediate practical value: it enables modelers to trace apparent deviations from electroneutrality back to specific entries of the electroneutral Darken matrix.

The predictive power of any theory, however elegant, rests on the fidelity of its constitutive inputs. Chapter 5 therefore undertakes a comprehensive characterisation of the thermo-mechanical properties of $LiPF_6$ in EC/EMC mixed carbonates, measuring viscosity, density, acoustic velocity, and both isothermal and isentropic bulk moduli across temperature and composition windows typical of contemporary battery operation. Although $LiPF_6$ electrolytes differ chemically from the $V(acac)_3$ systems explored in the earlier chapters, they share a critical structural similarity: both rely on rigid-ring solutes dissolved in comparatively flexible linear co-solvents. This parallelism suggest that volume-of-mixing functions, partial-molar compressibilities, and analogous second derivatives of the Gibbs free energy exhibit trends that are not limited to individual chemistries. By providing closed-form correlations for these properties, Chapter 5 makes the OSM framework in the salt–charge basis of Chapter 4 executable under varying pressure and temperature.

The interplay between Chapters 4 and 5 thus completes a methodological loop that began with the mechanistic diagnostics of Chapters 2 and 3. The experimental discovery that fouling accelerates whenever large ionic-strength and

potential gradients are imposed across the separator is now able to be practically modeled using concentrated solution theory with only a limited number of transport coefficients with the relations derived in Chapter 4, while the constitutive data of Chapter 5 allows for the extension under nonisothermal and nonisobaric conditions. A practical implication follows: separator durability cannot be evaluated by steady-state permeability tests performed at a single concentration, nor can it be predicted by models that assume ideal mixing. Instead, one must resolve space- and time-dependent gradients of both concentration and electrostatic potential, feed them through the full OSM framework, and monitor the resulting ionic fluxes.

Several limitations remain. Although the salt–charge methodology is formally general, its empirical validation has so far been confined to a single class of lithium electrolytes. Extending the property measurements to acetonitrile-based organometallic systems would tighten the link between theory and the specific RFB chemistry studied in Chapters 2 and 3. Moreover, the membrane characterisation relied primarily on ex-situ imaging and electrochemical proxies; operando neutron or X-ray tomography could provide real-time visualisation of pore occupancy, directly correlating structural changes with transport degradation. Finally, the techno-economic implications of the dynamic fouling model—particularly the trade-off between separator cost and lifetime—have been only sketched in outline. Embedding the coupled transport and fouling equations into a cost-optimisation framework represents a practical next step toward technology-neutral decision making.

Notwithstanding these caveats, the work presented in this thesis ames to reshape several common assumptions made by the flow-battery research community. It shows that the lifetime of an RFB is governed as much by how the electrolyte is moved, balanced, and pressurised as by the intrinsic chemical stability of its redox couples. It supplies a theoretical language, complete with empirically grounded coefficients, to quantify those coupled influences. Lastly, it demonstrates that apparently disparate design choices such as separator porosity, flow-field geometry, reservoir sizing, and state-of-charge protocol can be evaluated on a single energetic and economic footing once representative transport descriptors are in place.

Taken as a whole, this dissertation argues for an integrative view of electrochemical-energy-storage research—one that treats materials science, transport theory, and system engineering as mutually reinforcing rather than sequential endeavours. By doing so, it shortens the feedback loop between laboratory discovery and profitable product design. In the broader context of grid decarbonisation, such integration is essential: only when theory, data, and device co-evolve can long-duration storage progress from an academic aspiration to an industrial reality capable of undergirding a resilient, low-carbon energy infrastructure.

References

[1] Sanya Carley et al. 'Empirical evaluation of the stringency and design of renewable portfolio standards'. In: *Nature Energy* 3.9 (Sept. 2018), pp. 754–763. DOI: 10.1038/s41560-018-0202-4.

[2] *Renewable Capacity Statistics 2024*. Tech. rep. Abu Dhabi: International Renewable Energy Agency, Mar. 2024. URL: https://www.irena.org/-/media/Files/IRENA/Agency/Publication/2024/Mar/IRENA_RE_Capacity_Statistics_2024.pdf.

[3] Pravin P. Varaiya, Felix F. Wu and Janusz W. Bialek. 'Smart Operation of Smart Grid: Risk-Limiting Dispatch'. In: *Proceedings of the IEEE* 99.1 (2011), pp. 40–57. DOI: 10.1109/JPROC.2010.2080250.

[4] *Pathways to Commercial Liftoff: Long Duration Energy Storage*. Tech. rep. U.S. Department of Energy, Mar. 2023. URL: https://liftoff.energy.gov.

[5] Anya Castillo and Dennice F. Gayme. 'Grid-scale energy storage applications in renewable energy integration: A survey'. In: *Energy Conversion and Management* 87 (2014), pp. 885–894. DOI: 10.1016/j.enconman.2014.07.063.

[6] Omar J. Guerra et al. 'The value of seasonal energy storage technologies for the integration of wind and solar power'. In: *Energy and Environmental Science* 13.7 (July 2020), pp. 1909–1922. DOI: 10.1039/d0ee00771d.

[7] Paul Denholm et al. *The Role of Energy Storage with Renewable Electricity Generation*. Tech. rep. National Renewable Energy Laboratory, 2010. URL: http://www.osti.gov/bridge.

[8] *Net load data flexible capacity needs*. 2025. URL: https://www.caiso.com/library/net-load-data-flexible-capacity-needs.

[9] Xing Luo et al. 'Overview of current development in electrical energy storage technologies and the application potential in power system operation'. In: *Applied Energy* 137 (2015), pp. 511–536. DOI: 10.1016/j.apenergy.2014.09.081.

[10] Noah Kittner et al. 'Grid-scale energy storage'. In: *Technological Learning in the Transition to a Low-Carbon Energy System: Conceptual Issues, Empirical Findings, and Use, in Energy Modeling*. Elsevier, Jan. 2019, pp. 119–143. DOI: 10.1016/B978-0-12-818762-3.00008-X.

[11] Wei Wang et al. 'Recent progress in redox flow battery research and development'. In: *Advanced Functional Materials* 23.8 (Feb. 2013), pp. 970–986. DOI: 10.1002/adfm.201200694.

[12] David Wenzhong Gao. 'Basic Concepts and Control Architecture of Microgrids'. In: *Energy Storage for Sustainable Microgrid*. Elsevier, 2015, pp. 1–34. DOI: 10.1016/B978-0-12-803374-6.00001-9.

[13] Sina Orangi et al. 'Historical and prospective lithium-ion battery cost trajectories from a bottom-up production modeling perspective'. In: *Journal of Energy Storage* 76 (Jan. 2024). DOI: 10.1016/j.est.2023.109800.

[14] *Long Duration Storage Shot*. URL: https://www.energy.gov/topics/long-duration-storage-shot?nrg_redirect=471280.

[15] Julio Romel Martinez-Bolanos et al. 'Economic feasibility of battery energy storage systems for replacing peak power plants for commercial consumers under energy time of use tariffs'. In: *Journal of Energy Storage* 29 (June 2020). DOI: 10.1016/j.est.2020.101373.

[16] Yifeng Li et al. 'Long term performance evaluation of a commercial vanadium flow battery system'. In: *Journal of Energy Storage* 90 (June 2024), p. 111790. DOI: 10.1016/j.est.2024.111790.

[17] *Case Study: Energy Superhub Oxford*. URL: https://invinity.com/energy-superhub-oxford/.

[18] Walther Kangro. *Method for storing electrical energy*. 1949.

[19] Lawrence Thaller. 'Electrically rechargeable redox flow cells'. In: *Intersoc. Energy Conversion Eng. Conf.* 1974: NASA.

[20] M. Skyllas-Kazacos et al. 'New All-Vanadium Redox Flow Cell'. In: *Journal of The Electrochemical Society* 133.5 (May 1986), pp. 1057–1058. DOI: 10.1149/1.2108706.

[21] Maria Skyllas-Kazacos et al. 'Characteristics and performance of 1 kW UNSW vanadium redox battery'. In: *Journal of Power Sources* 35.4 (Sept. 1991), pp. 399–404. DOI: 10.1016/0378-7753(91)80058-6.

[22] Xiao-Zi Yuan et al. 'A review of all-vanadium redox flow battery durability: Degradation mechanisms and mitigation strategies'. In: *International Journal of Energy Research* (June 2019), er.4607. DOI: 10.1002/er.4607.

[23] Mani Ulaganathan et al. 'Recent Advancements in All-Vanadium Redox Flow Batteries'. In: *Advanced Materials Interfaces* 3.1 (Jan. 2016). DOI: 10.1002/admi.201500309.

[24] John Kaldellis. *Stand-Alone and Hybrid Wind Energy Systems*. Woodhead Publishing, 2010.

[25] Kara E. Rodby et al. 'Assessing the levelized cost of vanadium redox flow batteries with capacity fade and rebalancing'. In: *Journal of Power Sources* 460 (June 2020), p. 227958. DOI: 10.1016/j.jpowsour.2020.227958.

[26] Christine Minke and Thomas Turek. 'Materials, system designs and modelling approaches in techno-economic assessment of all-vanadium redox flow batteries – A review'. In: *Journal of Power Sources* 376 (Feb. 2018), pp. 66–81. DOI: 10.1016/j.jpowsour.2017.11.058.

[27] Jens Noack et al. 'Techno-Economic Modeling and Analysis of Redox Flow Battery Systems'. In: *Energies* 9.8 (Aug. 2016), p. 627. DOI: 10.3390/en9080627.

[28] Jingyu Xi et al. 'Broad temperature adaptability of vanadium redox flow battery—Part 2: Cell research'. In: *Electrochimica Acta* 191 (Feb. 2016), pp. 695–704. DOI: 10.1016/j.electacta.2016.01.165.

[29] Adam Z. Weber et al. 'Redox flow batteries: A review'. In: *Journal of Applied Electrochemistry* 41.10 (2011), pp. 1137–1164. DOI: 10.1007/s10800-011-0348-2.

[30] Jens Noack et al. 'The Chemistry of Redox-Flow Batteries'. In: *Angewandte Chemie International Edition* 54.34 (Aug. 2015), pp. 9776–9809. DOI: 10.1002/anie.201410823.

[31] Feng Pan and Qing Wang. 'Redox Species of Redox Flow Batteries: A Review'. In: *Molecules* 20.11 (Nov. 2015), pp. 20499–20517. DOI: 10.3390/molecules201119711.

[32] M. Skyllas-Kazacos et al. 'Progress in Flow Battery Research and Development'. In: *Journal of The Electrochemical Society* 158.8 (2011), R55. DOI: 10.1149/1.3599565.

[33] P. Leung et al. 'Recent developments in organic redox flow batteries: A critical review'. In: *Journal of Power Sources* 360 (Aug. 2017), pp. 243–283. DOI: 10.1016/j.jpowsour.2017.05.057.

[34] Gareth Kear, Akeel A. Shah and Frank C. Walsh. 'Development of the all-vanadium redox flow battery for energy storage: a review of technological, financial and policy aspects'. In: *International Journal of Energy Research* 36.11 (Sept. 2012), pp. 1105–1120. DOI: 10.1002/er.1863.

[35] Jeffrey A Kowalski et al. 'Recent advances in molecular engineering of redox active organic molecules for nonaqueous flow batteries'. In: *Current Opinion in Chemical Engineering* 13 (Aug. 2016), pp. 45–52. DOI: 10.1016/j.coche.2016.08.002.

[36] Yan Huang et al. 'Nonaqueous redox-flow batteries: features, challenges, and prospects'. In: *Current Opinion in Chemical Engineering* 8 (May 2015), pp. 105–113. DOI: 10.1016/j.coche.2015.04.001.

[37] Robert M. Darling et al. 'Pathways to low-cost electrochemical energy storage: a comparison of aqueous and nonaqueous flow batteries'. In: *Energy Environ. Sci.* 7.11 (Sept. 2014), pp. 3459–3477. DOI: 10.1039/C4EE02158D.

[38] Shikha Sharma et al. 'Iron-iminopyridine complexes as charge carriers for non-aqueous redox flow battery applications'. In: *Energy Storage Materials* 37 (May 2021), pp. 576–586. DOI: 10.1016/j.ensm.2021.01.035.

[39] Y. Matsuda et al. 'A rechargeable redox battery utilizing ruthenium complexes with non-aqueous organic electrolyte'. In: *Journal of Applied Electrochemistry* 18.6 (Nov. 1988), pp. 909–914. DOI: 10.1007/BF01016050.

[40] M.H. Chakrabarti, R.A.W. Dryfe and E.P.L. Roberts. 'Evaluation of electrolytes for redox flow battery applications'. In: *Electrochimica Acta* 52.5 (Jan. 2007), pp. 2189–2195. DOI: 10.1016/j.electacta.2006.08.052.

[41] Zhen Li et al. 'Electrochemical Properties of an All-Organic Redox Flow Battery Using 2,2,6,6-Tetramethyl-1-Piperidinyloxy and N-Methylphthalimide'. In: *Electrochemical and Solid-State Letters* 14.12 (2011), A171. DOI: 10.1149/2.012112esl.

[42] Sri R. Narayan et al. 'Next-generation aqueous flow battery chemistries'. In: *Current Opinion in Electrochemistry* 18 (Dec. 2019), pp. 72–80. DOI: 10.1016/j.coelec.2019.10.010.

[43] Yahua Liu et al. 'Degradation of electrochemical active compounds in aqueous organic redox flow batteries'. In: *Current Opinion in Electrochemistry* 32 (Apr. 2022), p. 100895. DOI: 10.1016/j.coelec.2021.100895.

[44] Bo Yang et al. 'An Inexpensive Aqueous Flow Battery for Large-Scale Electrical Energy Storage Based on Water-Soluble Organic Redox Couples'. In: *Journal of The Electrochemical Society* 161.9 (June 2014), A1371–A1380. DOI: 10.1149/2.1001409jes.

[45] Yuhao Lu, John B. Goodenough and Youngsik Kim. 'Aqueous Cathode for Next-Generation Alkali-Ion Batteries'. In: *Journal of the American Chemical Society* 133.15 (Apr. 2011), pp. 5756–5759. DOI: 10.1021/ja201118f.

[46] Zhicheng Xu et al. 'Review of zinc dendrite formation in zinc bromine redox flow battery'. In: *Renewable and Sustainable Energy Reviews* 127 (July 2020), p. 109838. DOI: 10.1016/j.rser.2020.109838.

[47] Mihai Duduta et al. 'Semi-Solid Lithium Rechargeable Flow Battery'. In: *Advanced Energy Materials* 1.4 (July 2011), pp. 511–516. DOI: 10.1002/aenm.201100152.

[48] Xiao Wang, Jingchao Chai and Jianbing "Jimmy" Jiang. 'Redox flow batteries based on insoluble redox-active materials. A review'. In: *Nano Materials Science* 3.1 (Mar. 2021), pp. 17–24. DOI: 10.1016/j.nanoms.2020.06.003.

[49] Dong Kyu Kim et al. 'Parametric study and flow rate optimization of all-vanadium redox flow batteries'. In: *Applied Energy* 228 (Oct. 2018), pp. 891–901. DOI: 10.1016/j.apenergy.2018.06.094.

[50] Sandip Maurya et al. 'Effect of flow field geometry on operating current density, capacity and performance of vanadium redox flow battery'. In: *Journal of Power Sources* 404 (Nov. 2018), pp. 20–27. DOI: 10.1016/j.jpowsour.2018.09.093.

[51] Adolf Fick. 'Ueber Diffusion'. In: *Annalen der Physik* 170.1 (Jan. 1855), pp. 59–86. DOI: 10.1002/andp.18551700105.

[52] Adolph Fick. 'On liquid diffusion'. In: *The London, Edinburgh, and Dublin Philosophical Magazine and Journal of Science* 10.63 (July 1855), pp. 30–39. DOI: 10.1080/14786445508641925.

[53] Thomas Graham. 'On the diffusion of liquids'. In: *Philosophical Transactions of the Royal Society of London* 140 (Dec. 1850), pp. 1–46. DOI: 10.1098/rstl.1850.0001.

[54] Tad W. Patzek. 'Fick's Diffusion Experiments Revisited — Part I'. In: *Advances in Historical Studies* 03.04 (2014), pp. 194–206. DOI: 10.4236/ahs.2014.34017.

[55] Tad W. Patzek. 'Fick's Diffusion Experiments Revisited — Part II'. In: *Advances in Historical Studies* 03.04 (2014), pp. 207–220. DOI: 10.4236/ahs.2014.34018.

[56] Max Planck. 'Ueber die Erregung von Electricität und Wärme in Electrolyten'. In: *Annalen der Physik* 275.2 (Jan. 1890), pp. 161–186. DOI: 10.1002/andp.18902750202.

[57] Max Planck. 'Ueber die Potentialdifferenz zwischen zwei verdünnten Lösungen binärer Electrolyte'. In: *Annalen der Physik* 276.8 (Jan. 1890), pp. 561–576. DOI: 10.1002/andp.18902760802.

[58] John Newman and K.E. Thomas-Alyea. *Electrochemical Systems*. 3rd ed. New Jersey: John Wiley & Sons, Inc., 2004.

[59] Adrien M. Bizeray, David A. Howey and Charles W. Monroe. 'Resolving a Discrepancy in Diffusion Potentials, with a Case Study for Li-Ion Batteries'. In: *Journal of The Electrochemical Society* 163.8 (May 2016), E223–E229. DOI: 10.1149/2.0451608jes.

[60] Lars Ole Valoen and Jan N. Reimers. 'Transport Properties of LiPF6-Based Li-Ion Battery Electrolytes'. In: *Journal of The Electrochemical Society* 152.5 (2005), A882. DOI: 10.1149/1.1872737.

[61] Athinthra Krishnaswamy Sethurajan et al. 'Accurate Characterization of Ion Transport Properties in Binary Symmetric Electrolytes Using In Situ NMR Imaging and Inverse Modeling'. In: *The Journal of Physical Chemistry B* 119.37 (Sept. 2015), pp. 12238–12248. DOI: 10.1021/acs.jpcb.5b04300.

[62] Josef Stefan. 'Über das Gleichgewicht und die Bewegung, insbesondere die Diffusion von Gasgemengen'. In: *Sitzungsberichte der Akademie der Wissenschaften, mathematisch-naturwissenschaftliche Klasse* 63 (1871).

[63] Kara D. Fong et al. 'Transport phenomena in electrolyte solutions: Nonequilibrium thermodynamics and statistical mechanics'. In: *AIChE Journal* 66.12 (Dec. 2020). DOI: 10.1002/aic.17091.

[64] Alexander Van-Brunt, Patrick E. Farrell and Charles W. Monroe. 'Structural electroneutrality in Onsager–Stefan–Maxwell transport with charged species'. In: *Electrochimica Acta* 441 (Feb. 2023). DOI: 10.1016/j.electacta.2022.141769.

[65] Brian A. Pethica. 'Are electrostatic potentials between regions of different chemical composition measurable? The Gibbs–Guggenheim principle reconsidered, extended and its consequences revisited'. In: *Physical Chemistry Chemical Physics* 9.47 (2007), p. 6253. DOI: 10.1039/b706153f.

[66] Qinghua Liu et al. 'Non-aqueous vanadium acetylacetonate electrolyte for redox flow batteries'. In: *Electrochemistry Communications* 11.12 (Dec. 2009), pp. 2312–2315. DOI: 10.1016/j.elecom.2009.10.006.

[67] Aaron A. Shinkle et al. 'Degradation mechanisms in the non-aqueous vanadium acetylacetonate redox flow battery'. In: *Journal of Power Sources* 206 (May 2012), pp. 490–496. DOI: 10.1016/j.jpowsour.2010.12.096.

[68] Aaron A. Shinkle et al. 'Electrode kinetics in non-aqueous vanadium acetylacetonate redox flow batteries'. In: *Journal of Applied Electrochemistry* 41.10 (Oct. 2011), pp. 1191–1199. DOI: 10.1007/s10800-011-0314-z.

[69] James D. Saraidaridis and Charles W. Monroe. 'Nonaqueous vanadium disproportionation flow batteries with porous separators cycle stably and tolerate high current density'. In: *Journal of Power Sources* 412 (Feb. 2019), pp. 384–390. DOI: 10.1016/j.jpowsour.2018.11.058.

[70] Ismailia L. Escalante-García et al. 'Performance of a Non-Aqueous Vanadium Acetylacetonate Prototype Redox Flow Battery: Examination of Separators and Capacity Decay'. In: *Journal of The Electrochemical Society* 162.3 (2015), A363–A372. DOI: 10.1149/2.0471503jes.

[71] Charlotte Clegg and Ian G. Hill. 'Characterizing Degradation in Non-aqueous Vanadium(III) Acetylacetonate Redox Flow Batteries'. In: *Journal of The Electrochemical Society* 167.12 (Aug. 2020), p. 120510. DOI: 10.1149/1945-7111/aba932.

[72] Michelle L. Lehmann et al. 'Membrane design for non-aqueous redox flow batteries: Current status and path forward'. In: *Chem* 8.6 (June 2022), pp. 1611–1636. DOI: 10.1016/j.chempr.2022.04.005.

[73] Kirk P. Smith and Charles W. Monroe. 'Image-Based Mechanical Balancing of Reservoir Volumes During Benchtop Flow Battery Operation'. In: *Frontiers in Chemical Engineering* 3 (Oct. 2021). DOI: 10.3389/fceng.2021.748865.

[74] R Rungta. *Data and Code for "Drivers of membrane fouling in the vanadium acetylacetonate flow battery"*. 2023. DOI: 10.5287/ora-rbe2g7ebb. URL: https://ora.ox.ac.uk/objects/uuid:d56ac0e3-c629-4ae3-a5a9-9d220efbedc1.

[75] Kirk Smith. 'Symmetric Nonaqueous Flow Batteries with Porous Separators'. PhD thesis. Oxford: University of Oxford, 2021.

[76] Pedro Ascencio et al. 'Adaptive Observer for Charge-State and Crossover Estimation in Disproportionation Redox Flow Batteries undergoing Self-Discharge'. In: *American Control Conference* (2019).

[77] Jiashu Yuan et al. 'Membranes in non-aqueous redox flow battery: A review'. In: *Journal of Power Sources* 500 (May 2021). DOI: 10.1016/j.jpowsour.2021.229983.

[78] Craig A. MacHado et al. 'Redox Flow Battery Membranes: Improving Battery Performance by Leveraging Structure-Property Relationships'. In: *ACS Energy Letters* 6.1 (Jan. 2021), pp. 158–176. DOI: 10.1021/acsenergylett.0c02205.

[79] Lin Qiao et al. 'A Composite Membrane with High Stability and Low Cost Specifically for Iron–Chromium Flow Battery'. In: *Polymers* 14.11 (May 2022), p. 2245. DOI: 10.3390/polym14112245.

[80] Toby Wong et al. 'Sulfonated poly(ether-ether-ketone) membranes with intrinsic microporosity enable efficient redox flow batteries for energy storage'. In: *Joule* 9.2 (Feb. 2025), p. 101795. DOI: 10.1016/j.joule.2024.11.012. URL: https://linkinghub.elsevier.com/retrieve/pii/S2542435124005099.

[81] Ke Gong et al. 'Nonaqueous redox-flow batteries: Organic solvents, supporting electrolytes, and redox pairs'. In: *Energy and Environmental Science* 8.12 (Dec. 2015), pp. 3515–3530. DOI: 10.1039/c5ee02341f.

[82] Rohit Rungta, Kirk P. Smith and Charles W. Monroe. 'Drivers of membrane fouling in the vanadium acetylacetonate flow battery'. In: *Journal of Membrane Science Letters* 4.1 (June 2024). DOI: 10.1016/j.memlet.2024.100074.

[83] Tao Liu et al. 'Two-dimensional vermiculite nanosheets-modified porous membrane for non-aqueous redox flow batteries'. In: *Journal of Power Sources* 500 (July 2021). DOI: 10.1016/j.jpowsour.2021.229987.

[84] Jae Hun Kim et al. 'Fabrication of a composite anion exchange membrane with aligned ion channels for a high-performance non-aqueous vanadium redox flow battery'. In: *RSC Advances* 10.9 (2020), pp. 5010–5025. DOI: 10.1039/c9ra08616a.

[85] Kirk P. Smith et al. 'Multi-Week Cycling of a Nonaqueous Flow Battery Using Tris-Bipyridine Iron (II) Triflate without Additional Supporting Electrolyte'. In: *Journal of The Electrochemical Society* 170.6 (June 2023), p. 060510. DOI: 10.1149/1945-7111/acd873.

[86] James R. Welty, Gregory L. Rorrer and David G. Foster. *Fundamentals of Momentum, Heat, and Mass Transfer*. 6th ed. John Wiley & Sons, Inc, 2015.

[87] Thomas Williams and Rohit Rungta. *RFB Pump Controller*. Mar. 2025. URL: https://github.com/Concrete-Slab/RFB-Pump-Controller.

[88] Jacob Houser et al. 'Architecture for improved mass transport and system performance in redox flow batteries'. In: *Journal of Power Sources* 351 (2017), pp. 96–105. DOI: 10.1016/j.jpowsour.2017.03.083.

[89] John Newman, Douglas Bennion and Charles W. Tobias. 'Mass Transfer in Concentrated Binary Electrolytes'. In: *Berichte der Bunsengesellschaft für physikalische Chemie* 69.7 (Sept. 1965), pp. 608–612. DOI: 10.1002/bbpc.19650690712.

[90] Marc Doyle, Thomas F. Fuller and John Newman. 'Modeling of Galvanostatic Charge and Discharge of the Lithium/Polymer/Insertion Cell'. In: *Journal of The Electrochemical Society* 140.6 (June 1993), pp. 1526–1533. DOI: 10.1149/1.2221597.

[91] Marc Doyle et al. 'Comparison of Modeling Predictions with Experimental Data from Plastic Lithium Ion Cells'. In: *Journal of The Electrochemical Society* 143.6 (June 1996), pp. 1890–1903. DOI: 10.1149/1.1836921.

[92] John Newman. 'Stefan–Maxwell mass transport'. In: *Chemical Engineering Science* 64.22 (Nov. 2009), pp. 4796–4803. DOI: 10.1016/j.ces.2009.07.002.

[93] James Maxwell. 'IV. On the dynamical theory of gases'. In: *Philosophical Transactions of the Royal Society of London* 157 (Dec. 1867), pp. 49–88. DOI: 10.1098/rstl.1867.0004.

[94] E. N. Lightfoot, E. L. Cussler and R. L. Rettig. 'Applicability of the Stefan-Maxwell equations to multicomponent diffusion in liquids'. In: *AIChE Journal* 8.5 (Nov. 1962), pp. 708–710. DOI: 10.1002/aic.690080530.

[95] Lars Onsager. 'THEORIES AND PROBLEMS OF LIQUID DIFFUSION'. In: *Annals of the New York Academy of Sciences* 46.5 (Nov. 1945), pp. 241–265. DOI: 10.1111/j.1749-6632.1945.tb36170.x.

[96] Lars Onsager. *The Collected Works of Lars Onsager*. Ed. by P.C. Hemmer, H. Holden and S. Kjelstrup Ratkje. Vol. 17. Trondheim: World Scientific Publishing Co., 1996.

[97] Barun Kumar Chakrabarti et al. 'Modelling of redox flow battery electrode processes at a range of length scales: a review'. In: *Sustainable Energy & Fuels* 4.11 (2020), pp. 5433–5468. DOI: 10.1039/D0SE00667J.

[98] Andrew R. Crothers et al. 'Theory of Multicomponent Phenomena in Cation-Exchange Membranes: Part III. Transport in Vanadium Redox-Flow-Battery Separators'. In: *Journal of The Electrochemical Society* 167.1 (Jan. 2020), p. 013549. DOI: 10.1149/1945-7111/ab6725.

[99] Taeho Jung, Andrew A. Wang and Charles W. Monroe. 'Overpotential from Cosolvent Imbalance in Battery Electrolytes: LiPF6 in EMC:EC'. In: *ACS Omega* 8.23 (June 2023), pp. 21133–21144. DOI: 10.1021/acsomega.3c02088.

[100] Andrew A. Wang et al. 'Potentiometric MRI of a Superconcentrated Lithium Electrolyte: Testing the Irreversible Thermodynamics Approach'. In: *ACS Energy Letters* 6.9 (Sept. 2021), pp. 3086–3095. DOI: 10.1021/acsenergylett.1c01213.

[101] Charles W. Monroe, Dean R. Wheeler and John Newman. 'Nonequilibrium linear response theory: Application to Onsager-Stefan-Maxwell diffusion'. In: *Industrial and Engineering Chemistry Research* 54.16 (Apr. 2015), pp. 4460–4467. DOI: 10.1021/ie503875c.

[102] J. Willard Gibbs and John Tyndall. *On the equilibrium of heterogeneous substances*. [New Haven: Published by the Academy, 1874. DOI: 10.5479/sil.421748.39088007099781.

[103] Gilbert Lewis and Merle Randall. *Thermodynamics and the Free Energy of Chemical Substances*. New York and London: McGraw-Hill Book Company, Inc., 1923. DOI: 10.1002/ange.19250380811.

[104] E. A. Guggenheim. 'The Conceptions of Electrical Potential Difference between Two Phases and the Individual Activities of Ions'. In: *The Journal of Physical Chemistry* 33.6 (June 1929), pp. 842–849. DOI: 10.1021/j150300a003.

[105] Alexander Van-Brunt, Patrick E. Farrell and Charles W. Monroe. 'Consolidated theory of fluid thermodiffusion'. In: *AIChE Journal* 68.5 (May 2022). DOI: 10.1002/aic.17599.

[106] Jing Liu and Charles W. Monroe. 'Solute-volume effects in electrolyte transport'. In: *Electrochimica Acta* 135 (July 2014), pp. 447–460. DOI: 10.1016/j.electacta.2014.05.009.

[107] Priyamvada Goyal and Charles W. Monroe. 'New Foundations of Newman's Theory for Solid Electrolytes: Thermodynamics and Transient Balances'. In: *Journal of The Electrochemical Society* 164.11 (2017), E3647–E3660. DOI: 10.1149/2.0611711jes.

[108] Francis R A Aznaran et al. 'Finite element methods for multicomponent convection-diffusion'. In: *IMA Journal of Numerical Analysis* 45.1 (Feb. 2025), pp. 188–222. DOI: 10.1093/imanum/drae001.

[109] John Newman. 'The polarized diffuse double layer'. In: *Transactions of the Faraday Society* 61 (1965), p. 2229. DOI: 10.1039/tf9656102229.

[110] John Newman and Thomas W. Chapman. 'Restricted diffusion in binary solutions'. In: *AIChE Journal* 19.2 (1973), pp. 343–348. DOI: 10.1002/aic.690190220.

[111] Ronald F. Probstein. *Physicochemical Hydrodynamics*. Wiley, July 1994. DOI: 10.1002/0471725137.

[112] Kang Xu. 'Nonaqueous Liquid Electrolytes for Lithium-Based Rechargeable Batteries'. In: *Chemical Reviews* 104.10 (Oct. 2004), pp. 4303–4418. DOI: 10.1021/cr030203g.

[113] Andrew A. Wang et al. 'Compressibility of Lithium Hexafluorophosphate Solutions in Two Carbonate Solvents'. In: *Journal of Chemical and Engineering Data* 68.4 (Apr. 2023), pp. 805–812. DOI: 10.1021/acs.jced.2c00711.

[114] Jing Liu and Charles W. Monroe. 'On the characterization of battery electrolytes with polarization cells'. In: *Electrochimica Acta* 167 (June 2015), pp. 357–363. DOI: 10.1016/j.electacta.2015.03.104.

[115] Peter N. Pintauro and Douglas N. Bennion. 'Mass transport of electrolytes in membranes. 1. Development of mathematical transport model'. In: *Industrial & Engineering Chemistry Fundamentals* 23.2 (May 1984), pp. 230–234. DOI: 10.1021/i100014a016.

[116] Thomas F. Fuller and John Newman. 'Experimental Determination of the Transport Number of Water in Nafion 117 Membrane'. In: *Journal of The Electrochemical Society* 139.5 (May 1992), pp. 1332–1337. DOI: 10.1149/1.2069407.

[117] Francesco Fornasiero, John M. Prausnitz and Clayton J. Radke. 'Multicomponent Diffusion in Highly Asymmetric Systems. An Extended Maxwell Stefan Model for Starkly Different Sized, Segment Accessible Chain Molecules'. In: *Macromolecules* 38.4 (Feb. 2005), pp. 1364–1370. DOI: 10.1021/ma040133v.

[118] Ali Salehi et al. 'A unified multicomponent stress-diffusion model of drug release from non-biodegradable polymeric matrix tablets'. In: *Journal of Controlled Release* 224 (Feb. 2016), pp. 43–58. DOI: 10.1016/j.jconrel.2015.12.045.

[119] Masao Doi. *Introduction to Polymer Physics*. Tokyo: Iwanami Shoten, 1992.

[120] Tianhong Hou and Charles W. Monroe. 'Composition-dependent thermodynamic and mass-transport characterization of lithium hexafluorophosphate in propylene carbonate'. In: *Electrochimica Acta* 332 (Feb. 2020). DOI: 10.1016/j.electacta.2019.135085.

[121] Pablo G. Debenedetti. 'Fluctuation-based computer calculation of partial molar properties. I. Molecular dynamics simulation of constant volume fluctuations'. In: *The Journal of Chemical Physics* 86.12 (June 1987), pp. 7126–7137. DOI: 10.1063/1.452362.

[122] Alexander Findlay. 'The Phase Rule and Its Applications'. In: *Journal of Chemical Education* 5.4 (Apr. 1928), p. 499. DOI: 10.1021/ed005p499.1.

[123] H. B. G. Casimir. 'On Onsager's Principle of Microscopic Reversibility'. In: *Reviews of Modern Physics* 17.2-3 (Apr. 1945), pp. 343–350. DOI: 10.1103/RevModPhys.17.343.

[124] Eugene Helfand. 'On Inversion of the Linear Laws of Irreversible Thermodynamics'. In: *The Journal of Chemical Physics* 33.2 (Aug. 1960), pp. 319–322. DOI: 10.1063/1.1731144.

[125] Charles W. Monroe and John Newman. 'Onsager reciprocal relations for Stefan-Maxwell diffusion'. In: *Industrial and Engineering Chemistry Research* 45.15 (July 2006), pp. 5361–5367. DOI: 10.1021/ie051061e.

[126] Priyamvada Goyal and Charles W. Monroe. 'Thermodynamic factors for locally non-neutral, concentrated electrolytic fluids'. In: *Electrochimica Acta* 371 (Mar. 2021). DOI: 10.1016/j.electacta.2020.137638.

[127] Yang Zhao et al. 'Standard partial molar volumes of some electrolytes in ethylene carbonate based mixtures'. In: *The Journal of Chemical Thermodynamics* 36.1 (Jan. 2004), pp. 1–6. DOI: 10.1016/j.jct.2003.09.005.

[128] H. J. Merk. 'The macroscopic equations for simultaneous heat and mass transfer in isotropic, continuous and closed systems'. In: *Applied Scientific Research* 8.1 (1959), pp. 73–99. DOI: 10.1007/BF00411741.

[129] Charles W. Monroe and John Newman. 'Onsager's shortcut to proper forces and fluxes'. In: *Chemical Engineering Science* 64.22 (Nov. 2009), pp. 4804–4809. DOI: 10.1016/j.ces.2009.05.009.

[130] K. E. Bett, J. S. Rowlinson and G. Saville. *Thermodynamics for Chemical Engineers*. The MIT Press, Mar. 2003. DOI: 10.7551/mitpress/6793.001.0001.

[131] Dean R. Wheeler and John Newman. 'Molecular Dynamics Simulations of Multicomponent Diffusion. 1. Equilibrium Method'. In: *The Journal of Physical Chemistry B* 108.47 (Nov. 2004), pp. 18353–18361. DOI: 10.1021/jp047850b.

[132] Dean R. Wheeler and John Newman. 'Molecular Dynamics Simulations of Multicomponent Diffusion. 2. Nonequilibrium Method'. In: *The Journal of Physical Chemistry B* 108.47 (Nov. 2004), pp. 18362–18367. DOI: 10.1021/jp047849c.

[133] Kara D. Fong et al. 'Ion Correlations and Their Impact on Transport in Polymer-Based Electrolytes'. In: *Macromolecules* 54.6 (Mar. 2021), pp. 2575–2591. DOI: 10.1021/acs.macromol.0c02545.

[134] Helen K. Bergstrom and Bryan D. McCloskey. 'Ion Transport in (Localized) High Concentration Electrolytes for Li-Based Batteries'. In: *ACS Energy Letters* 9.2 (Feb. 2024), pp. 373–380. DOI: 10.1021/acsenergylett.3c01662.

[135] Thomas W Chapman and J F Newman. 'A COMPILATION OF SELECTED THERMODYNAMIC AND TRANSPORT PROPERTIES OP BINARY ELECTROLYTES IN AQUEOUS SOLUTION'. In: 1968. URL: https://api.semanticscholar.org/CorpusID:93489730.

[136] Gabriel M. Silva, Xiaodong Liang and Georgios M. Kontogeorgis. 'Investigation of the Limits of the Linearized Poisson–Boltzmann Equation'. In: *The Journal of Physical Chemistry B* 126.22 (June 2022), pp. 4112–4131. DOI: 10.1021/acs.jpcb.2c02758.

[137] E.A. Guggenheim. *Thermodynamics - An advanced treatment for chemists and physicists*. 8th ed. North-Holland Publishing Co, Aug. 1988.

[138] Zhejun Li et al. 'A high-energy and low-cost polysulfide/iodide redox flow battery'. In: *Nano Energy* 30 (Dec. 2016), pp. 283–292. DOI: 10.1016/j.nanoen.2016.09.043.

[139] Jan Winsberg et al. 'Redox-Flow Batteries: From Metals to Organic Redox-Active Materials'. In: *Angewandte Chemie International Edition* 56.3 (Jan. 2017), pp. 686–711. DOI: 10.1002/anie.201604925.

[140] Dion Hubble et al. 'Liquid electrolyte development for low-temperature lithium-ion batteries'. In: *Energy & Environmental Science* 15.2 (2022), pp. 550–578. DOI: 10.1039/D1EE01789F.

[141] T. Richard Jow et al. *Electrolytes for Lithium and Lithium-Ion Batteries*. Vol. 58. New York, NY: Springer New York, 2014. DOI: 10.1007/978-1-4939-0302-3.

[142] E.R. Logan and J.R. Dahn. 'Electrolyte Design for Fast-Charging Li-Ion Batteries'. In: *Trends in Chemistry* 2.4 (Apr. 2020), pp. 354–366. DOI: 10.1016/j.trechm.2020.01.011.

[143] Joe C. Stallard et al. 'Mechanical properties of cathode materials for lithium-ion batteries'. In: *Joule* 6.5 (May 2022), pp. 984–1007. DOI: 10.1016/j.joule.2022.04.001.

[144] Joshua Lamb and Christopher J. Orendorff. 'Evaluation of mechanical abuse techniques in lithium ion batteries'. In: *Journal of Power Sources* 247 (Feb. 2014), pp. 189–196. DOI: 10.1016/j.jpowsour.2013.08.066.

[145] Julian Kalhoff et al. 'Safer electrolytes for lithium-ion batteries: State of the art and perspectives'. In: *ChemSusChem* 8.13 (July 2015), pp. 2154–2175. DOI: 10.1002/cssc.201500284.

[146] Long Chen et al. 'Toward wide-temperature electrolyte for lithium–ion batteries'. In: *Battery Energy* 1.2 (Apr. 2022). DOI: 10.1002/bte2.20210006.

[147] Qiuyan Li et al. 'Wide-Temperature Electrolytes for Lithium-Ion Batteries'. In: *ACS Applied Materials and Interfaces* 9.22 (June 2017), pp. 18826–18835. DOI: 10.1021/acsami.7b04099.

[148] E.J. Plichta and W.K. Behl. 'A low-temperature electrolyte for lithium and lithium-ion batteries'. In: *Journal of Power Sources* 88.2 (June 2000), pp. 192–196. DOI: 10.1016/S0378-7753(00)00367-0.

[149] Michael S. Ding et al. 'Liquid/Solid Phase Diagrams of Binary Carbonates for Lithium Batteries Part II'. In: *Journal of The Electrochemical Society* 148.4 (2001), A299. DOI: 10.1149/1.1353568.

[150] David S. Hall, Julian Self and J. R. Dahn. 'Dielectric Constants for Quantum Chemistry and Li-Ion Batteries: Solvent Blends of Ethylene Carbonate and Ethyl Methyl Carbonate'. In: *Journal of Physical Chemistry C* 119.39 (Sept. 2015), pp. 22322–22330. DOI: 10.1021/acs.jpcc.5b06022.

[151] Mengyun Nie et al. 'Lithium ion battery graphite solid electrolyte interphase revealed by microscopy and spectroscopy'. In: *Journal of Physical Chemistry* 117.3 (Jan. 2013), pp. 1257–1267. DOI: 10.1021/jp3118055.

[152] Kang Xu et al. 'Graphite/electrolyte interface formed in LiBOB-based electrolytes I. Differentiating the roles of EC and LiBOB in SEI formation'. In: *Electrochemical and Solid-State Letters* 7.9 (2004). DOI: 10.1149/1.1774973.

[153] E. R. Logan et al. 'A Study of the Physical Properties of Li-Ion Battery Electrolytes Containing Esters'. In: *Journal of The Electrochemical Society* 165.2 (2018), A21–A30. DOI: 10.1149/2.0271802jes.

[154] L. F. Xiao et al. 'Optimization of EC-based multi-solvent electrolytes for low temperature applications of lithium-ion batteries'. In: *Electrochimica Acta* 49.27 (Oct. 2004), pp. 4857–4863. DOI: 10.1016/j.electacta.2004.05.038.

[155] S S Zhang et al. 'LiPF6–EC–EMC electrolyte for Li-ion battery'. In: *Journal of Power Sources* 107.1 (Apr. 2002), pp. 18–23. DOI: https://doi.org/10.1016/S0378-7753(01)00968-5.

[156] Longfei Zhang et al. 'Synergistic effect between lithium bis(fluorosulfonyl)imide (LiFSI) and lithium bis-oxalato borate (LiBOB) salts in LiPF6-based electrolyte for high-performance Li-ion batteries'. In: *Electrochimica Acta* 127 (May 2014), pp. 39–44. DOI: 10.1016/j.electacta.2014.02.008.

[157] M. C. Smart et al. 'Improved low-temperature performance of lithium-ion cells with quaternary carbonate-based electrolytes'. In: *Journal of Power Sources*. Vol. 119-121. June 2003, pp. 349–358. DOI: 10.1016/S0378-7753(03)00154-X.

[158] L. Niedzicki, B. Brzozowski and P. Wieczorek. 'LiTDI and solvent mixture based electrolytes for lithium-ion cells'. In: *Electrochimica Acta* 174 (June 2015), pp. 625–629. DOI: 10.1016/j.electacta.2015.06.038.

[159] Andrew A. Wang et al. 'Current-driven solvent segregation in lithium-ion electrolytes'. In: *Cell Reports Physical Science* 3.9 (Sept. 2022). DOI: 10.1016/j.xcrp.2022.101047.

[160] T. M.M. Heenan et al. 'Mapping internal temperatures during high-rate battery applications'. In: *Nature* 617.7961 (May 2023), pp. 507–512. DOI: 10.1038/s41586-023-05913-z.

[161] C. P. Aiken et al. 'Tracking Electrolyte Motion in Cylindrical Li-ion Cells Using Moment of Inertia Measurements'. In: *Journal of The Electrochemical Society* 170.4 (Apr. 2023), p. 040529. DOI: 10.1149/1945-7111/acce72.

[162] Florian Schmidt and Monika Schönhoff. 'Solvate Cation Migration and Ion Correlations in Solvate Ionic Liquids'. In: *Journal of Physical Chemistry B* 124.7 (Feb. 2020), pp. 1245–1252. DOI: 10.1021/acs.jpcb.9b11330.

[163] David M. Halat et al. 'Electric-Field-Induced Spatially Dynamic Heterogeneity of Solvent Motion and Cation Transference in Electrolytes'. In: *Physical Review Letters* 128.19 (May 2022). DOI: 10.1103/PhysRevLett.128.198002.

[164] Darby T. Hickson et al. 'Complete characterization of a lithium battery electrolyte using a combination of electrophoretic NMR and electrochemical methods'. In: *Physical Chemistry Chemical Physics* 22.3 (Sept. 2022). DOI: 10.1039/d2cp02622h.

[165] Saheli Chakraborty et al. 'Lithium transference in electrolytes with star-shaped multivalent anions measured by electrophoretic NMR'. In: *Physical Chemistry Chemical Physics* 25.31 (June 2023), pp. 21065–21073. DOI: 10.1039/d3cp00923h.

[166] Darby T. Hickson et al. 'Low-Temperature Characterization of a Nonaqueous Liquid Electrolyte for Lithium Batteries'. In: *Journal of The Electrochemical Society* 171.3 (Mar. 2024), p. 030514. DOI: 10.1149/1945-7111/ad2d91.

[167] Sophie Solchenbach et al. 'Quantification of PF5 and POF3 from Side Reactions of LiPF6 in Li-Ion Batteries'. In: *Journal of The Electrochemical Society* 165.13 (Sept. 2018), A3022–A3028. DOI: 10.1149/2.0481813jes.

[168] V. A. Del Grosso and C. W. Mader. 'Speed of Sound in Pure Water'. In: *The Journal of the Acoustical Society of America* 52.5B (Nov. 1972), pp. 1442–1446. DOI: 10.1121/1.1913258.

[169] Nykolai Bilaniuk and George S.K. Wong. 'Speed of sound in pure water as a function of temperature'. In: *Journal of the Acoustical Society of America* 93.3 (1993), pp. 1609–1612. DOI: 10.1121/1.406819.

[170] Mouad Dahbi et al. 'Comparative study of EC/DMC LiTFSI and LiPF6 electrolytes for electrochemical storage'. In: *Journal of Power Sources* 196.22 (Nov. 2011), pp. 9743–9750. DOI: 10.1016/j.jpowsour.2011.07.071.

[171] Patrice Porion et al. 'Comparative study on transport properties for LiFAP and LiPF6 in alkyl-carbonates as electrolytes through conductivity, viscosity and NMR self-diffusion measurements'. In: *Electrochimica Acta* 114 (2013), pp. 95–104. DOI: 10.1016/j.electacta.2013.10.015.

[172] Henrik Lundgren, Mårten Behm and Göran Lindbergh. ' Electrochemical Characterization and Temperature Dependency of Mass-Transport Properties of LiPF 6 in EC:DEC '. In: *Journal of The Electrochemical Society* 162.3 (2015), A413–A420. DOI: 10.1149/2.0641503jes.

[173] Andreas Hofmann and Thomas Hanemann. 'Novel electrolyte mixtures based on dimethyl sulfone, ethylene carbonate and LiPF6 for lithium-ion batteries'. In: *Journal of Power Sources* 298 (Dec. 2015), pp. 322–330. DOI: 10.1016/j.jpowsour.2015.08.071.

[174] Andrew A. Wang et al. 'Shifting-reference concentration cells to refine composition-dependent transport characterization of binary lithium-ion electrolytes'. In: *Electrochimica Acta* 358 (Oct. 2020). DOI: 10.1016/j.electacta.2020.136688.

[175] Miles Cranmer. 'Interpretable Machine Learning for Science with PySR and SymbolicRegression.jl'. In: (May 2023). URL: http://arxiv.org/abs/2305.01582.

[176] B E Conway et al. 'Transitions In the Speed of Sound in Concentrated Aqueous Electrolyte Solutions'. In: *The Journal of Physical Chemistry* 89.7 (Mar. 1985), pp. 1062–1064. URL: https://pubs.acs.org/sharingguidelines.

[177] A. G. Hsieh et al. 'Electrochemical-acoustic time of flight: In operando correlation of physical dynamics with battery charge and health'. In: *Energy and Environmental Science* 8.5 (May 2015), pp. 1569–1577. DOI: 10.1039/c5ee00111k.

[178] Wesley Chang et al. 'Understanding Adverse Effects of Temperature Shifts on Li-Ion Batteries: An Operando Acoustic Study'. In: *Journal of The Electrochemical Society* 167.9 (Jan. 2020), p. 090503. DOI: 10.1149/1945-7111/ab6c56.

[179] Lukas Gold et al. 'Probing lithium-ion batteries' state-of-charge using ultrasonic transmission – Concept and laboratory testing'. In: *Journal of Power Sources* 343 (2017), pp. 536–544. DOI: 10.1016/j.jpowsour.2017.01.090.

[180] Clement Bommier et al. 'Operando Acoustic Monitoring of SEI Formation and Long-Term Cycling in NMC/SiGr Composite Pouch Cells'. In: *Journal of The Electrochemical Society* 167.2 (Jan. 2020), p. 020517. DOI: 10.1149/1945-7111/ab68d6.

[181] Wesley Chang and Daniel Steingart. 'Operando 2D Acoustic Characterization of Lithium-Ion Battery Spatial Dynamics'. In: *ACS Energy Letters* 6 (2021), pp. 2960–2968. DOI: 10.1021/acsenergylett.1c01324.

[182] Michael S. Ding. 'Liquid-solid phase equilibria and thermodynamic modeling for binary organic carbonates'. In: *Journal of Chemical and Engineering Data* 49.2 (Mar. 2004), pp. 276–282. DOI: 10.1021/je034134e.

[183] Masamoto Watanabe and Raymond M Fuoss. 'Quatemization Kinetics. IV. Pyridine and 4-Picoline in Ethylene Carbonate and 4-Picoline in Mixtures of Propylene Carbonate and Diphenyl Etherl'. In: *Journal of the American Chemical Society* 78.3 (Feb. 1956), pp. 509–696. URL: https://pubs.acs.org/sharingguidelines.

[184] D J Meier et al. 'Dielectric Properties of Liquid Propylene Carbonate Dielectric Properties of Liquid Propylene Carbonate'. In: *The Journal of Physical Chemistry* 74.7 (Apr. 1970), pp. 1405–1654. URL: https://pubs.acs.org/sharingguidelines.

[185] Ao Tang, Jie Bao and Maria Skyllas-Kazacos. 'Studies on pressure losses and flow rate optimization in vanadium redox flow battery'. In: *Journal of Power Sources* 248 (Feb. 2014), pp. 154–162. DOI: 10.1016/j.jpowsour.2013.09.071.

[186] Ao Tang, Jie Bao and Maria Skyllas-Kazacos. 'Thermal modelling of battery configuration and self-discharge reactions in vanadium redox flow battery'. In: *Journal of Power Sources* 216 (Oct. 2012), pp. 489–501. DOI: 10.1016/j.jpowsour.2012.06.052.

[187] Yitao Yan et al. 'Modelling and simulation of thermal behaviour of vanadium redox flow battery'. In: *Journal of Power Sources* 322 (Aug. 2016), pp. 116–128. DOI: 10.1016/j.jpowsour.2016.05.011.

[188] Malcolm MacDonald and Robert M. Darling. 'Modeling flow distribution and pressure drop in redox flow batteries'. In: *AIChE Journal* 64.10 (Oct. 2018), pp. 3746–3755. DOI: 10.1002/aic.16330.

[189] Leon D. Brown et al. 'The effect of felt compression on the performance and pressure drop of all-vanadium redox flow batteries'. In: *Journal of Energy Storage* 8 (Nov. 2016), pp. 91–98. DOI: 10.1016/j.est.2016.10.003.

[190] S. Kumar and S. Jayanti. 'Effect of flow field on the performance of an all-vanadium redox flow battery'. In: *Journal of Power Sources* 307 (Mar. 2016), pp. 782–787. DOI: 10.1016/j.jpowsour.2016.01.048.